Calhoun: The NPS Institutional Archive

DSpace Repository

Theses and Dissertations | 1. Thesis and Dissertation Collection, all items

2012-06

Modeling Radiation Effects on a Triple Junction Solar Cell using Silvaco ATLAS

Schiavo, Daniel

Monterey, California. Naval Postgraduate School

http://hdl.handle.net/10945/7412

Downloaded from NPS Archive: Calhoun

http://www.nps.edu/library

Calhoun is the Naval Postgraduate School's public access digital repository for research materials and institutional publications created by the NPS community. Calhoun is named for Professor of Mathematics Guy K. Calhoun, NPS's first appointed -- and published -- scholarly author.

Dudley Knox Library / Naval Postgraduate School
411 Dyer Road / 1 University Circle
Monterey, California USA 93943

NAVAL POSTGRADUATE SCHOOL

MONTEREY, CALIFORNIA

THESIS

MODELING RADIATION EFFECTS ON A TRIPLE JUNCTION SOLAR CELL USING SILVACO ATLAS

by

Daniel Schiavo

June 2012

Thesis Advisor:	Sherif Michael
Second Reader:	Douglas Fouts

Approved for public release; distribution is unlimited

THIS PAGE INTENTIONALLY LEFT BLANK

REPORT DOCUMENTATION PAGE			Form Approved OMB No. 0704-0188
Public reporting burden for this collection of information is estimated to average 1 hour per response, including the time for reviewing instruction, searching existing data sources, gathering and maintaining the data needed, and completing and reviewing the collection of information. Send comments regarding this burden estimate or any other aspect of this collection of information, including suggestions for reducing this burden, to Washington headquarters Services, Directorate for Information Operations and Reports, 1215 Jefferson Davis Highway, Suite 1204, Arlington, VA 22202-4302, and to the Office of Management and Budget, Paperwork Reduction Project (0704-0188) Washington DC 20503.			
1. AGENCY USE ONLY ***(Leave blank)***	**2. REPORT DATE** June 2012	**3. REPORT TYPE AND DATES COVERED** Master's Thesis	
4. TITLE AND SUBTITLE Modeling Radiation Effects on a Triple Junction Solar Cell using Silvaco ATLAS		**5. FUNDING NUMBERS**	
6. AUTHOR(S) Daniel Schiavo			
7. PERFORMING ORGANIZATION NAME(S) AND ADDRESS(ES) Naval Postgraduate School Monterey, CA 93943-5000		**8. PERFORMING ORGANIZATION REPORT NUMBER**	
9. SPONSORING /MONITORING AGENCY NAME(S) AND ADDRESS(ES) N/A		**10. SPONSORING/MONITORING AGENCY REPORT NUMBER**	
11. SUPPLEMENTARY NOTES The views expressed in this thesis are those of the author and do not reflect the official policy or position of the Department of Defense or the U.S. Government. IRB Protocol number: N/A.			
12a. DISTRIBUTION / AVAILABILITY STATEMENT Approved for public release; distribution is unlimited		**12b. DISTRIBUTION CODE**	

13. ABSTRACT (maximum 200 words)

In this research, Silvaco ATLAS, an advanced virtual wafer fabrication tool, was used to model the effects of radiation on a triple junction InGaP/GaAs/Ge solar cell. A Silvaco ATLAS model of a triple junction InGaP/GaAs/Ge cell was created by first creating individual models for solar cells composed of each material. Realistic doping levels were used and thicknesses were varied to produce the design parameters and create reasonably efficient solar cell models for testing. After the individual solar cells were built, defects simulating the damage caused by radiation were introduced into the semiconductor model. After showing that the defects had a noticeable effect on the characteristics of the individual cells, a triple-junction solar cell created by layering the individual cells was then modeled. Work from previous NPS theses provided the background for modeling solar cells and the effects of radiation using Silvaco ATLAS. Data from another thesis provided the number of defects associated with the different fluence levels simulated.

14. SUBJECT TERMS ATLAS, Fluence, I-V Curve, Photogeneration, Radiation, Semiconductors, Silvaco, Solar Cell, Traps, Triple Junction			**15. NUMBER OF PAGES** 133
			16. PRICE CODE
17. SECURITY CLASSIFICATION OF REPORT Unclassified	**18. SECURITY CLASSIFICATION OF THIS PAGE** Unclassified	**19. SECURITY CLASSIFICATION OF ABSTRACT** Unclassified	**20. LIMITATION OF ABSTRACT** UU

NSN 7540-01-280-5500 Standard Form 298 (Rev. 2-89)
Prescribed by ANSI Std. 239-18

THIS PAGE INTENTIONALLY LEFT BLANK

Approved for public release; distribution is unlimited

MODELING RADIATION EFFECTS ON A TRIPLE JUNCTION SOLAR CELL USING SILVACO ATLAS

Daniel Schiavo
Ensign, United States Navy
B.S., U.S. Naval Academy, 2011

Submitted in partial fulfillment of the
requirements for the degree of

MASTER OF SCIENCE IN ELECTRICAL ENGINEERING

from the

NAVAL POSTGRADUATE SCHOOL
June 2012

Author: Daniel Schiavo

Approved by: Sherif Michael
Thesis Advisor

Douglas Fouts
Second Reader

Clark Robertson
Chair, Department of Electrical and Computer Engineering

THIS PAGE INTENTIONALLY LEFT BLANK

ABSTRACT

In this research, Silvaco ATLAS, an advanced virtual wafer fabrication tool, was used to model the effects of radiation on a triple junction InGaP/GaAs/Ge solar cell. A Silvaco ATLAS model of a triple junction InGaP/GaAs/Ge cell was created by first creating individual models for solar cells composed of each material. Realistic doping levels were used and thicknesses were varied to produce the design parameters and create reasonably efficient solar cell models for testing. After the individual solar cells were built, defects simulating the damage caused by radiation were introduced into the semiconductor model. After showing that the defects had a noticeable effect on the characteristics of the individual cells, a triple-junction solar cell created by layering the individual cells was then modeled. Work from previous NPS theses provided the background for modeling solar cells and the effects of radiation using Silvaco ATLAS. Data from another thesis provided the number of defects associated with the different fluence levels simulated.

THIS PAGE INTENTIONALLY LEFT BLANK

TABLE OF CONTENTS

I. INTRODUCTION 1

II. BASIC SEMICONDUCTOR PHYSICS 3
- A. PARTICLES, ATOMS, AND ELEMENTS 3
- B. SEMICONDUCTOR CRYSTAL STRUCTURES 8
- C. CHARGE CARRIERS 10
- D. SEMICONDUCTOR DOPING AND IMPURITIES 11
- E. FERMI LEVEL 12
- F. DIFFUSION AND DRIFT CURRENT 14
- G. MOBILITY 15
- H. GENERATION/RECOMBINATION 17
- I. MANUFACTURING PROCESSES 18

III. P-N JUNCTION 21
- A. BASIC P-N JUNCTION 21
- B. REVERSE APPLIED BIAS 23
- C. FORWARD APPLIED BIAS 24
- D. REVERSE BREAKDOWN 26

IV. SOLAR CELLS 29
- A. P-N JUNCTION SOLAR CELL PROPERTIES 29
- B. FACTORS AFFECTING SOLAR CELL EFFICIENCY 33
- C. MULTIJUNCTION SOLAR CELLS 35

V. RADIATION 39
- A. OVERVIEW 39
- B. CARRIERS OF RADIATION 43
- C. IONIZATION 43
- D. DISPLACEMENT DAMAGE 44

VI. SILVACO ATLAS MODELING SOFTWARE 47
- A. OVERVIEW 47
- B. SILVACO ATLAS BACKGROUND 47
- C. SILVACO ATLAS INPUTS AND OUTPUTS 48
- D. SILVACO ATLAS INPUT DECK STRUCTURE 49
- E. ATLAS GENERAL DEVICE CONSTRUCTION OUTLINE 51
  - 1. Mesh 51
  - 2. Regions 53
  - 3. Contacts 54
  - 4. Doping 55
  - 5. Material 56
  - 6. Physical Models 56
  - 7. Solution Method 57
  - 8. Solution Specification 58
  - 9. Data Extraction and Plotting 59
- F. CONCLUSION 59

VII. RESULTS OF SIMULATION 61
A. INDIVIDUAL INGAP SOLAR CELL 61
B. INDIVIDUAL GAAS SOLAR CELL 62
C. INDIVIDUAL GE SOLAR CELL 64
D. INGAP/GAAS/GE TRIPLE JUNCTION SOLAR CELL 65
E. DISCUSSION OF RESULTS 71

VIII. CONCLUSIONS AND RECOMMENDATIONS 75

APPENDIX A. ATLAS SOURCE CODE 85
A. INGAP SOLAR CELL INPUT DECK 85
B. GAAS SOLAR CELL INPUT DECK 86
C. GE SOLAR CELL INPUT DECK 88
D. INGAP SOLAR CELL INPUT DECK 90
E. RADIATION STATEMENTS 92
1. 1 MeV Fluence of $10e^{14}$ 92
2. 1 MeV Fluence of $10e^{15}$ 93
3. 1 MeV Fluence of $10e^{16}$ 94

APPENDIX B. MATLAB SCRIPT 97
A. LOADING DATA AND PLOTTING I-V CURVES 97
B. COMPARING ISC, VOC, AND PMAX OF THE EXPERIMENTAL AND SIMULATED TRIPLE JUNCTION SOLAR CELLS UNDER THREE FLUENCE LEVELS 100
C. COMPARING ISC, VOC, AND PMAX OF THE EXPERIMENTAL AND SIMULATED GAAS SOLAR CELLS UNDER THREE FLUENCE LEVELS 102

LIST OF REFERENCES 105

INITIAL DISTRIBUTION LIST 111

LIST OF FIGURES

Figure 1. The Periodic Table from NCSU. From [5].....4
Figure 2. Structure of a silicon atom. From [6].....5
Figure 3. Hydrogen line spectra. From [7].....5
Figure 4. Electron shell organization. From [9].....6
Figure 5. Band gap illustration. From [11].....7
Figure 6. Band gap comparison. From [12].....8
Figure 7. Single crystal, polycrystalline, and amorphous solids. From [14].....9
Figure 8. Basic crystal structures. From [15].....9
Figure 9. Diamond crystal structure. From [16].....10
Figure 10. Substitutional and interstitial impurities. From [17].....12
Figure 11. Fermi-Dirac Distribution Function. From [18]....13
Figure 12. Fermi level for intrinsic, n-type, and p-type material. From [7].....14
Figure 13. Diffusion current in a material and equilibrium. From [19].....15
Figure 14. Drift of a carrier due to an applied electric field. From [20].....15
Figure 15. Depiction of decreasing mobility as doping concentration increases. From [1].....16
Figure 16. Types of recombination. From [21].....18
Figure 17. Silicon grown using the Czochralski growth method. From [22].....19
Figure 18. Epitaxial growth of a semiconductor. From [23]..20
Figure 19. Simple p-n junction diffusion and its resulting depletion region. From [24].....22
Figure 20. Energy-band diagram of a p-n junction. From [25].....22
Figure 21. Reverse applied bias to a p-n junction. From [26].....24
Figure 22. Energy-band diagram of a reverse-biased p-n junction. From [27].....24
Figure 23. A forward biased p-n junction. From [28].....25
Figure 24. Forward biased p-n junction band diagram. From [29].....25
Figure 25. Realistic performance of a p-n junction with reverse breakdown compared to the ideal case. From [30].....26
Figure 26. Basic diagram of zener breakdown. From [31].....27
Figure 27. An electron causing the chain reaction of an avalanche breakdown. From [32].....27

Figure 28. P-N junction representation of a solar cell. From [33].....30
Figure 29. I-V curve for a photovoltaic cell showing its maximum power rectangle. From [34].....31
Figure 30. AM0 spectrum. From [35].....33
Figure 31. I-V curves of Ge, Si, GaAs, and InGaP. From [36].....36
Figure 32. InGaP/GaAs/Ge Solar Cell. From [37].....37
Figure 33. Spectrum and band gap energies of Ge, Si, GaAs, and InGaP. From [36].....38
Figure 34. Diagram of three Earth orbits. From [39].....42
Figure 35. Van Allen radiation belts. From [38].....42
Figure 36. Ionization damage due to radiation. From [41]...44
Figure 37. Poole-Frenkel defect. From [4].....45
Figure 38. Elastic collision cascade effect. From [4].....45
Figure 39. The input/output structure utilized by ATLAS. From [42].....49
Figure 40. ATLAS input deck structure outline. From [42]...50
Figure 41. Fine and course meshing in ATLAS.....52
Figure 42. Regions created in a semiconductor device.....53
Figure 43. Contacts on a GaAs solar cell.....54
Figure 44. Doping levels in different regions. From [43]..55
Figure 45. I-V characteristics of an InGaP solar cell with and without radiation effects.....61
Figure 46. I-V characteristics of an GaAs solar cell with and without radiation effects.....63
Figure 47. I-V characteristics of a Ge solar cell with and without radiation effects.....64
Figure 48. Silvaco ATLAS structure file of the triple junction cell.....66
Figure 49. A comparison of the outputs of an InGaP solar cell and the top layer of the triple junction cell.....67
Figure 50. A comparison of the outputs of a GaAs solar cell and the middle layer of the triple junction cell.....67
Figure 51. A comparison of the outputs of a Ge solar cell the bottom layer of the triple junction cell....68
Figure 52. I-V curves from the top layer (InGaP) of the triple junction solar cell with and without radiation damage.....68
Figure 53. I-V curves from the middle layer (GaAs) of the triple junction solar cell with and without radiation damage.....69

Figure 54. I-V curves from the bottom layer (Ge) of the triple junction solar cell with and without radiation damage.....69
Figure 55. The overall I-V curves from the simulated triple junction solar cell with and without radiation damage.....70
Figure 56. Triple junction solar cell I-V curve. From [44].....72
Figure 57. Triple junction solar cell I-V curve from Silvaco ATLAS simulation.....72
Figure 58. Remaining short circuit current after different levels of radiation. From [44].....73
Figure 59. Remaining open circuit voltage after different levels of radiation. From [44].....73
Figure 60. Remaining maximum power after different levels of radiation. From [44].....73
Figure 61. A comparison of the effects of radiation on the short circuit current of the experimental and simulated GaAs solar cells.....77
Figure 62. A comparison of the effects of radiation on the open circuit voltage of the experimental and simulated GaAs solar cells.....78
Figure 63. A comparison of the effects of radiation on the maximum power of the experimental and simulated GaAs solar cells.....78
Figure 64. Normalized values for short circuit current in a GaAs solar cell. From [45].....79
Figure 65. Normalized values for open circuit voltage in a GaAs solar cell. From [45].....79
Figure 66. Normalized values for maximum power in a GaAs solar cell. From [45].....80
Figure 67. A comparison of the effects of radiation on the short circuit current of the experimental and simulated triple junction solar cells.....81
Figure 68. A comparison of the effects of radiation on the open circuit voltage of the experimental and simulated triple junction solar cells.....82
Figure 69. A comparison of the effects of radiation on the maximum power of the experimental and simulated triple junction solar cells.....82

THIS PAGE INTENTIONALLY LEFT BLANK

LIST OF TABLES

Table 1. InGaP solar cell characteristics.....62
Table 2. GaAs solar cell characteristics.....63
Table 3. Ge solar cell characteristics.....65
Table 4. Triple junction solar cell characteristics.....71
Table 5. Data from [44] triple junction solar cell.....74
Table 6. Data from the Silvaco ATLAS simulation triple junction solar cell.....74
Table 7. Comparison of important characteristics of the simulated and experimental GaAs solar cells.....77
Table 8. Comparison of important characteristics of the simulated and experimental triple junction solar cells.....81

THIS PAGE INTENTIONALLY LEFT BLANK

EXECUTIVE SUMMARY

Solar cells are crucial to the war-fighting capability of the United States because they are the main power source for military satellites that give the U.S. information superiority, the ability to communicate quickly and effectively, and the ability to perform precision strikes against enemy targets. However, these same solar cells are also a critical vulnerability due to their degradation from radiation in space. Unfortunately, space radiation is not the only concern; if the enemy used nuclear weapons in space, the radiation from the weapon would also damage solar cells. The degradation due to these sources of radiation will reduce the output power of the solar cells until it reaches a level that cannot supply all the power for the satellite, causing it to fail. Determining the effects of radiation on the different materials used to produce solar cells is essential.

The most current technique utilized to observe the influence of radiation on a particular material is measuring the current-voltage (I-V) curve after being exposed to a range of fluence levels of a certain type of radiation. Regrettably, this requires exhaustive testing to determine constants for a slew of material parameters in order to produce complicated mathematical estimations. This style of prediction also leads to a much higher cost due to the cycle of fabrication and testing needed to verify the mathematical estimations.

In previous theses, Michalopoulous and Tsutagawa showed that Silvaco ATLAS is suitable for modeling

individual and multi-junction solar cells. Crespin proved in his thesis that ATLAS was capable of determining the effects of radiation on a Gallium-Arsenide cell accurately. This thesis is an extension of those projects, as it contains a determination of the effects of radiation on Indium-Gallium-Phosphide and Germanium solar cells. The effects of radiation on a InGaP/GaAs/Ge triple junction solar cell are also modeled.

Permanent degradation of a solar cell due to radiation is caused by damage to the crystal structure of the semiconductor material. The destruction of the crystal structure leads to traps, which are energy levels between the conduction and valence bands that form in the band gap.

Weng-Lyang Wang, as part of his PhD dissertation at the University of Florida in 1984, determined the characterization of traps induced by 1 MeV electron radiation in solar cells. These results were found through the use of Deep Level Transient Spectroscopy techniques. These trap levels were used as the basis for the introduction of radiation damage in the solar cells modeled in this thesis. In 2002, the Tsukuba Space Center in Japan studied the effects of radiation on high efficiency triple junction solar cells at different magnitudes and fluence levels. Among the results they published were the decay in the open circuit voltage, short-circuit current, and the maximum power.

Silvaco ATLAS solar cell models were produced for three fluence levels of 1 MeV electron radiation. The results of the ATLAS simulation showed an accurate

representation of radiation effects on a triple junction cell when compared to the measurements published in 2002 by the Tsukuba Space Center.

THIS PAGE INTENTIONALLY LEFT BLANK

ACKNOWLEDGMENTS

I would like to thank Professor Sherif Michael for his guidance throughout the course of working on this thesis. I appreciate the input and suggestions of Dr. Douglas Fouts and the people of the Research Office. I would also like to thank Research Associate Matthew Porter for his expertise with Silvaco ATLAS and MATLAB. Finally, I would like to thank my family for their patience and help proofreading this thesis.

THIS PAGE INTENTIONALLY LEFT BLANK

I. INTRODUCTION

The U.S. military has continued to be dominant in warfare due to its technological superiority. Much of that supremacy is possible due to the satellites that the U.S. has launched into orbit. Once these satellites are in space, repairing and refueling them is difficult and costly; therefore, the satellites require resilient hardware and software as well as a renewable power source. The best solution for a renewable power source in space is the solar cell.

The latest and best solar cells are now multi-junction and have achieved efficiencies of over 30 percent. The most concerning aspect of a solar cell in space is how quickly the performance degrades due to the breakdown of the material from which the cell is made. The main sources of energetic particles that are of concern are protons and electrons trapped in the Van Allen belts, heavy ions trapped in the magnetosphere, cosmic ray protons and heavy ions, and protons and heavy ions from solar flares [1].

Michalopoulous [2] utilized the tools available from the Silvaco ATLAS device simulator to model the operation of multi-junction solar cells. His work helped prove that ATLAS can be used as an effective, efficient tool to help lower costs and decrease the amount of time need to design solar cells. Tsutagawa [3] developed an optimized triple junction cell comprised of GaAs, InGaP, and Ge. Crespin [4] developed a novel approach to simulate the effects of space radiation on a GaAs solar cell at different levels of radiation. As an extension of these works, modeling and

simulating radiation effects on GaAs, InGaP, and Ge individually as well as in a triple junction solar cell in Silvaco ATLAS are incorporated in this thesis.

A background discussion of semiconductor physics, solar cells, and defects in solar cells is provided in Chapter II. An overview of p-n junctions is given in Chapter III. A background on solar cells is provided in Chapter IV. Radiation and its effects are discussed in Chapter V. The Silvaco ATLAS software and the procedures used to model a solar cell and the effects of radiation upon them are discussed in Chapter VI. The results of this thesis are shown and discussed in Chapter VII. The conclusions of this thesis and recommendations for future work in this area are noted in Chapter VIII. The ATLAS source code used to simulate the solar cells and radiation effects is provided in Appendix A. The MATLAB code used to generate the overall current-voltage characteristics of the triple junction cell is given in Appendix B.

II. BASIC SEMICONDUCTOR PHYSICS

A method to model the effects of radiation on Germanium, Indium Gallium Phosphide, and Gallium Arsenide solar cells individually and together in a triple junction cell is presented in this thesis. A discussion on basic semiconductor physics, solar cell operation, and material manufacturing is provided in this chapter. An examination of defects within the solar cell material and their effects is also included.

A. PARTICLES, ATOMS, AND ELEMENTS

All matter in the known universe is made up of particles called protons, electrons, and neutrons. Elements, the basic building blocks of matter, are constructed using these particles. All elements contain a nucleus that is composed of positively charged protons and neutral neutrons. Around the nucleus of each element are negatively charged electrons. The strong attraction between the opposing charges of the protons and electrons is what binds the atom together. The element created is determined by the number of protons, electrons, and neutrons, which also determines its number on the periodic table. The periodic table is composed of all of the elements in increasing order, and the elements are grouped into the different categories shown in Figure 1.

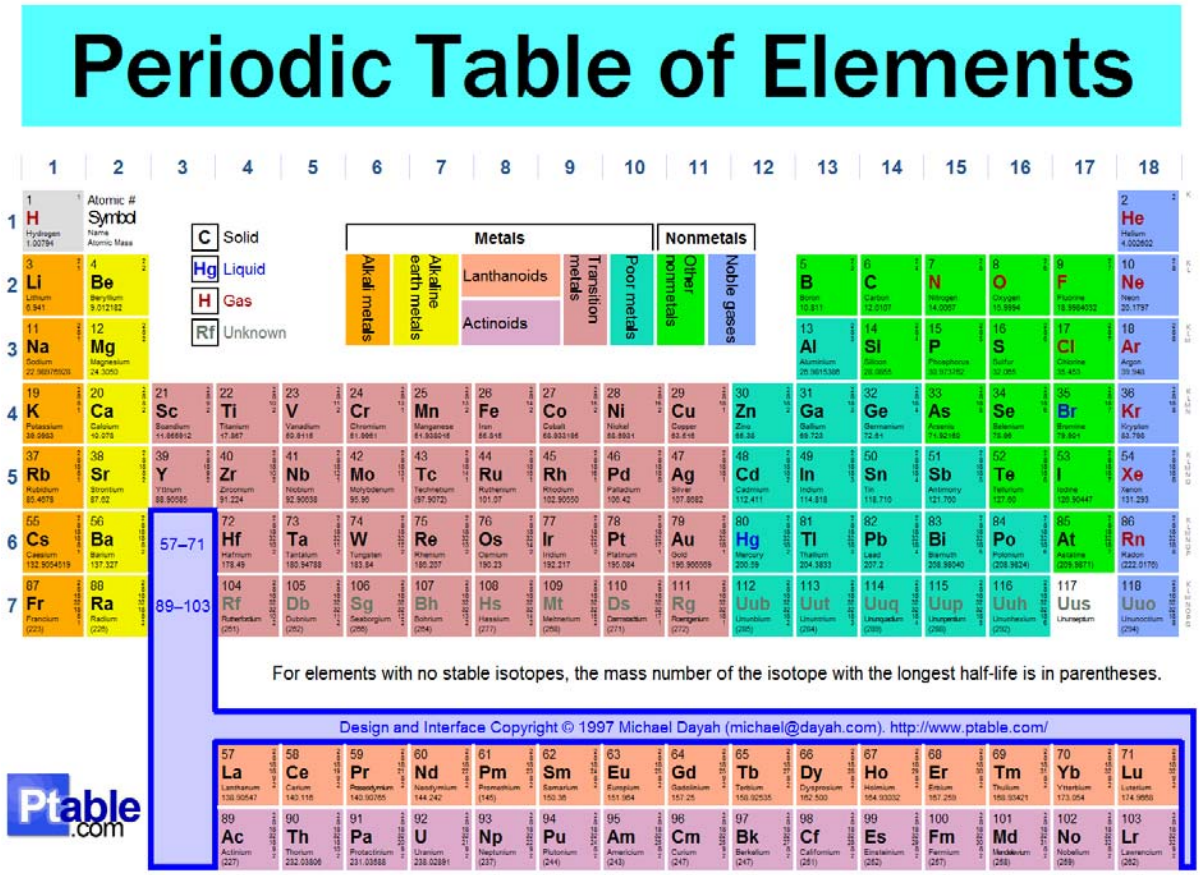

Figure 1. The Periodic Table from NCSU. From [5].

The illustration in Figure 2 of a silicon atom helps introduce the concept of electron shells. The nucleus contains fourteen protons and fourteen neutrons. While the protons and neutrons are contained inside of the nucleus, electrons are relatively free to move and are organized into shells. Niels Bohr was the first to develop this theory using line spectra, and an example of line spectra can be seen in Figure 3 [7]. Bohr knew that heating up elements caused the emission of light in specific spectra, rather than white light. He also knew that this emission was in small, precise quantities and was not continuous. He postulated that when electrons were heated or consumed

energy they would "jump" to a higher state, and the light generated was due to electrons losing energy by "falling" to lower states. The amount of energy lost in the "fall" corresponded to the wavelength of the light emitted [8]. Each shell can hold a certain number of electrons before a new shell must be created. These shells are divided up into four orbitals: s, p, d, and f. The orbitals are combined to form levels which are determined by the elements row of the periodic table. The shell organization can be seen in Figure 4.

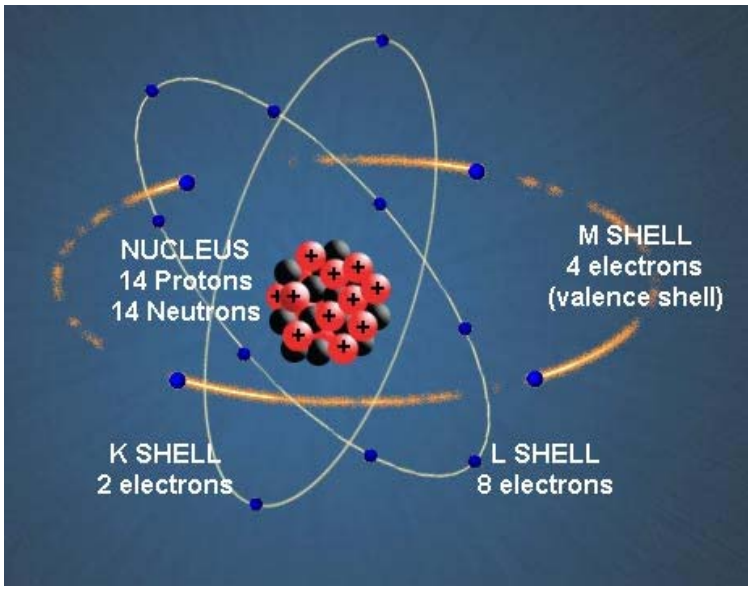

Figure 2. Structure of a silicon atom. From [6].

Figure 3. Hydrogen line spectra. From [7].

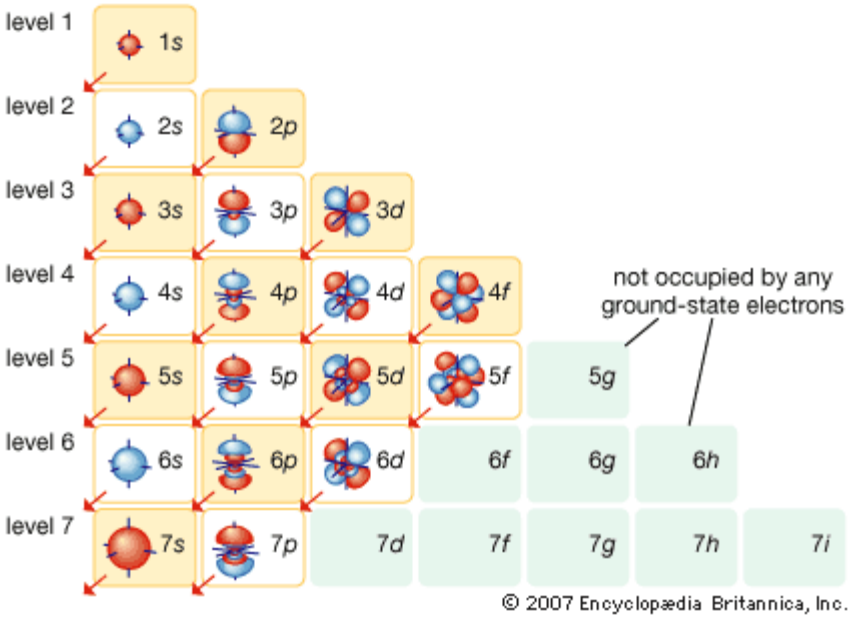

Figure 4. Electron shell organization. From [9].

The next concept that needs to be understood in order to study solar cells is how the band gap of an element affects an electron's ability to move to different levels. Each element has unique electrical properties such as resistance ρ and conductivity σ that determine the band gap of a material. The band gap separates the conduction band from the valence band and represents an energy range in which no electron states can exist. An illustration of this can be seen in Figure 5. At absolute zero, or zero Kelvin, all valence electrons are contained in the valence band. When energy is given to these electrons, such as an increase in temperature, some of the electrons will break free and move to the conduction level. It is important to note that when free electrons occupy the conduction band, the absence of these electrons results in the formation of a hole in the valence band. The energy required for an electron to transition from the valence band to the

conduction band is defined as the band gap energy E_g and has units of electron volts (eV) [10].

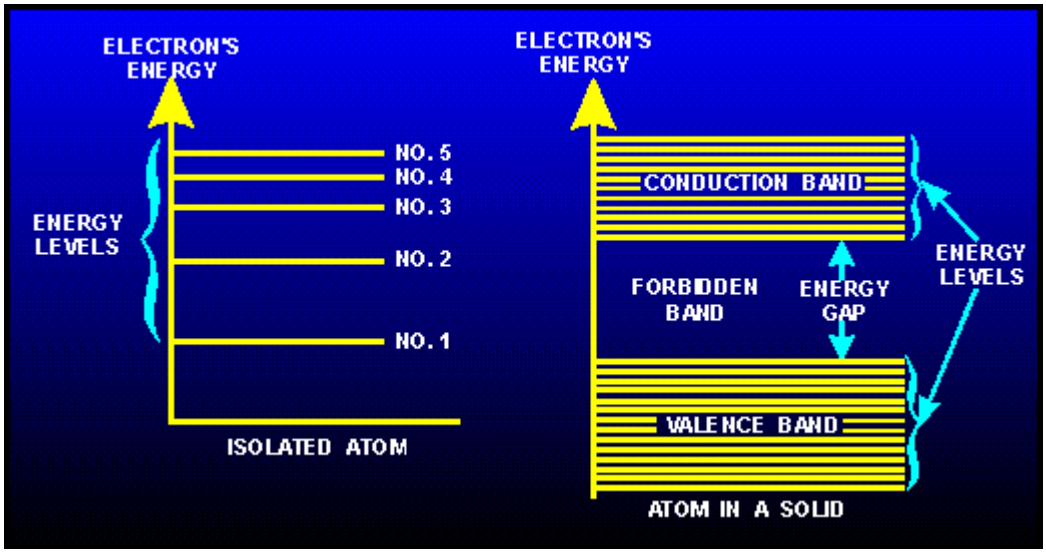

Figure 5. Band gap illustration. From [11].

From these characteristics, elements and compounds can be classified as insulators, conductors, or semiconductors. A conductive material more readily releases electrons from its valence shell, the outermost electron shell, with very little or no addition of energy. At one extreme, the insulator has a very large band gap and is hostile towards electrons attempting to cross from the valence band to the conduction band due to the large amount of energy required. At the other extreme, the conductor has no band gap because the valence and conduction bands overlap. Therefore, electrons are free to move with little or no external energy. Finally, the semiconductor has a bandgap small enough that electrons are still able to cross from the valence band to the conduction band with a reasonable amount of externally applied energy. For the purpose of this thesis, semiconductors are the most important of the

three because solar cells are built using this type of material. An illustration of the three types of materials with their respective band gap diagrams is shown in Figure 6.

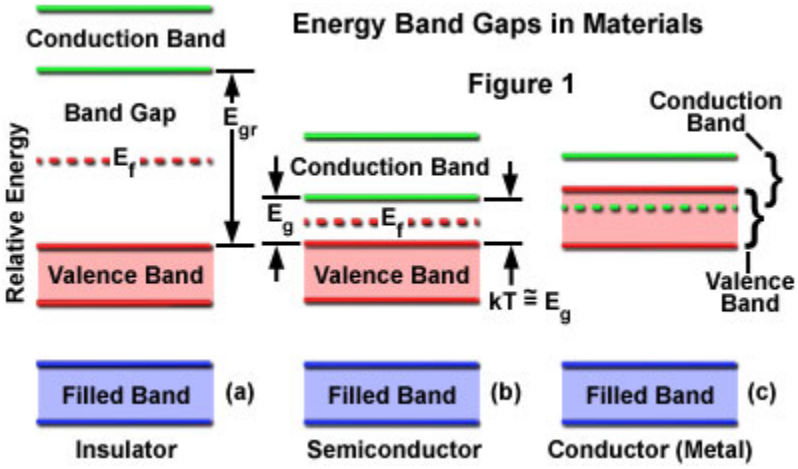

Figure 6. Band gap comparison. From [12].

B. SEMICONDUCTOR CRYSTAL STRUCTURES

Solids are organized into three categories: amorphous, polycrystalline, and single crystal, all of which can be seen in Figure 7. Amorphous solids only have order within a few atomic or molecular dimensions but are otherwise not uniform. Polycrystalline solids have regions of order, but these regions are not ordered with respect to one another. Finally, the single crystal solid has geometric periodicity throughout the entire volume of the material and, therefore, is the solid with the best electrical properties. The advantage is due to the lack of grain boundaries that would have degraded electrical characteristics [13].

Figure 7. Single crystal, polycrystalline, and amorphous solids. From [14].

All solid materials are formed into crystal structures based on three basic crystal structures: simple cubic, body-centered cubic, and the face-centered cubic. The simple cubic structure has atoms on each corner, the body-centered cubic has atoms on the corners and one in the center, and the face-centered cubic has atoms on the corners and each face of the structure. The most common structure is the diamond. It is not a simple cubic structure, but it is composed of two body-centered cubic diagonally adjacent to each other. The three basic crystal structures are shown in Figure 8, and the diamond crystal structure is depicted in Figure 9.

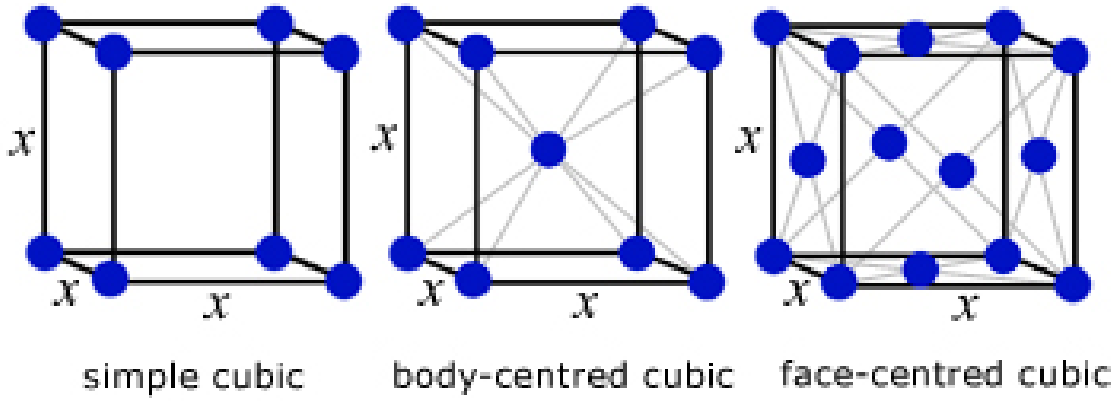

Figure 8. Basic crystal structures. From [15].

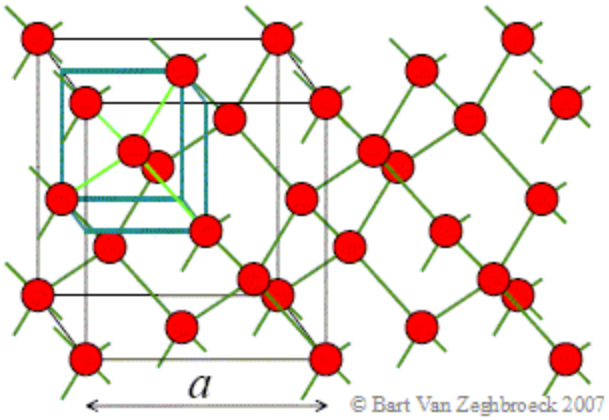

Figure 9. Diamond crystal structure. From [16].

C. CHARGE CARRIERS

For the solar cell application of semiconductors, the most important aspect of a material is the current-voltage characteristic. Current is the movement of charge through a material. The charges in a semiconductor that can move within the material as a result of applied force are called carriers. Carriers must flow to and from the conduction and valence bands in order to create a current in the semiconductor. One such carrier is the electron, which has a negative charge. The change in energy of an electron can be calculated from

$$dE = F\ dx = Fv\ dt \qquad (2.1)$$

where dE is the change in energy, F is the applied force, dx is the change in position, and v is the velocity. Given enough input energy, a valence electron will break free of its covalent bond and move to the conduction band, creating a carrier. The amount of energy required for this promotion is the band gap energy E_g. The second type of carrier, the counterpart to the electron, is the hole. A positively charged empty state is created whenever a valence band

electron escapes to the conduction band or another valence electron moves into the hole created by the original escaped electron. Because of this effect, a positive charge has the ability to "move" throughout a material as well. The electron-hole pair is the fundamental principle of electric current flow within semiconductor based devices [13].

D. SEMICONDUCTOR DOPING AND IMPURITIES

There are two types of semiconductors, intrinsic and extrinsic. Intrinsic semiconductors are completely pure, meaning that they only have one type of element or compound within its crystal structure. Intrinsic semiconductors are impossible to create because at some point during the growth process impurities inadvertently contaminate the material. Extrinsic semiconductors are created by adding impurity atoms into intrinsic materials. Fortunately, adding impurities into a material can be beneficial to the performance of the semiconductor. Adding impurities into the substance with the intent of controlling its performance characteristics is known as doping. There are two types of doping, n-type and p-type. The n-type dopants are also known as donors because they are elements or compounds with five or more valence electrons that will donate one electron after the other four form covalent bonds with the intrinsic material into which they were placed. In n-type materials, electrons are the majority carrier and holes are the minority carriers. The p-type dopants, or acceptors, are elements or compounds that have three or less valence electrons and accept electrons, forming covalent bonds with four of their five or more

holes. The p-type materials have holes as the majority carrier and electrons as the minority carriers [13].

There are two ways that an intrinsic material may be doped so that it becomes extrinsic via a substitutional impurity or interstitial impurity. A substitutional impurity occurs when the correct atom in the sequence is replaced by an incorrect atom. An interstitial impurity is when an atom is placed into the empty space between atoms in the lattice structure. A visual representation of these impurities can be found in Figure 10.

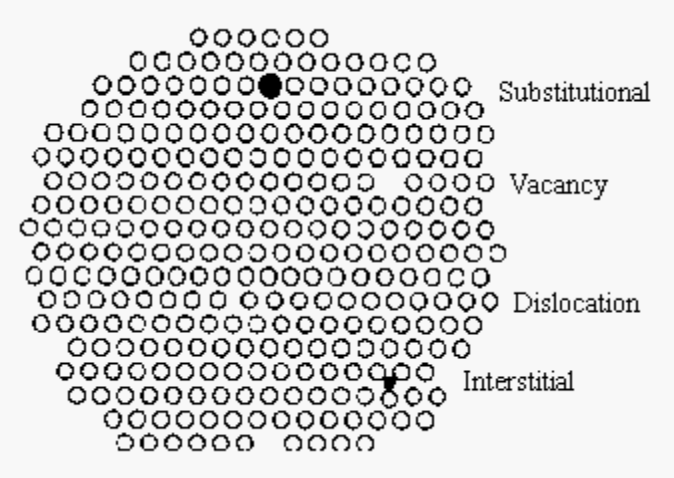

Figure 10. Substitutional and interstitial impurities. From [17]

E. FERMI LEVEL

The Fermi-Dirac distribution function gives the probability that an available energy state E is occupied by an electron at temperature T under thermal equilibrium [7]. A graphical representation can be seen in Figure 11.

The Fermi function is described mathematically as

$$f(E)=\frac{1}{1+e^{(E-E_F)/kT}} \tag{2.2}$$

where E_F is the Fermi energy or Fermi level, k is Boltzmann's constant (8.617e-5 eV/K), and T is temperature in Kelvin (K).

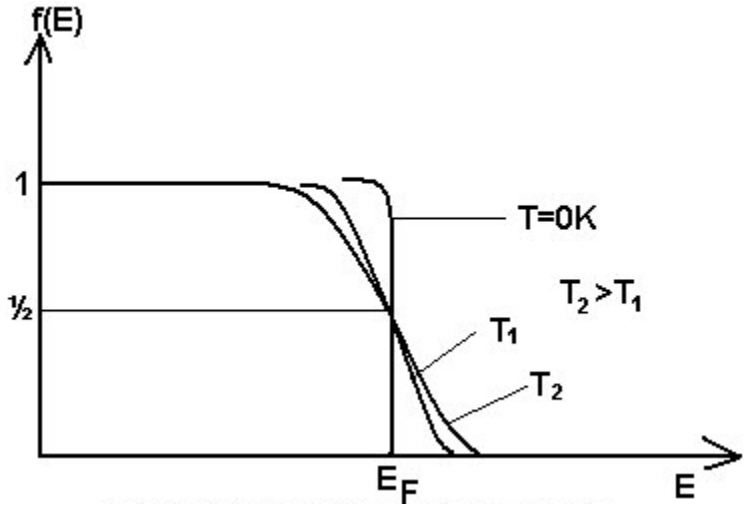

Figure 11. Fermi-Dirac Distribution Function. From [18]

The Fermi level E_F depends on the concentration of holes in the valence band and the concentration of electrons in the conduction band. In a purely intrinsic material, the Fermi level can be assumed to be directly in the middle of the band gap because the concentrations of holes and electrons are the same. This is also known as the intrinsic level of the material E_i. In n-type material, there is an excess of electrons in the conduction band, and the Fermi distribution function lies above the intrinsic level, which is closer to the conduction band. In p-type material, the opposite holds true, and the Fermi level

moves below the intrinsic level and closer to the valence band. These phenomena are shown in Figure 12.

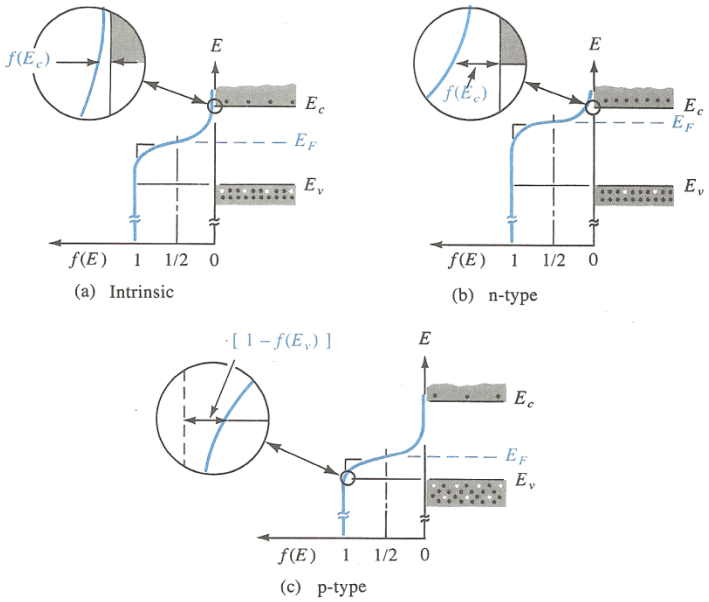

Figure 12. Fermi level for intrinsic, n-type, and p-type material. From [7]

F. DIFFUSION AND DRIFT CURRENT

Carriers flow in semiconductors because of two mechanisms: diffusion and drift. Diffusion current I_D is related to the majority carrier concentration and doping level. Diffusion current creates current when there is a higher concentration of carriers in one part of the doped semiconductor than the other, which is amplified when there is a large number of majority carriers. The carriers naturally spread throughout the material in an attempt to reach equilibrium. An illustration of diffusion current is found in Figure 13.

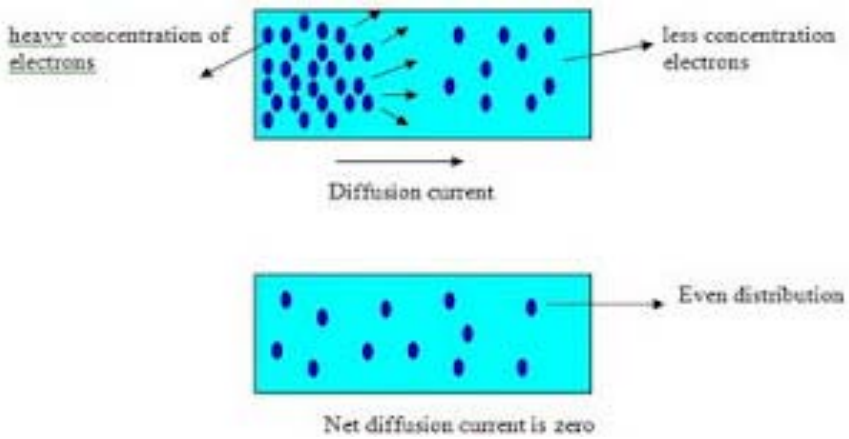

Figure 13. Diffusion current in a material and equilibrium. From [19]

Drift current I_D is produced when an electric field or magnetic field is applied to a doped semiconductor. Drift current is related to the minority carrier concentration and temperature. Drift current caused by the application of an electric field is depicted in Figure 14.

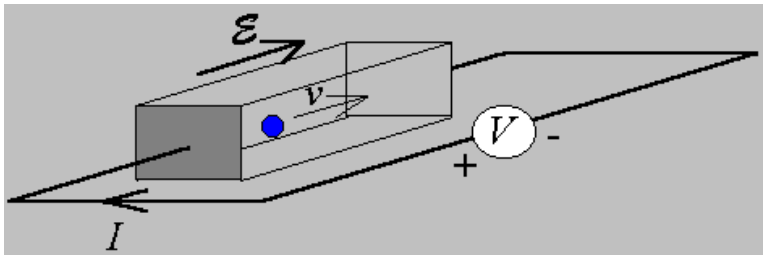

Figure 14. Drift of a carrier due to an applied electric field. From [20]

G. MOBILITY

Mobility is defined as the ease with which electrons are able to drift through a material. Carrier mobility is an important characteristic for semiconductor materials, because if the mobility is too low then the performance of

that material degrades. Some of the properties affecting the mobility of a material are: an electron's effective mass in that material, the volume density of atoms, and the mean time between scattering events. Collisions with the atoms and impurities in the lattice slow the electrons until an average drift speed is achieved. Mobility μ is the ratio of speed to the applied electric or magnetic field. Mobility is also negatively affected by increasing the temperature and the doping level because of the increased scattering effect in the material. Increasing temperature and impurity concentration decreases mobility due to carrier scattering. The effect on a silicon semiconductor's mobility suffers as the doping level increases, as shown in Figure 15. The red line is electron mobility, and the blue line is hole mobility [13].

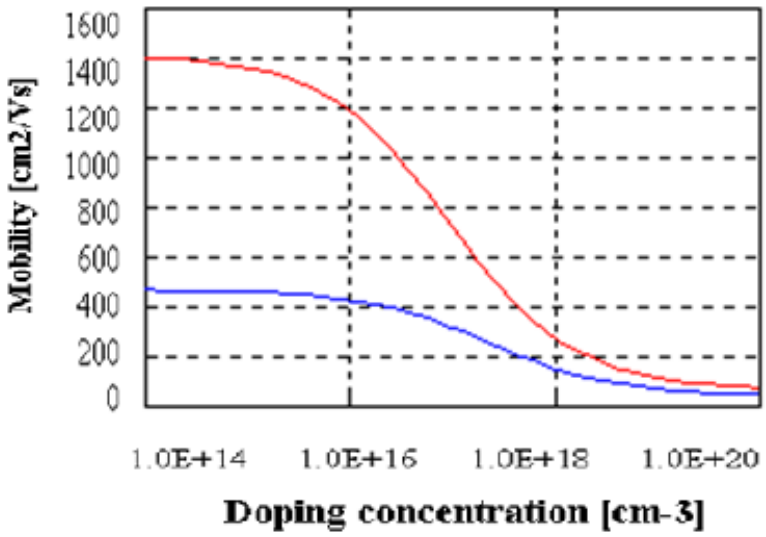

Figure 15. Depiction of decreasing mobility as doping concentration increases. From [1].

H. GENERATION/RECOMBINATION

Generation occurs when carriers are created, and recombination is a process by which the opposing carriers annihilate each other. The electrons are attracted to and fill holes in one or multiple steps. Any energy difference between the initial and final state of the electron is released after recombination. Recombination is complete when the electron-hole pair rejoins and restores system equilibrium. When recombination occurs, a small amount of energy is released and both the electron and the hole disappear. This energy can be categorized in three ways: radiative, or the emission of a photon (light), non-radiative, or the emission of a phonon (heat), and Auger, or a transfer of kinetic energy to another free electron or hole.

Band-to-band recombination occurs when an electron moves from the conduction band to a hole in the valence band without a change in momentum between the two states. Band-to-band recombinations are typically a radiative transition in direct band gap semiconductors.

Trap-assisted recombination begins when an electron gets into a trap, or an energy level within the band gap created by a structural defect or impurity. Eventually, the electron takes a second step and moves back to the valence band and recombines with a hole. This process is also known as Shockley-Read-Hall (SRH) recombination.

Augur recombination requires three particles: at least one hole and one electron and the third may be either a hole or an electron. This type of recombination is similar

to band-to-band recombination; however, the third particle receives the energy from the recombination. All three of these processes are shown in Figure 16.

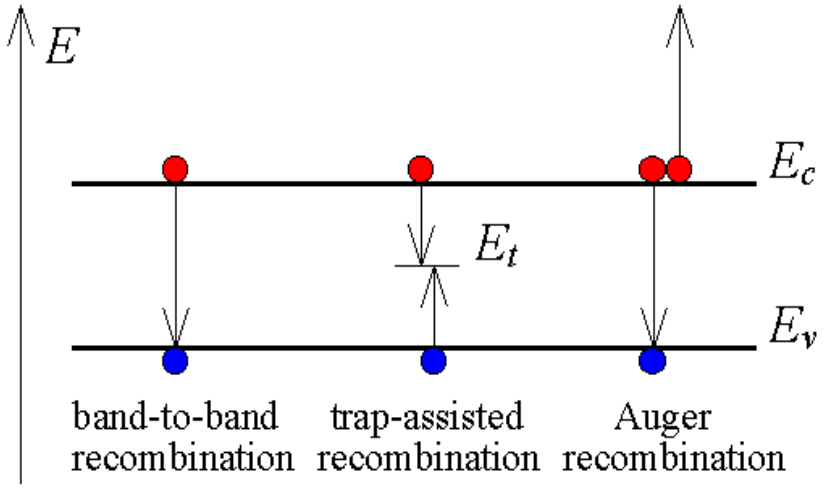

Figure 16. Types of recombination. From [21].

I. MANUFACTURING PROCESSES

The most prevalent method of producing a semiconductor material is the Czochralski growth method. A small piece of single-crystal, called the seed, is placed into a liquid comprised of the same material as the seed and is slowly twisted and pulled upwards. If a doped material is desired, then the dopants are added into the melt in their respective quantities[13]. The process of growing a silicon ingot using this process is illustrated in Figure 17.

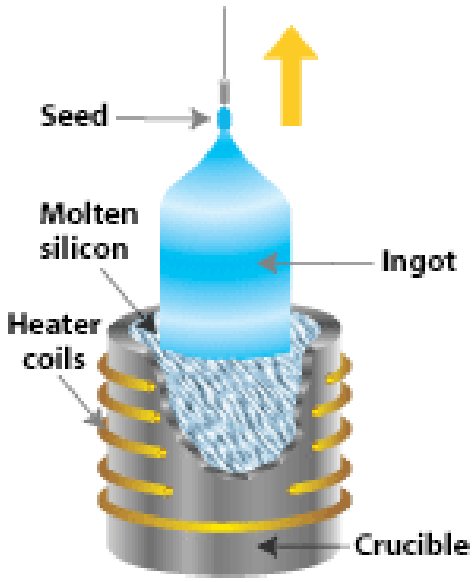

Figure 17. Silicon grown using the Czochralski growth method. From [22].

The other most commonly used growth method is epitaxial growth. It is a process by which a thin, single-crystal layer of material is grown on the surface of a single-crystal substrate. In the epitaxial process, the single-crystal substrate acts as the seed. Homoepitaxy is when the same material as the substrate is grown. Hetereoepitaxy is the process of growing a different material onto the substrate. Heteroepitaxy is much more difficult because great consideration must be taken to make sure the two substances have similar crystal structures to avoid defects at the junction of the two materials [13]. An example of epitaxial growth is shown in Figure 18.

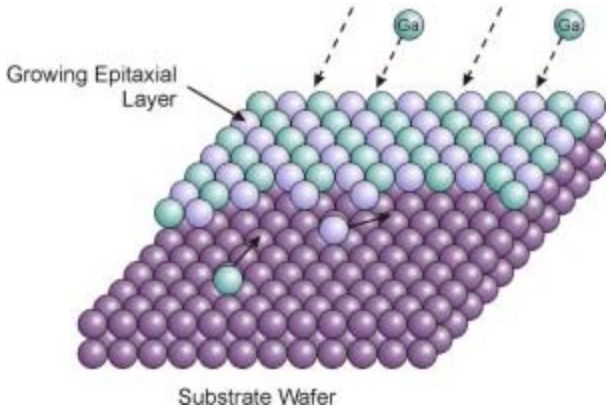

Figure 18. Epitaxial growth of a semiconductor. From [23]

III. P-N JUNCTION

A. BASIC P-N JUNCTION

Understanding the fundamentals of the p-n junction is crucial to understanding how a solar cell works because the principles that allow solar cells to work are based on these basic concepts. A p-n junction is formed when a single-crystal material has one region doped with acceptor impurity atoms to become the p-region and the other region is doped with donor impurity atoms and becomes the n-region. The boundary which joins these two regions is known as the metallurgical junction. As soon as the two regions are joined, majority carrier electrons from the n-region diffuse to the p-region, and the majority-carrier holes from the p-region diffuse to the n-region. This process creates positively charged donor atoms where the diffusing electrons are in the n-region, and negatively charged acceptor atoms where the holes are in the p-region. The net positive and negative charges induce an electric field following the direction of positive to negative, or from the n-region to the p-region. Together, these two charged regions are known as the depletion region because it is depleted of any mobile charge. Without external forces applied, this process cannot continue indefinitely [13]. A simple p-n junction diffusing and creating a depletion region is shown in Figure 19.

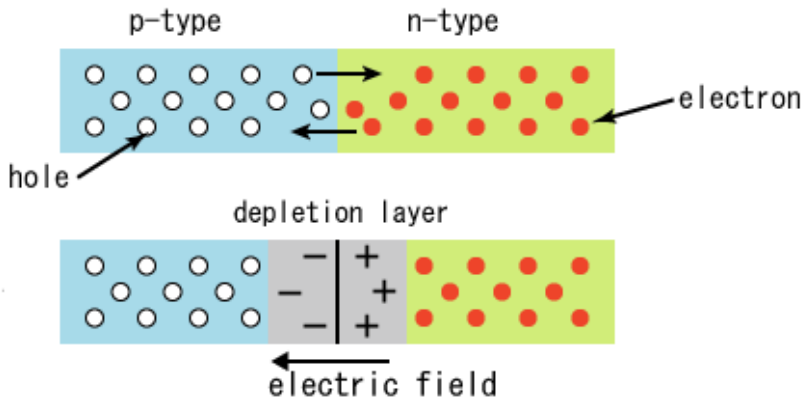

Figure 19. Simple p-n junction diffusion and its resulting depletion region. From [24].

It is important to note the effect that the joining of the p-n junction has on the Fermi level throughout the entire material. After the diffusion process ends and the material reaches thermal equilibrium, a stable Fermi level is established. The conduction and valence bands as well as the intrinsic level must then bend in relation to the Fermi level when creating the energy-band diagram for the p-n junction. This principle is illustrated in Figure 20.

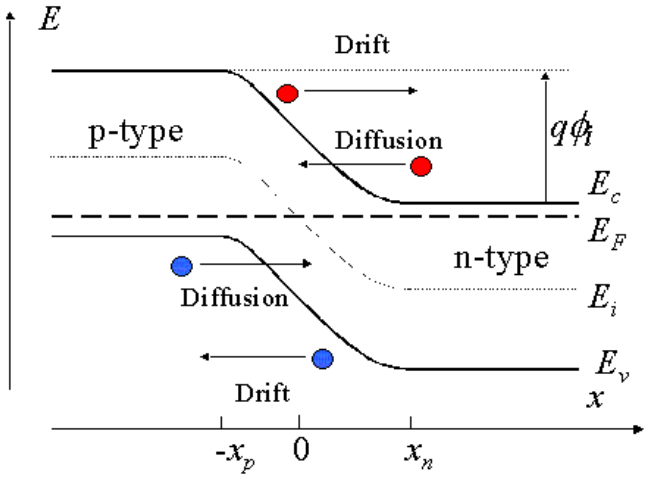

Figure 20. Energy-band diagram of a p-n junction. From [25].

The force that maintains the equilibrium without any external forces is the built-in potential barrier V_{bi}. This barrier maintains equilibrium by separating majority carrier electrons in the n-region from the minority carrier electrons in the p-region. Similarly, it separates the majority carrier holes in the p-region and the minority carrier holes in the n-region. Because this voltage maintains equilibrium, it also produces no current. The mathematical representation of this voltage is [13]

$$V_{bi} = \frac{kT}{q} \ln\left(\frac{N_a}{N_d}\right) = V_t \ln\left(\frac{N_a}{N_d}\right) \tag{3.1}$$

where N_a is the acceptor concentration (cm^{-3}), N_d is the donor concentration (cm^{-3}), and q is the charge (C).

B. REVERSE APPLIED BIAS

The p-n junction being discussed up to this point has been at thermal equilibrium because no external bias has been assumed. Once a potential is applied between the regions, many properties change. In order to reverse bias a p-n junction, a positive voltage must be applied to the n-region with respect to the p-region. Once the bias is applied, the Fermi level is no longer constant throughout the material. In an energy-band diagram, the more positive direction is downward. The Fermi level in the n-region moves below the Fermi level in the p-region, and the difference between the two is the applied bias. A p-n junction in the reverse biased configuration is shown in Figure 21. The energy-band diagram of a reverse biased p-n junction is illustrated in Figure 22 [13].

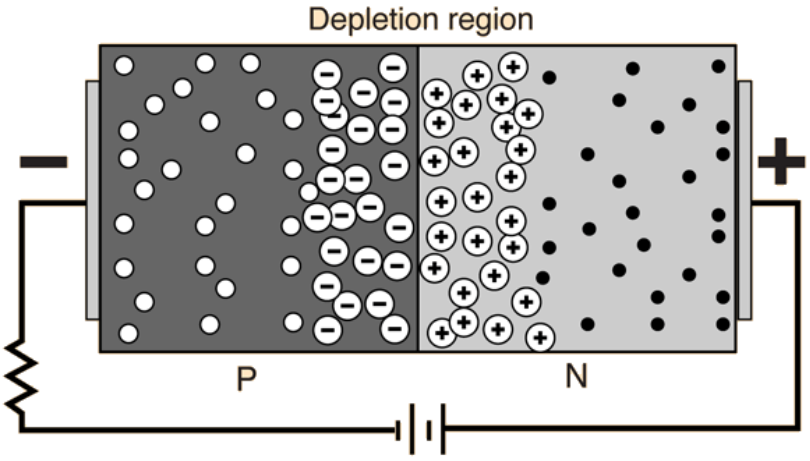

Figure 21. Reverse applied bias to a p-n junction. From [26].

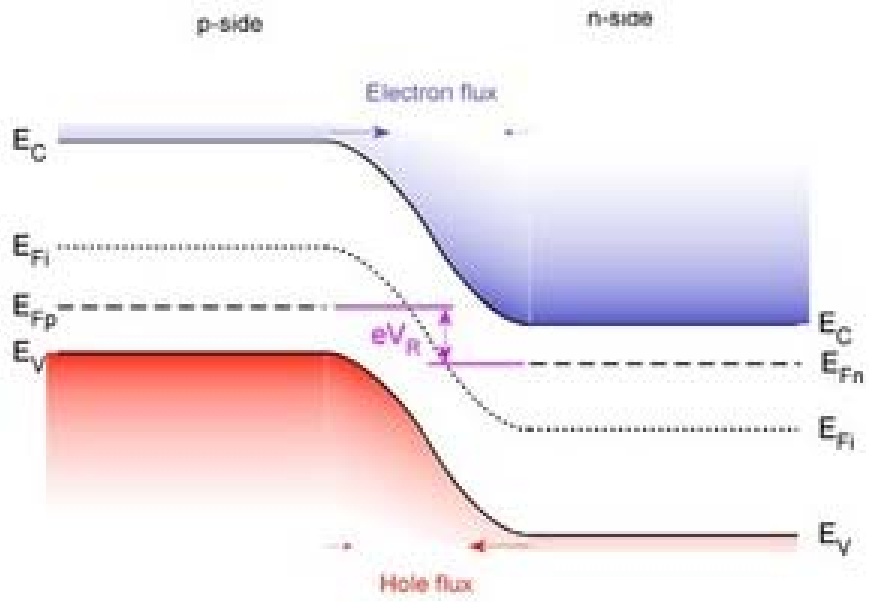

Figure 22. Energy-band diagram of a reverse-biased p-n junction. From [27].

C. FORWARD APPLIED BIAS

In order to forward bias a p-n junction, a positive voltage must be applied to the p-region with respect to the n-region. Once this bias is applied, the Fermi level is no

longer constant throughout the material. In an energy-band diagram, the negative direction is upward. The Fermi level in the n-region moves above the Fermi level in the p-region, and the difference between the two is the applied bias. A p-n junction in the forward biased configuration is shown in Figure 23, and the energy-band diagram of a forward biased p-n junction is illustrated in Figure 24 [13].

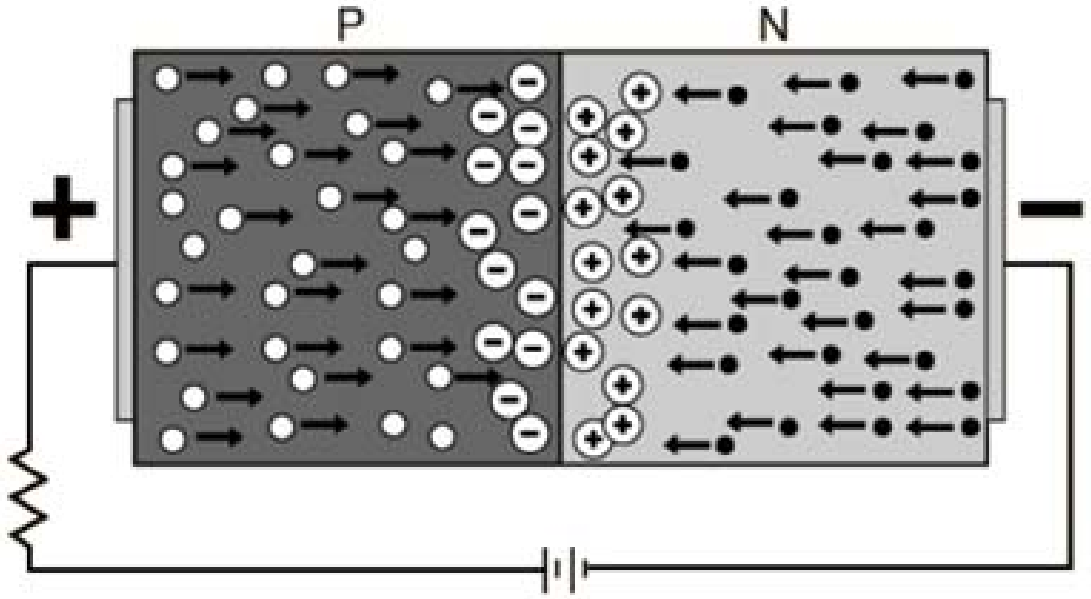

Figure 23. A forward biased p-n junction. From [28].

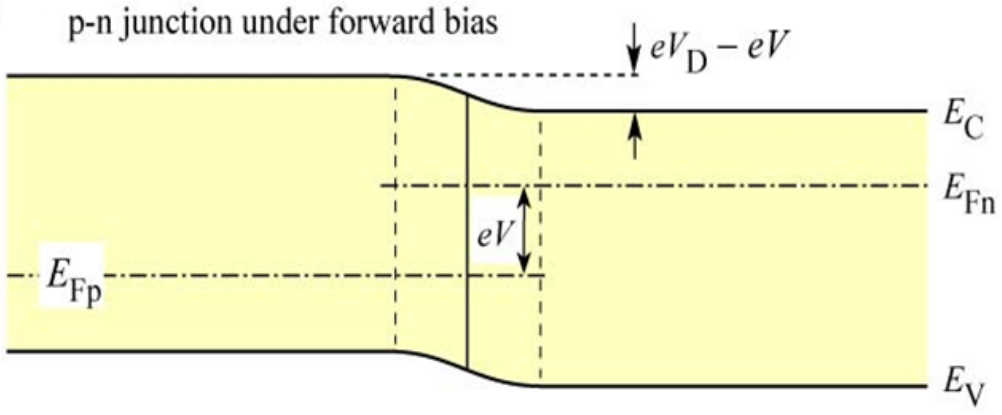

Figure 24. Forward biased p-n junction band diagram. From [29].

D. REVERSE BREAKDOWN

The ideal p-n junction creates large currents when the voltage is above zero and has zero current when the voltage becomes negative. When applying a reverse bias above a certain threshold value that is specific to the device, the p-n junction will breakdown and allow large negative current to flow through the device. The two most common types of reverse breakdown are zener and avalanche [7]. The realistic p-n junction is juxtaposed with an ideal case in Figure 25.

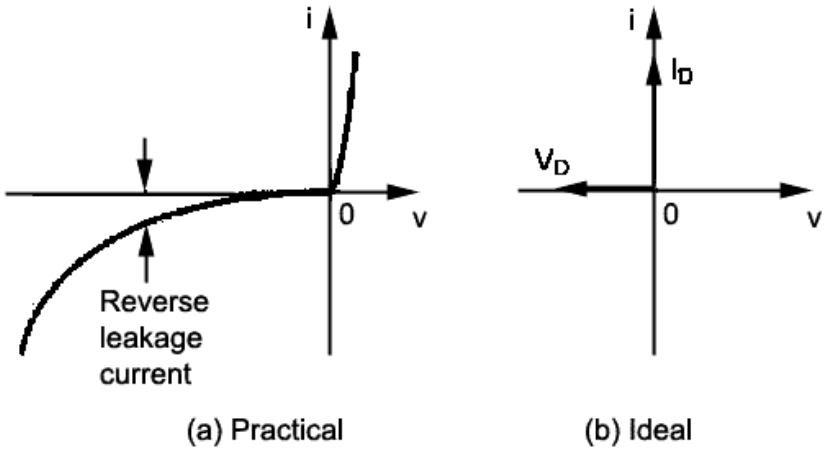

Figure 25. Realistic performance of a p-n junction with reverse breakdown compared to the ideal case. From [30]

Zener breakdown occurs in highly doped p-n junctions by means of tunneling. If the material is highly doped, then during reverse biasing the conduction and valence bands on the opposite side of the junction are so close that the electrons may travel directly from the valence band in the p-region to the conduction band in the

n-material [7]. A diagram of an electron tunneling from the p-region valence band to the n-region conduction band can be seen in Figure 26.

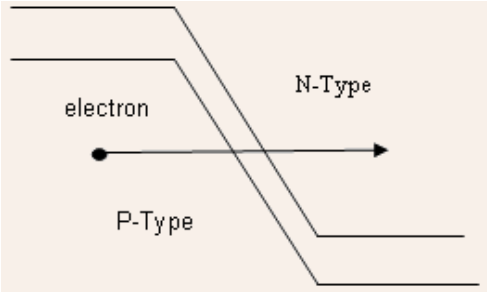

Figure 26. Basic diagram of zener breakdown. From [31].

Avalanche breakdown occurs when holes or electrons travelling through the material obtain enough energy from the electric field to create electron-hole pairs by colliding with electrons in the depletion region. This is a process known as impact ionization. A single interaction of this type results in carrier multiplication, which can lead to creating more of these events. When the field is sufficiently strong, this effect can happen rapidly and cause the breakdown [7]. This process is illustrated in Figure 27.

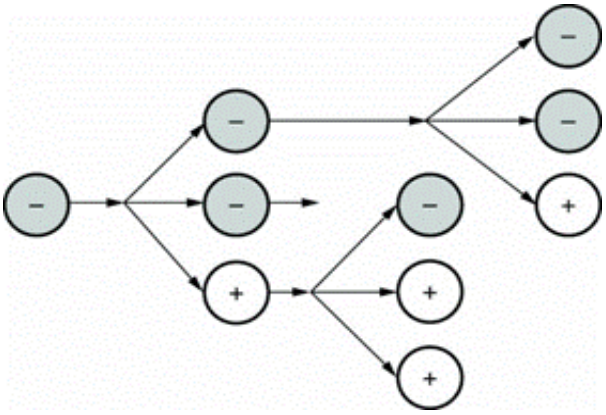

Figure 27. An electron causing the chain reaction of an avalanche breakdown. From [32].

THIS PAGE INTENTIONALLY LEFT BLANK

IV. SOLAR CELLS

A. P-N JUNCTION SOLAR CELL PROPERTIES

Solar cells generate power by utilizing the energy stored in photons of light to create electron-hole pairs in a p-n junction. The design of a solar cell is critical because each material chosen and each variation of a parameter has the potential to significantly affect the cell's performance. The five characteristics that determine the quality of a solar cell are the open circuit voltage V_{oc}, the short circuit current I_{sc}, the maximum power P_{max}, the fill factor FF, and the efficiency η.

A solar cell can be thought of as a p-n junction with a resistive load. Even without applied bias, there is an electric field in the depletion region. Photons with a high enough energy create electron-hole pairs in the depletion region that then move, creating a photocurrent I_L in the reverse-bias direction. This current creates a voltage drop across the load, which forward-biases the p-n junction. The forward-bias voltage, in turn, creates a forward-bias current I_F which opposes the photocurrent [13]. The resulting net p-n junction current I is

$$I = I_L - I_F \quad . \tag{4.1}$$

The magnitude of the electric field decreases when the junction is forward-biased, but it does not disappear altogether or reverse polarity. The photocurrent is always in the reverse-bias direction, which also causes the net

solar cell current to flow in the reverse-bias direction. The p-n junction representation of a solar cell is shown in Figure 28.

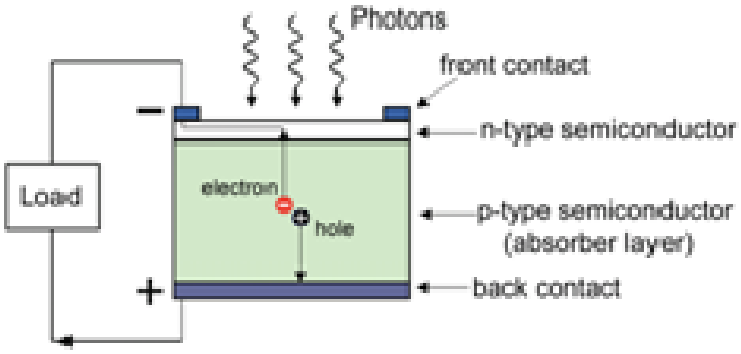

Figure 28. P-N junction representation of a solar cell. From [33].

Short circuit current is one of two important limiting parameters of a solar cell. Short circuit current is obtained when the load resistance is zero, causing the voltage to also be zero. The short circuit current is given by

$$I = I_{sc} = I_L \,. \tag{4.2}$$

The other crucial limiting parameter for a solar cell is the open circuit voltage. Under the open circuit condition, the load resistance is infinite and the current is zero. The open circuit voltage can then be calculated from

$$V_{oc} = V_t \ln\left(1 + \frac{I_L}{I_S}\right) \tag{4.3}$$

where I_S is the reverse saturation current, and V_t is the thermal voltage.

Each solar cell has a unique I-V curve that begins at zero voltage where the current is I_{SC} and ends where voltage is V_{OC} and current is zero. A solar cell's maximum power P_{max} is an important quality because the purpose of the solar cell is to deliver power to a load. The maximum power rectangle can be found within the I-V curve and is created by drawing straight lines outward from the maximum current and voltage points. An I-V curve for a solar cell with a maximum power rectangle is illustrated in Figure 29. Points A and B in Figure 29 illustrate two possible power rectangles for this solar cell, and the maximum power point MPP shows the maximum power rectangle for this solar cell. The maximum power is given by

$$P_{\max} = V_{\max} I_{\max} . \tag{4.4}$$

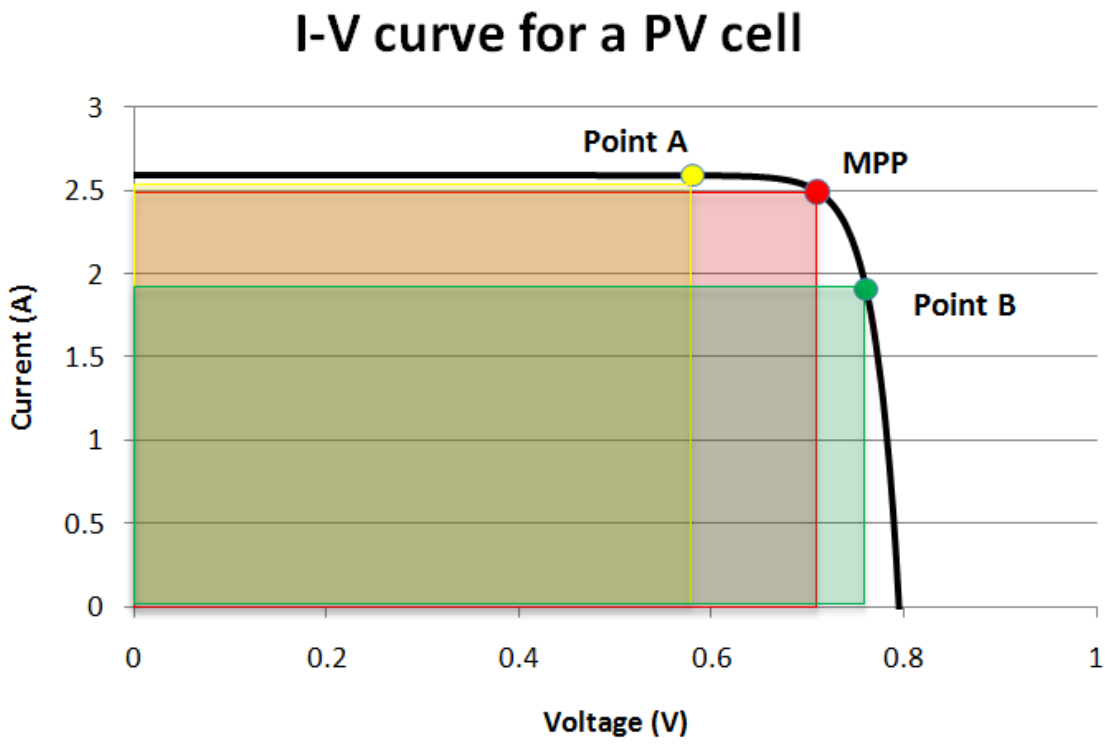

Figure 29. I-V curve for a photovoltaic cell showing its maximum power rectangle. From [34].

The fill factor FF is a ratio of the maximum power to the power that the open circuit voltage and short circuit current would make if they were multiplied together. The fill factor equation is given by

$$FF = \frac{P_{\max}}{V_{oc} I_{sc}} \; FF = \frac{P_{\max}}{V_{oc} I_{sc}} \; . \tag{4.5}$$

A fill factor of one is ideal because it creates the greatest possible maximum power for the given solar cell. The fill factor can be seen as the sharpness of the "knee" of the I-V curve. If the fill factor is equal to one, the I-V curve is a perfect rectangle.

The last and most important quality of a solar cell is its efficiency. A high efficiency cell allows a smaller cell to produce the same amount or more power than a larger cell. A larger cell not only costs more to build but also costs much more to put into space. The calculation for efficiency is given by

$$\eta = \frac{P_{\max}}{P_{in}} \tag{4.6}$$

where P_{in} is the input power from the sun. The parameter P_{in} is based on the air mass number of where the cell is located in relation to the sun. In space, the air mass number (AM0) is zero, meaning all of the energy put out by the sun at that location is receivable because the atmosphere does not intercept and dissipate it as it would on Earth. For this thesis, the light source utilized was the sun, which delivers 136.67 mW/cm^2 to solar cells in Earth's orbit. The AM0 spectrum is shown in Figure 30.

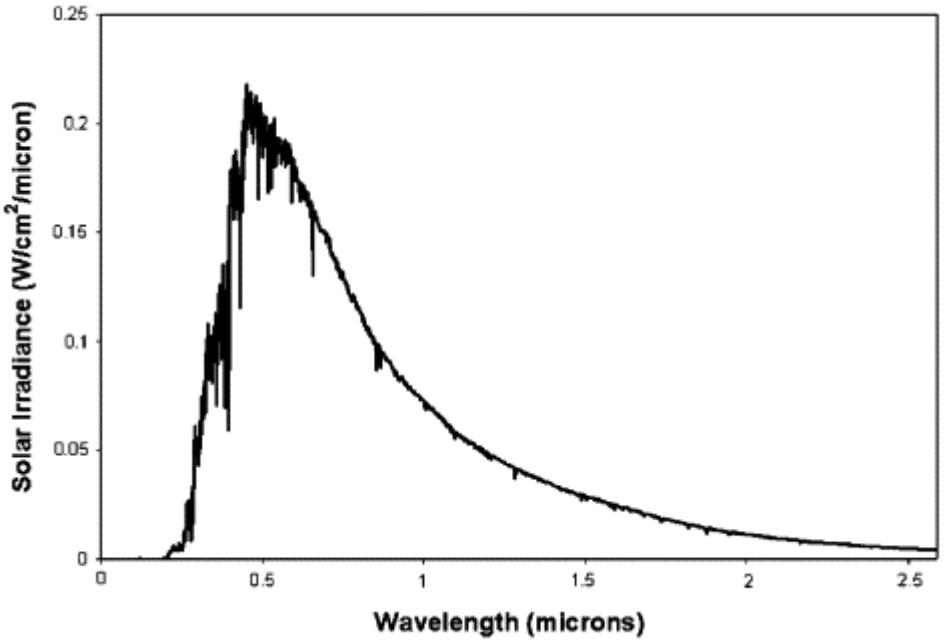

Figure 30. AM0 spectrum. From [35].

B. FACTORS AFFECTING SOLAR CELL EFFICIENCY

Efficiency is the goal of all solar cell design. There are many factors that lower a solar cell's efficiency, which is why even the best solar cells only output 30 percent of the input power radiated onto them.

Any light shone on the surface of a solar cell has the potential to simply reflect off of the surface before it can impart its energy to the electrons in the material. If the angle of incidence is far from perpendicular and the material has a highly reflective surface, then the solar cell can lose as much as 36 percent of the energy. As a solution to this problem, special anti-reflective coatings have been designed, tested, and applied to the surface of the solar cells. At a perpendicular angle of incidence, this coating has been shown to reduce the loss due to reflection by as much as 5 percent.

The next problem to consider is that all photons have different amounts of energy. The energy needed to cross the band gap is specific to each material. A photon could bombard an electron but not have enough energy to make that electron jump from the valence band to the conduction band. The second issue associated with this fact is that the collision of an under-powered photon with an electron causes it to simply heat up because it cannot cross the band gap. This is not a rare occurrence, and this leads to increased resistance due to the heating of the entire solar cell. Losses due to heating effects also significantly reduce the output.

Conversely, photons may carry too much energy. When an over-powered photon collides with an electron, it causes the electron to cross the band gap. The excess energy that was not utilized to cross the band gap is dissipated as heat and causes the same heating effects as the under-powered photon bombardment.

Another cause of increased cell temperature is the very phenomenon that allows solar cells to generate current. The electro-static field of the depletion region sweeps charge carriers to opposite sides of the cell and some internal recombination occurs, resulting in heating.

The temperature of the cell is crucial to efficient operation. When the cell is above or below its designed operating temperature, the vibration of the crystal lattice structure interferes with the movement of charge carriers through the cell, thus reducing output power.

When the semiconductor materials used to make solar cells are manufactured, inevitable defects and impurities

are introduced to the finished product. These impurities and defects to the crystal structure cause degraded performance.

The metal contacts of the solar cell have an inherent resistance that causes a loss in output power and an increase in the cell's temperature. These same contacts and the conducting grid on top of the solar cell do not allow light to pass through them and, thus, have a shading effect. This shading effect reduces the input light to the cell by up to 8 percent.

Photons are tiny particles, and even though the atoms in a crystal structure are large with respect to a photon, not all photons traveling into a solar cell bombard an electron. Some photons simply enter the cell and pass through without imparting energy. To reduce the effect of this problem, a back surface reflector is added. This reflector doubles the probability that the incoming photon collides with a semiconductor atom because the photon is reflected back through the solar cell after striking the back surface reflector [36].

C. MULTIJUNCTION SOLAR CELLS

The desire to increase the output power of solar cells has led to the creation of solar cells that are made up of layers of different materials. The reason this increases the efficiency of the overall cell is because the different materials have different I-V characteristics. A properly-designed triple junction cell has increased efficiency because the extra layers absorb additional energy even if the layer of material above consumes a considerable amount

of photons. The I-V curves of a few common materials used to create solar cells are illustrated in Figure 31.

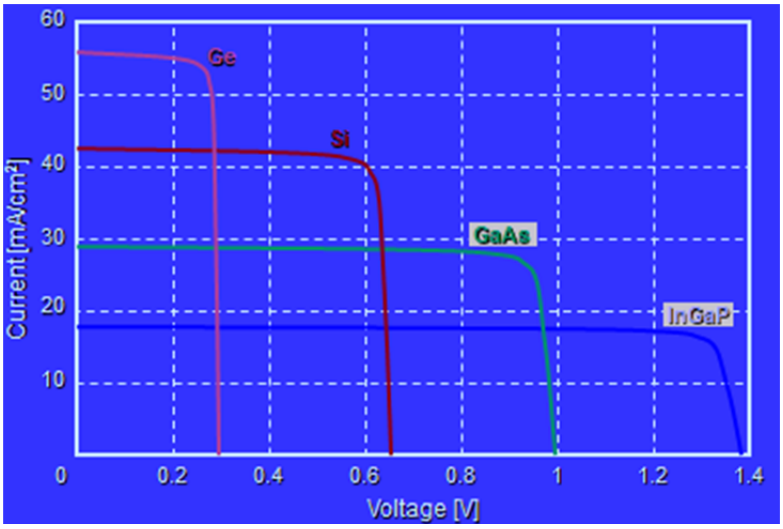

Figure 31. I-V curves of Ge, Si, GaAs, and InGaP. From [36].

This union of multiple layers is beneficial to the overall efficiency of the cell. It is important to note that, when all of these materials are put together, the voltage from each is added together, whereas the smallest current determines the overall current of the cell.

The triple junction cell that is focused on in this thesis is the InGaP/GaAs/Ge cell, with respect to the order of cell layers from the top to the bottom. A simple diagram of this cell can be seen in Figure 32.

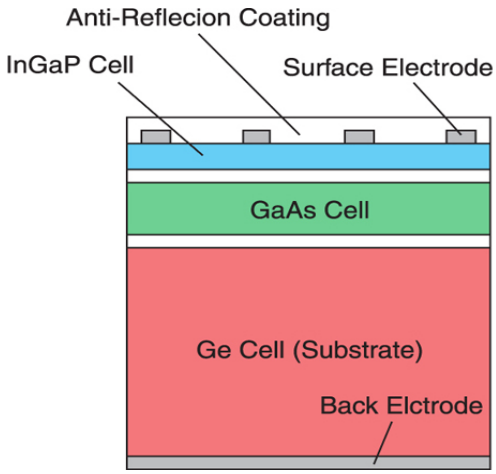

Figure 32. InGaP/GaAs/Ge Solar Cell. From [37].

The indium gallium phosphide (InGaP) material creates the least current but the highest voltage. The gallium arsenide (GaAs) material produces the second most current and voltage. Finally, the germanium (Ge) material creates the most current and the least voltage. Another factor in determining a combination of materials is the spectrum of light that each material will absorb. As seen in Figure 33, InGaP collects the shorter wavelength light and passes the rest through. GaAs collects the small and mid-range wavelengths and passes the large wavelengths onto Ge. InGaP is placed on top in order to absorb the high energy photons and allow the lower-energy photons to pass through. GaAs is the middle cell and absorbs middle energy range photons and allows the rest to pass through. Ge is used for the bottom cell so that it can absorb the remaining photons.

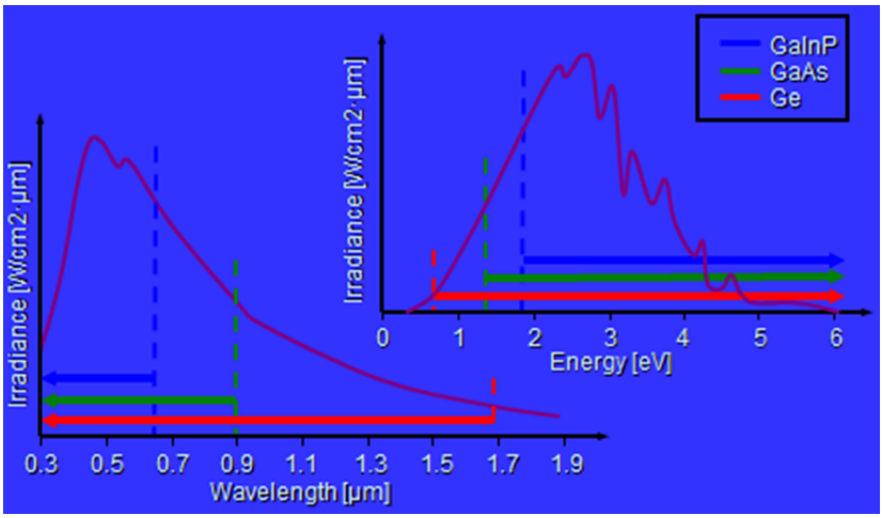

Figure 33. Spectrum and band gap energies of Ge, Si, GaAs, and InGaP. From [36].

V. RADIATION

A. OVERVIEW

Military and governmental agencies have become both more formidable and more vulnerable due to the technology used in space. Space systems must be designed to withstand the effects of naturally occurring radiation and the potential nuclear-based weapon attacks on the space infrastructure.

Radiation can be described as the emission and propagation of waves or particles, in other words, radiated energy. As such, radiation may or may not have its own mass. Radiation can be quantified in many ways, but the most common measurements used in electronic components are rads, or radiation absorbed dose, which is specific to each material absorbing the radiation. The energy of a particle can be measured in electron-volts, which are equivalent to $1.6x10^{-19}$ joules each, and fluence, which is defined by the total particles per area in a given time period with units of particles/cm^2. Radiated energy can have two possible effects when applied to semiconductors. First, radiated energy may remove or ionize electrons in the atoms, or second, at higher energies or with massive particle radiation, atoms within the crystal may be moved or displaced [38].

When considering the effects of radiation damage to the semiconductor material within solar cells, the most prominent concern is how much energy is absorbed by the semiconductor. The total energy absorbed is determined by

several conditions. The first condition is the length of time that the particle imparting the radiative energy is within range of the affected atom. For this consideration, a slow-moving particle with low kinetic energy imparts more energy. The second is the density of the target atom in g/cm^3. A denser atom absorbs more energy due to the proximity of many electrons and a large nucleus. The third is the size and mass of the radiative particle. The larger the particle, the more energy it imparts upon collision. The final consideration is the cross-sectional area of the target atom in cm^2. The larger the cross-sectional area, the more energy it absorbs [38].

The military is concerned with six types of radiation caused failure mechanisms for the semiconductors in space platforms. The first is the total dose. After absorbing this amount of radiation, the semiconductor-based component goes out of the specifications recommended by the manufacturer and is likely to fail. The next type of failure is the dose rate upset. This mechanism is measured in rads/sec and is defined as the failure of a device caused by a high-intensity pulse of ionizing radiation that induces a change in stored data. The third is dose rate latchup. This mechanism is measured in rads/sec and is defined as the failure of a device caused by the creation of a short-circuit path that irrevocably destroys the semiconductor device. Next is neutron damage. This is measured in units of neutrons/cm^2, and this type of failure causes displacement damage in the material until the overall device fails. The fifth failure mechanism is the single event upset. This type of damage causes bit errors in the memory of a system due to a single pulse of

sufficient energy, which could have devastating effects in a military application. The final type is the single event latchup. This type of failure is determined by the amount of energy that a semiconductor can absorb before causing a fatal short circuit in the device [38].

The effects of the space environment on semiconductors vary depending on the system's distance from the Earth. Three Earth orbits are shown in Figure 34. These environments can be separated into four categories for the purposes of radiation effects on orbiting electronic equipment. The first orbit of interest is the low Earth orbit (LEO). LEO encompasses any orbit within 650 kilometers of the Earth's surface. This is also considered the safest place with respect to radiation because the Earth's magnetic field protects against its effects. The next important orbit is the middle Earth orbit (MEO). MEO includes the space between 650 and 35,786 kilometers from Earth's surface. This is the worst place for electronics, as radiation has the greatest influence due to the loss of shielding from the Earth's magnetic field and the Van Allen radiation belts, areas where there are large amount of trapped radiative particles. The location of the Van Allen belts and the density of trapped protons and electrons within those belts are shown in Figure 35. The third orbit is the geosynchronous orbit (GEO). GEO is the orbit at which any satellite will rotate at the same speed as the Earth, meaning that it will continuously be above the same place on the surface of the Earth. This orbit is found at 35,786 kilometers from the Earth's surface. This orbit is above the outer Van Allen belt; therefore, the majority of the radiation it receives comes from space. Beyond GEO is

interplanetary Space, which is all of space greater than 35,786 kilometers from the Earth's surface. This area is exclusively affected by cosmic radiation.

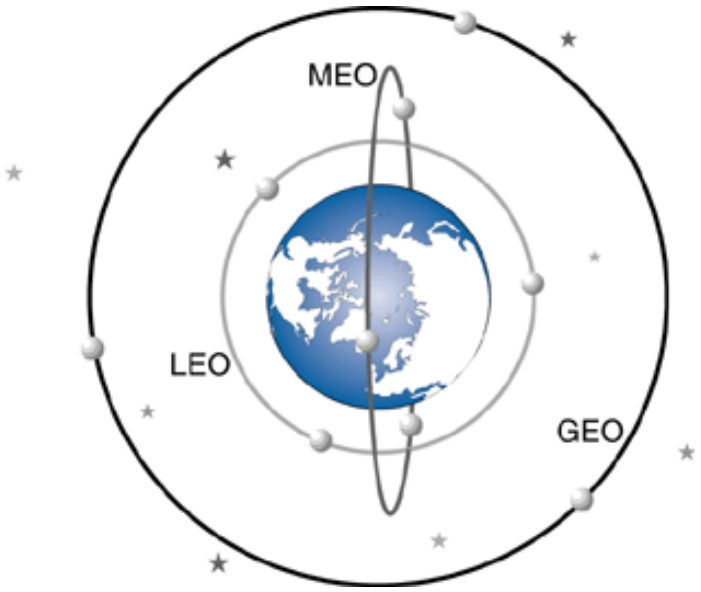

Figure 34. Diagram of three Earth orbits. From [39].

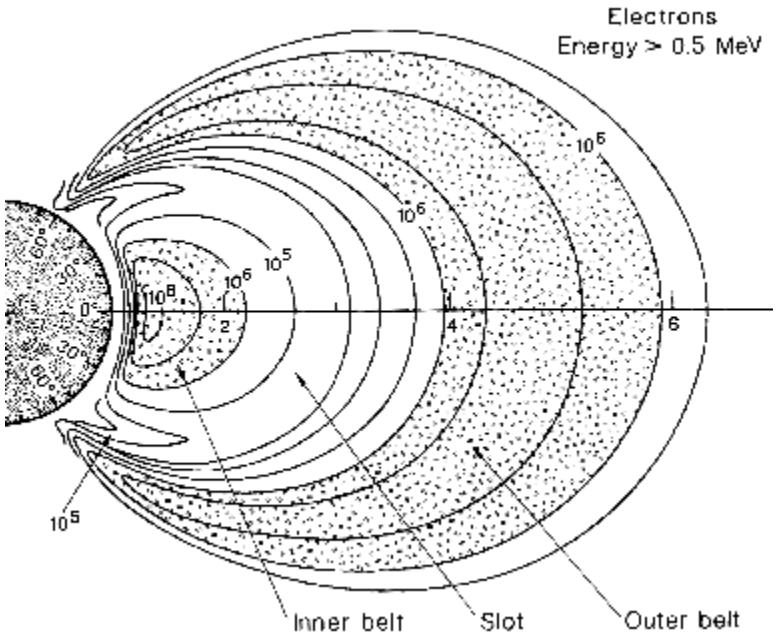

Figure 35. Van Allen radiation belts. From [38].

B. CARRIERS OF RADIATION

The Law of Conservation of Energy implies there is always a source and receiver of radiated energy. It follows that there are different types of radiation, and each has its own effect on different "targets."

Before discussing the types of radiation, it is helpful to first describe the different vehicles of radiation. Electromagnetic radiation has no mass and consists of X-rays, gamma rays, and high frequency, short wavelengths of light. Sources of this type of radiation consist mostly of the byproducts of cosmic events, such as exploding stars. The other main delivery system for radiation is through high energy particles. These particles include low-mass electrons, protons, alpha particles, light ions and heavy ions (ions that are heavier than hydrogen atoms). It is important to note that all radiative ions are positive because their high speed causes their electrons to be ionized or "stripped" [38].

C. IONIZATION

The first type of radiation damage is ionization. Ionization occurs when the radiation carries enough energy to remove an electron from an atom or molecule, leaving the remaining atom charged or ionized. The effects that ionization can have on solar cells include the reduction of cover glass transmittance, darkening of transparent polymers, and altering of polymers mechanical properties [40]. Ionizing radiation can also produce electron hole pairs, but the energy level required is significantly

greater than the level required with light [40]. An illustration of ionizing radiation is shown in Figure 36.

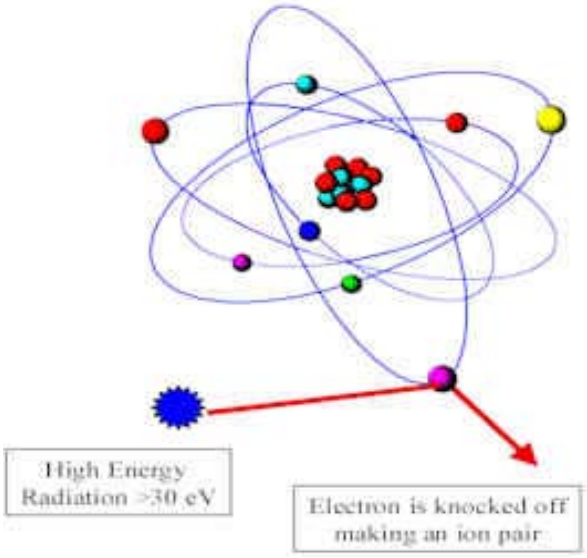

Figure 36. Ionization damage due to radiation. From [41].

D. DISPLACEMENT DAMAGE

The other form of harm that radiation causes is displacement damage. This type of radiation damage causes degradation through kinetic bombardment of atoms in the material, causing structural defects in the crystal lattice. A common outcome of this radiation is the Poole-Frenkel defect. This defect is caused when an atom in the crystal structure is dislodged, creating a vacancy in the lattice, and this displaced atom then becomes an interstitial atom. The Poole-Frenkel defect is illustrated in Figure 37. The other type of displacement damage requires higher energy radiation and also causes more damage by displacing many atoms by means of subsequent elastic collisions. This type of radiation damage is known as the elastic collision cascade effect and is shown in

Figure 38. An important correlation can be made that radiation-induced defects result in energy states within the band gap similar to those created by grown-in defects. These energy states result in trapping and recombination centers throughout the solar cell material. This similarity is used in this thesis to model the effects of equivalent radiation effects on solar cells.

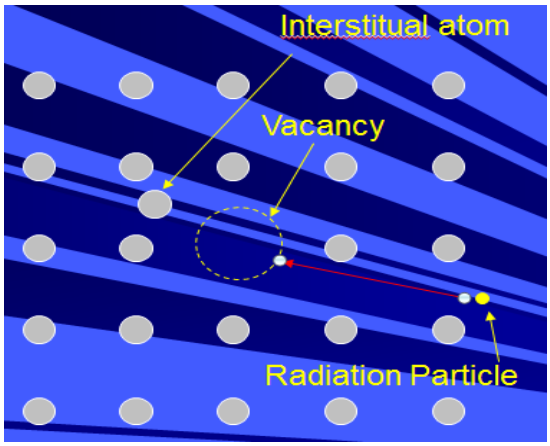

Figure 37. Poole-Frenkel defect. From [4].

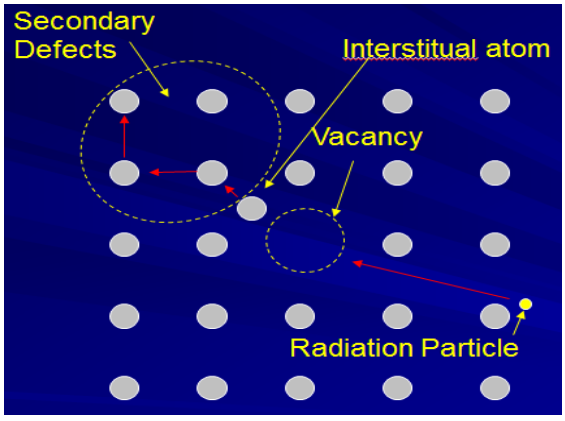

Figure 38. Elastic collision cascade effect. From [4].

THIS PAGE INTENTIONALLY LEFT BLANK

VI. SILVACO ATLAS MODELING SOFTWARE

A. OVERVIEW

The use of Silvaco ATLAS simulation software to model solar cells and then predict the effects of radiation on various performance aspects of the cell is the focus of this thesis. The capabilities of ATLAS when modeling a multi-junction solar cell are described in this chapter.

B. SILVACO ATLAS BACKGROUND

Silvaco's ATLAS software provides general capabilities for physically based two and three-dimensional simulation of semiconductor devices [42]. ATLAS is used via DeckBuild, an interactive runtime environment. Figures can be made from the data obtained from the simulation and plotted using TONYPLOT, the included interactive graphics and analysis package. ATLAS has a comprehensive collection of physical models that are of use for modeling solar cells. The collection includes drift-diffusion transport models, lattice heating and heat sinks, Fermi-Dirac and Boltzmann statistics, advanced mobility models, SRH, radiative, Auger, and surface recombination, full acceptor and donor trap dynamics, and heavy doping effects [42].

ATLAS is a physically-based device simulator. A physically-based device simulator predicts the electrical characteristics that are associated with specified physical structures and bias conditions. This becomes possible when approximating the operation of a device on a two or three dimensional grid, the points of which are called nodes. By

applying a set of differential equations, derived from Maxwell's laws, onto this grid, we can simulate the transport of carriers through a structure. Therefore, the modeling of the electrical performance of a device in DC and AC, both steady state and transient, modes of operation are achievable [42].

ATLAS can be used to simulate the manufacturing, operation, and introduction of defects to the material because it can extract the electrical characteristics from any configuration of materials with which it is provided. The way solar cells are modeled in ATLAS is by means of a text input deck. The ATLAS defined solar cell structure and composition requires several parameters to be defined. These basic parameters include a two-dimensional, fine division of the overall material called a mesh, the division of that mesh into regions, the assignment of materials to each region. Next, the electrode locations must be defined. Then, doping must be introduced into the respective materials. Also, a specification of a light spectrum for simulation must be made. (For the purposes of this thesis the source is the Sun, and the AM0 spectrum is used to simulate the energy received by a solar cell in a space application.) Finally, radiation effects must be simulated by the addition of manufacturing-produced defects, which were shown to be nearly interchangeable with defects caused by radiation in Crespin's thesis [4].

C. SILVACO ATLAS INPUTS AND OUTPUTS

ATLAS conducts simulations based on a two input, three output scheme. A flow chart of how ATLAS runs a simulation

is depicted in Figure 39. ATLAS simulations use two input files: a structure file that defines the structure that will be simulated, and a text file that contains commands for ATLAS to simulate the specified device with the conditions indicated by the user. ATLAS also produces three types of output files. First is the run-time output file which provides progress, error, and warning messages as the simulation proceeds. Next is the log file which stores all terminal voltages and currents from the device analysis. Last is the solution file which stores two and three-dimensional data relating to the values of solution variables within the device at a given bias point [42].

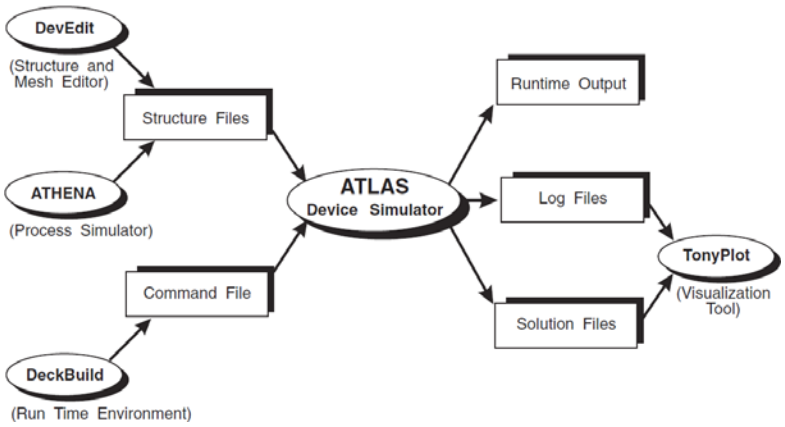

Figure 39. The input/output structure utilized by ATLAS. From [42].

D. SILVACO ATLAS INPUT DECK STRUCTURE

When starting the text input deck, the first line should always read, go atlas. This piece of input code calls ATLAS to run inside of DeckBuild. After that command statement, there is a standardized structure to follow that is outlined in Figure 40.

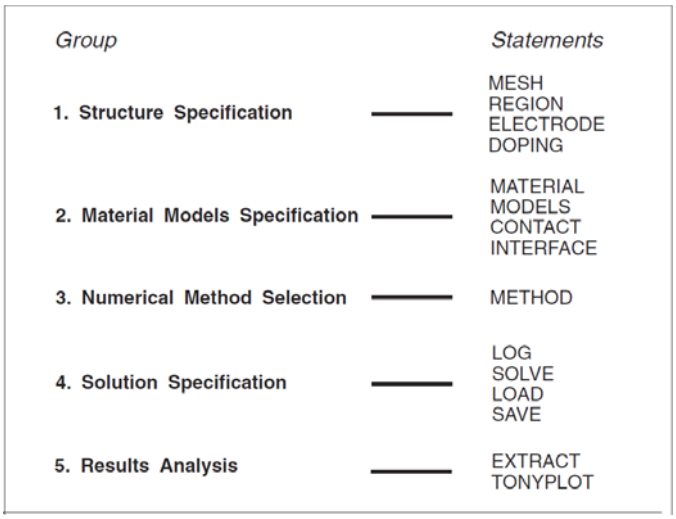

Figure 40. ATLAS input deck structure outline. From [42].

Each ATLAS statement is composed of a keyword and a set of parameters. The format is as follows:

<STATEMENT> <PARAMETER>=<VALUE>.

The following line of code is an example of the ATLAS syntax for doping a region of material:

DOPING UNIFORM N.TYPE CONCENTRATION=1.0e16 REGION=1 \
OUTFILE=my.dop.

The statement is 'DOPING', and the parameters are UNIFORM, N.TYPE, CONCENTRATION, REGION, and OUTFILE. The parameters can be classified into four groups: real, integer, character, and logical. The back slash '\' at the end of the line of code informs ATLAS that the next line of code should be considered as a part of the one preceding it. This is a useful tool because each line is limited to 256 characters and makes reading the code easier. The

'UNIFORM' and 'N.TYPE' parameters are of type logical, meaning they only have values of 'TRUE' or 'FALSE'. ATLAS automatically assigns a 'FALSE' value to a logical parameter unless otherwise instructed. The 'REGION' parameter is of type integer because it can only take on integer values. The 'CONCENTRATION' parameter is of type real, and as such, it takes floating point numbers as input values. Last, the 'OUTFILE' parameter is of type character and only takes strings as an input [42].

E. ATLAS GENERAL DEVICE CONSTRUCTION OUTLINE

1. Mesh

The first step in building a device after the go atlas statement is to define the mesh. The mesh is a grid that covers the physical area in which the device will be constructed and simulated. The mesh is simply created by a series of vertical and horizontal lines with user defined spacing between them [42].

The mesh is created with the following statements:

```
MESH SPACE.MULT=<VALUE>;

X.MESH LOCATION=<VALUE> SPACING=<VALUE>;

Y.MESH LOCATION=<VALUE> SPACING=<VALUE>.
```

The first line of code specifies a scaling factor for the mesh that is created by the X.MESH and Y.MESH commands.

The default value is one but can be changed to generate a finer mesh by substituting a value less than one or a courser mesh by substituting a value greater than one [42]. The benefit of a courser mesh is a faster simulation speed but at the cost of a less accurate model. The opposite is true for a finer mesh.

The next two lines contain the commands X.MESH and Y.MESH. They are used to specify the locations of the mesh vertical and horizontal lines in microns using the spacing defined in that line. In order for these commands to work, X.MESH and Y.MESH statements must be listed in the order of increasing *x* and *y*. Also, both negative and positive values of *x* and *y* are allowed [42]. An example of fine and course meshes created in ATLAS is illustrated in Figure 41.

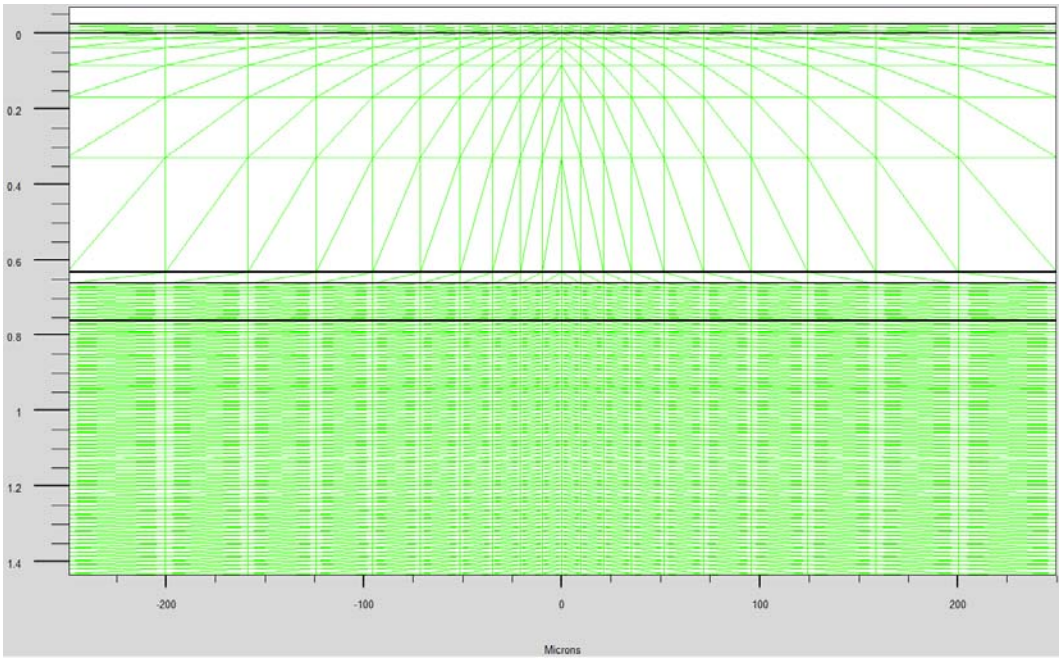

Figure 41. Fine and course meshing in ATLAS.

2. Regions

The next step in creating a semiconductor device is to separate the created mesh into regions. The format to define the regions is:

REGION number=<integer> <material_type> /

<position parameters>.

This statement can be broken up into several parts. First, the selected integer creates a region that can be referred to by that same integer. The material type determines what element or compound this region becomes and must be available in the ATLAS database. Last, the position parameters tell ATLAS which potion of the mesh that was just created will become the region. The position parameters must be contained within the bounds of the mesh that was created in the first step [42]. An example of created regions can be found in Figure 42.

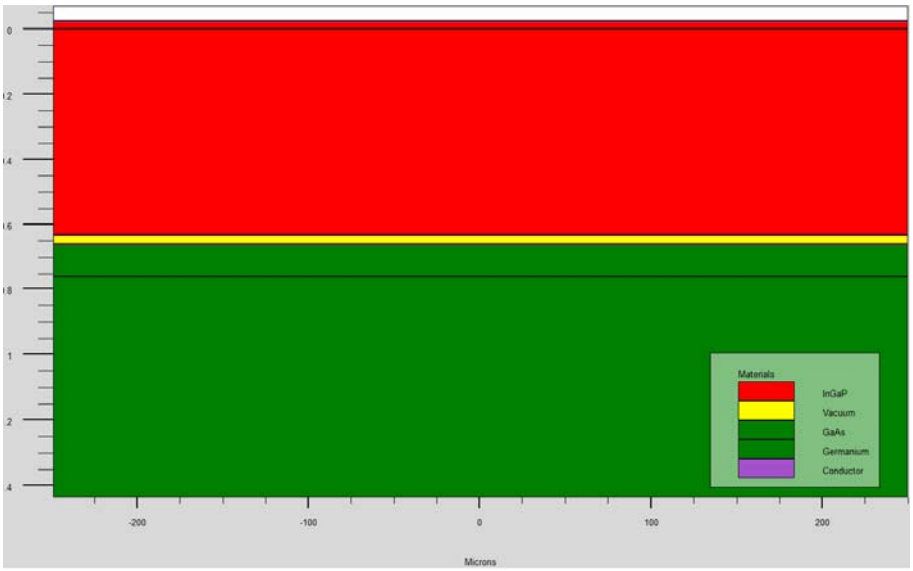

Figure 42. Regions created in a semiconductor device.

3. Contacts

After defining the regions and materials, the next step is to create contacts on the device. At least one contact must be specified in the script, up to a maximum of fifty. The ELECTRODE statement is:

ELECTRODE NAME = <electrode_name> /

<position parameters>.

The position parameters are specified using the X.MIN, X.MAX, Y.MIN, and Y.MAX parameters and have units of microns. The statement can also use the RIGHT, LEFT, TOP, and BOTTOM parameters to define the location [42]. An example of an anode and a cathode on a simple GaAs cell is depicted in Figure 43.

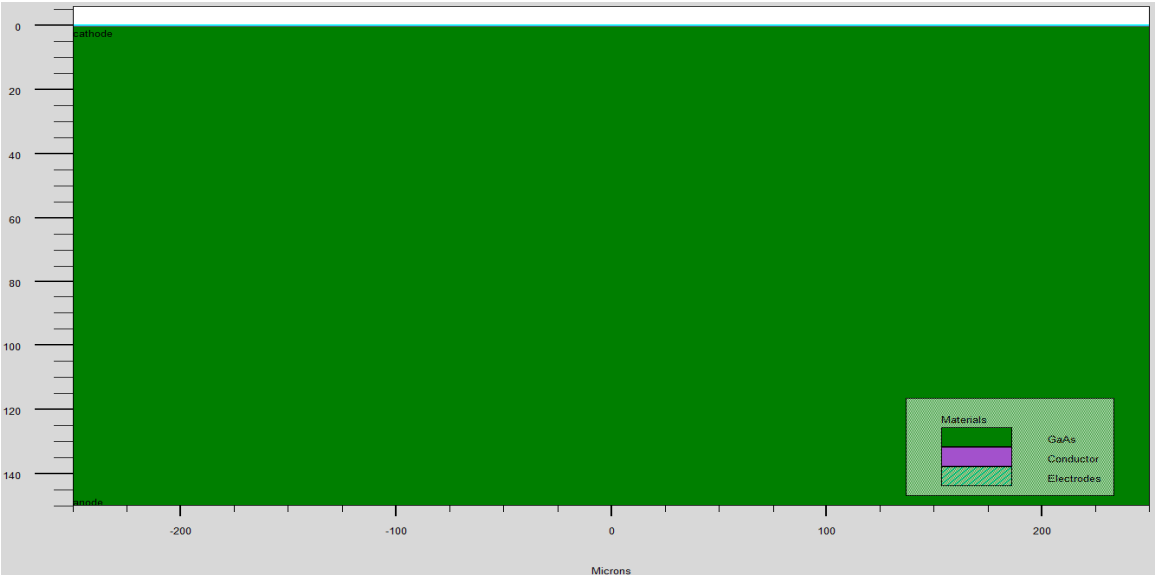

Figure 43. Contacts on a GaAs solar cell.

4. Doping

After creating the separate regions and assigning materials to those regions, the materials themselves can be doped. The user specifies the doping using the DOPING statement:

DOPING <distribution_type> <dopant_type> <position_parameters>. [42]

The DOPING statement is broken down into three sections. First, the distribution type can be either uniform, Gaussian, or complementary error function forms. Only the uniform distribution type was utilized in this thesis. Next, a concentration and type of doping must be specified. Finally, the region to be doped must be identified. A device with different doping levels in TonyPlot is illustrated in Figure 44. An example DOPING statement is:

DOPING UNIFORM CONCENTRATION=1E16 N.TYPE REGION=1.

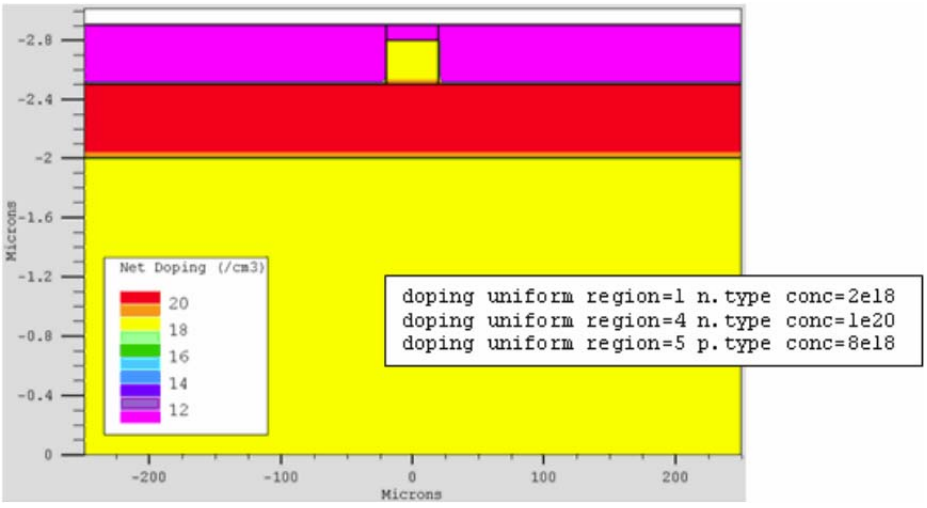

Figure 44. Doping levels in different regions. From [43].

5. Material

Once the structure is completely assembled, the materials used to construct the device must themselves be defined. The MATERIAL statement allows specification of some basic parameters. These values can apply to a material or a region [42]. The general MATERIAL statement is:

MATERIAL <localization> <material_definition>.

A specific example featuring silicon is:

MATERIAL MATERIAL=Silicon EG300=1.12 MUN=1100.

In this example the MATERIAL statement sets the band gap equal to 1.12 eV and the electron mobility to 1100 cm^2/Vs in all regions consisting of silicon throughout the entire device. If the desire is to only change material properties in one region, then the second MATERIAL from above would be replaced with a REGION statement. An example illustrating this feature is:

MATERIAL REGION=2 TAUN0=2e-7 TAUP0=1e-5.

6. Physical Models

Physical models are specified using the MODELS statement. The physical models are grouped into five classes: mobility, recombination, carrier statistics, impact ionization, and tunneling [42]. The list of physical models available to the ATLAS software can be found in the ATLAS user's manual. The general MODELS statement is:

MODELS <model_name>.

A specific example that specifies standard concentration dependent mobility, parallel field mobility, Shockley-Read-Hall recombination with fixed carrier lifetimes, and Fermi Dirac statistics is:

MODELS CONMOB FLDMOB SRH FERMIDIRAC.

7. Solution Method

ATLAS contains several numerical methods to calculate the solutions to semiconductor device problems. There are three main types of numerical methods. The first method is the GUMMEL type which is useful where the system of equations is weakly coupled but has only linear convergence. The next method is NEWTON, which is useful when the system of equations is strongly coupled and has quadratic convergence. This method causes ATLAS to spend extra time solving for quantities which are essentially constant or weakly coupled and also requires a more accurate initial guess to the problem to obtain convergence. The final method is the BLOCK method which can provide faster simulation times in situations where the NEWTON method struggles. Numerical methods are given in the METHOD statements of the input file. An example of an efficient METHOD statement is:

METHOD GUMMEL BLOCK NEWTON.

8. Solution Specification

This section of the input deck to ATLAS is where the simulation does its calculations to solve for the device specified. It is divided up into four parts: LOG, SOLVE, LOAD, and SAVE.

The LOG statement creates save file for steady-state, transient, or DC data determined by a solve statement after the log statement. An example LOG statement in which data is saved into example.log is:

```
LOG OUTFILE = example.log.
```

The SOLVE statement follows a LOG statement and calculates information at one or more bias points. An example SOLVE statement that ramps the base voltage from 0.0 V to 1.0 V with 0.05 V steps with a fixed collector voltage of 2.0 V is:

```
SOLVE VCOLLECTOR=2.0
SOLVE VBASE=0.0 VSTEP=0.05 VFINAL=1.0 NAME=base.
```

The LOAD and SAVE statements are used together to help create better initial guesses for bias points. The SAVE statement is used first to store all of the information about the bias points, and later the LOAD statement is used to retrieve that information and aid in the solution.

9. Data Extraction and Plotting

The final section of the input deck is extracting the data and plotting it in a useful way. The two statements associated with this section are EXTRACT and TONYPLOT. The EXTRACT statement is:

EXTRACT INIT INF="<filename>".

The TONYPLOT statement is:

TONYPLOT "<filename>".

F. CONCLUSION

An introduction to Silvaco's ATLAS software and the structure of its input files was given in this chapter. Also included was a walkthrough that can be followed to avoid unnecessary errors. With the toolbox that ATLAS provides, building InGaP, GaAs, and Ge solar cells individually and together in a triple junction cell, as well as the radiation effects on all four cells will be discussed in this thesis.

THIS PAGE INTENTIONALLY LEFT BLANK

VII. RESULTS OF SIMULATION

A. INDIVIDUAL INGAP SOLAR CELL

The first cell that was modeled and simulated using Silvaco ATLAS was the InGaP solar cell. The ATLAS input deck used to create it can be found in Appendix A. The I-V curve for the InGaP solar cell prior to radiation effects and then after exposure to 1 MeV electrons at three fluence levels, 10^{15} e/cm^2, 10^{16} e/cm^2, and 10^{17} e/cm^2, can be found in Figure 45. These levels were chosen because they represent the fluence levels present in the Van Allen Belts. The five most important characteristics of the InGaP solar cell based on the level of radiation are organized in Table 1.

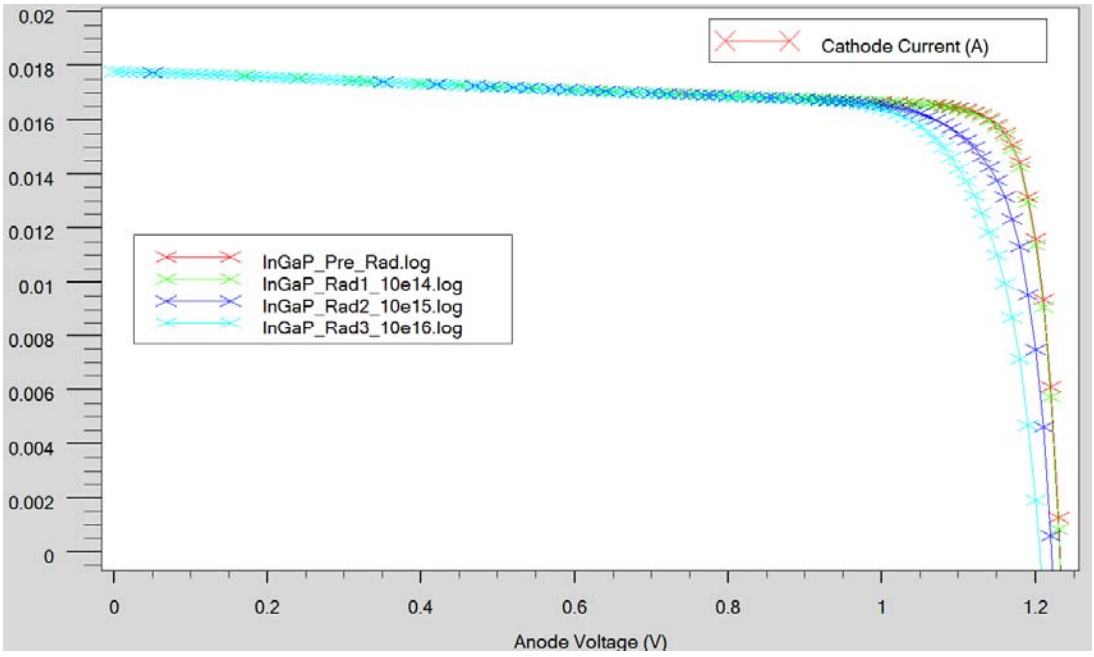

Figure 45. I-V characteristics of an InGaP solar cell with and without radiation effects.

Table 1. InGaP solar cell characteristics.

InGaP				
Fluence (e/cm^2)	Pre-Radiation	10^{15}	10^{16}	10^{17}
I_{sc} (A)	0.0178	0.0178	0.0178	0.0178
V_{oc} (V)	1.232	1.231	1.221	1.2052
P_{max} (W/cm^2)	0.0183	0.0182	0.0171	0.0166
FF	0.8358	0.8326	.7887	0.7736
Efficiency (%)	13.4	13.3	12.5	12.1

B. INDIVIDUAL GAAS SOLAR CELL

The next cell that was modeled was the GaAs solar cell. The ATLAS input deck used to create it can be found in Appendix A. The I-V curve for the GaAs solar cell prior to radiation effects and then after exposure to 1 MeV electrons at three fluence levels, 10^{15} e/cm^2, 10^{16} e/cm^2, and 10^{17} e/cm^2, is shown in Figure 46. The five most important characteristics of the GaAs solar cell based on the level of radiation are organized in Table 2.

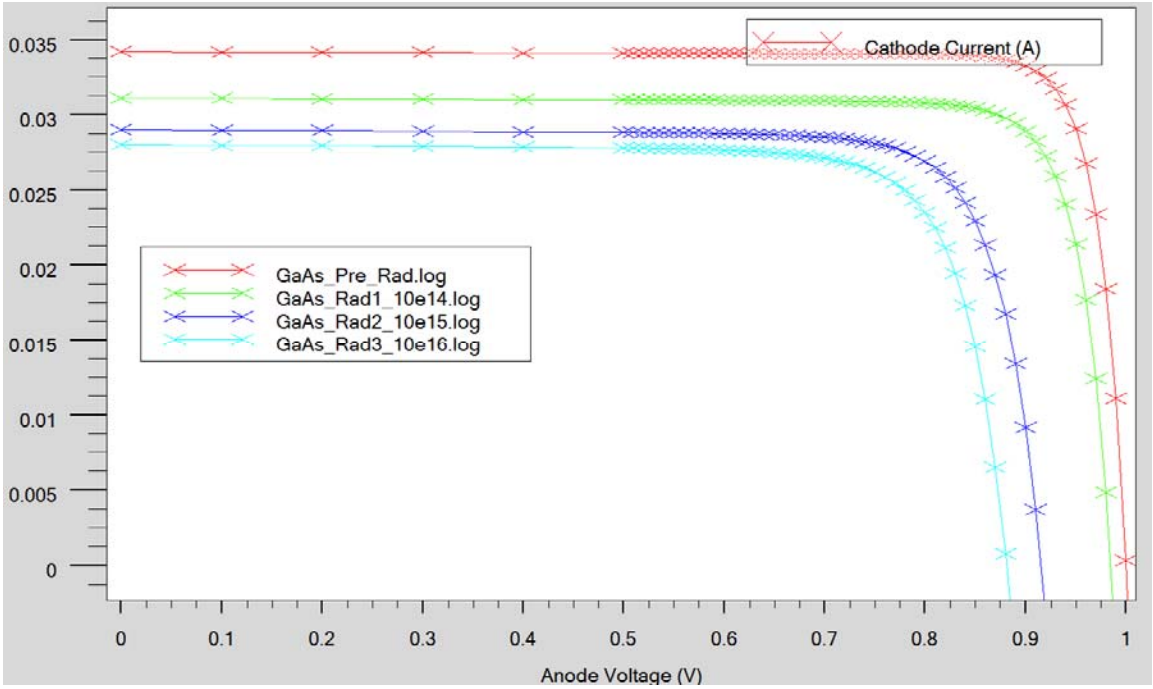

Figure 46. I-V characteristics of an GaAs solar cell with and without radiation effects.

Table 2. GaAs solar cell characteristics.

GaAs				
Fluence (e/cm^2)	Pre-Radiation	10^{15}	10^{16}	10^{17}
I_{sc} (A)	0.0342	0.0311	0.029	0.028
V_{oc} (V)	1.0002	0.9845	0.9153	0.881
P_{max} (W/cm^2)	0.0299	0.0262	0.0216	0.0197
FF	0.8766	0.8564	0.8115	0.7969
Efficiency (%)	21.97	19.22	15.79	14.41

C. INDIVIDUAL GE SOLAR CELL

The last cell that was modeled individually was the Ge solar cell. The ATLAS input deck used to create it can be found in Appendix A. The I-V curve for the InGaP solar cell prior to radiation effects and then after exposure to 1 MeV electrons at three fluence levels, 10^{15} e/cm^2, 10^{16} e/cm^2, and 10^{17} e/cm^2, can be found in Figure 47. The five most important characteristics of the Ge solar cell based on the level of radiation are organized in Table 3.

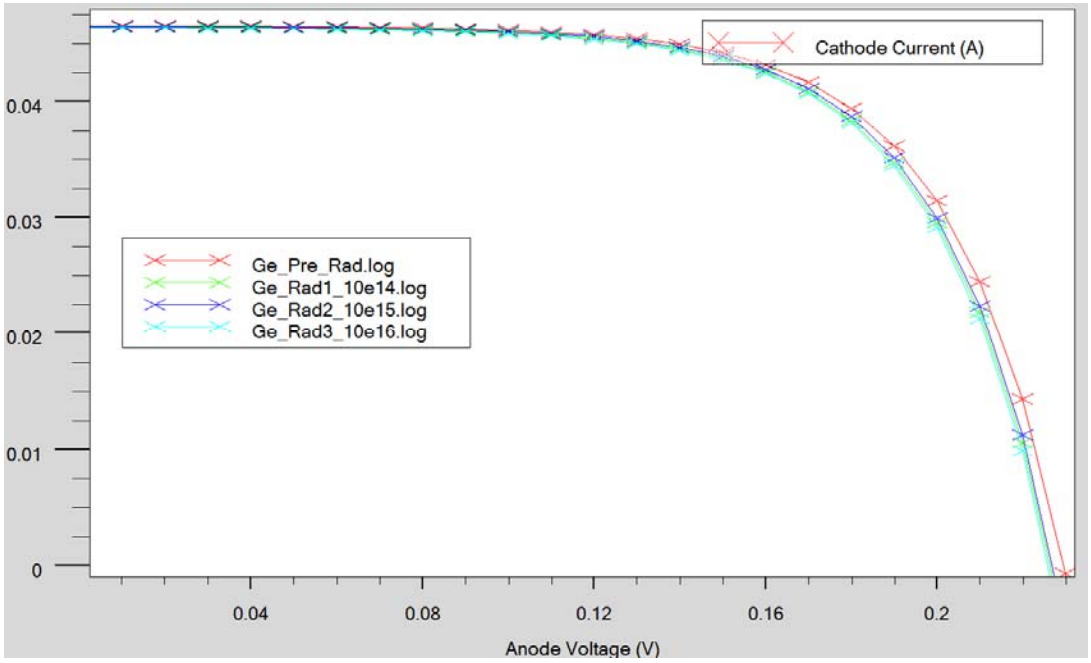

Figure 47. I-V characteristics of a Ge solar cell with and without radiation effects.

Table 3. Ge solar cell characteristics.

Ge				
Fluence (e/cm^2)	Pre-Radiation	10^{15}	10^{16}	10^{17}
I_{sc} (A)	0.0475	0.0474	0.0474	0.0473
V_{oc} (V)	0.2296	0.2264	0.2269	0.2259
P_{max} (W/cm^2)	0.0071	0.0069	0.007	0.0069
FF	0.65	0.6469	0.6494	0.6466
Efficiency (%)	5.19	5.08	5.11	5.05

D. INGAP/GAAS/GE TRIPLE JUNCTION SOLAR CELL

Once the three materials had each been built, modeled, and verified, the final step was to build the overall triple junction cell. The means by which this was accomplished was starting with a layer of InGaP on top, a layer of GaAs in the middle, and a bottom layer consisting of Ge. A vacuum was placed in between these layers to simulate the tunnel junctions of the solar cell. The ATLAS structure file representation of the triple junction cell is shown in Figure 48.

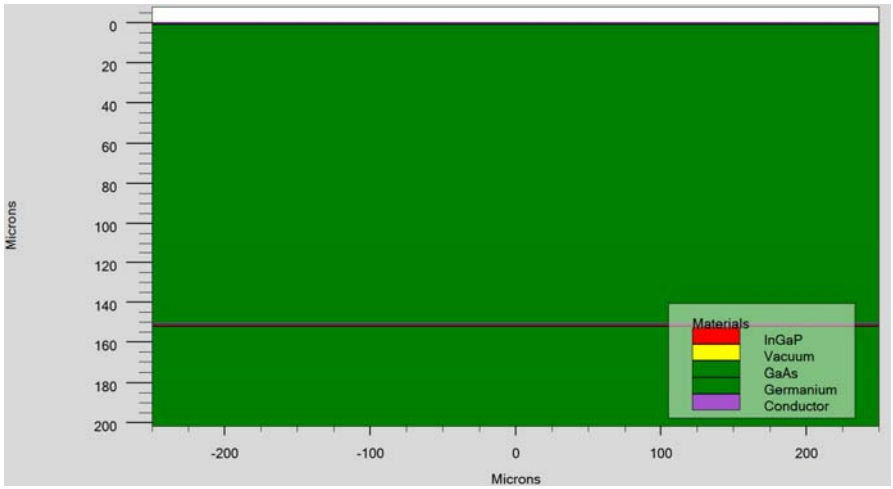

Figure 48. Silvaco ATLAS structure file of the triple junction cell.

In order to extract an overall I-V curve, three sets of anodes and cathodes were placed on the top, middle, and bottom layers of the cell, which then obtained three I-V curves. Before combining the data to achieve one overall curve, the three curves were compared to their respective individual cell to ensure that the middle and bottom layers' I-V characteristics had degraded due to the top layer absorbing some of the incident light. A comparison of the output of top layer and the InGaP solar cell is shown in Figure 49. These two curves are identical because they have the same parameters and the same incident light shone on them. A comparison of the outputs of the middle layer to the GaAs solar cell and the bottom layer to the Ge solar cell are found in Figures 50 and 51. In these two comparisons, it can be clearly seen that the effect of placing a layer above it significantly reduces the characteristics of that cell; however, having this extra power absorption available is what makes the triple junction cell more efficient than a single cell.

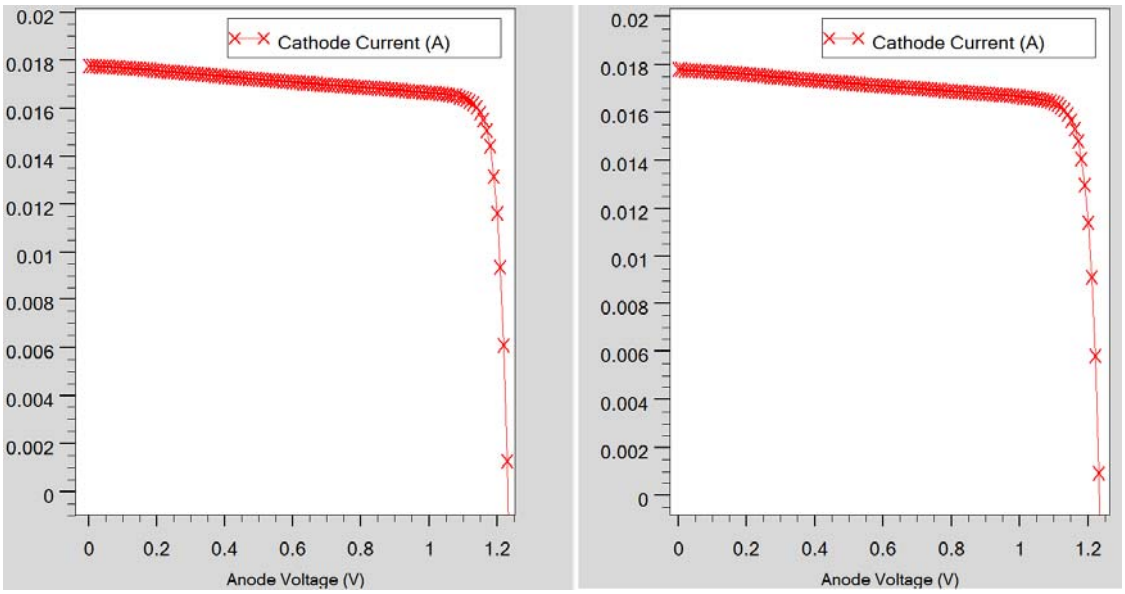

Figure 49. A comparison of the outputs of an InGaP solar cell and the top layer of the triple junction cell.

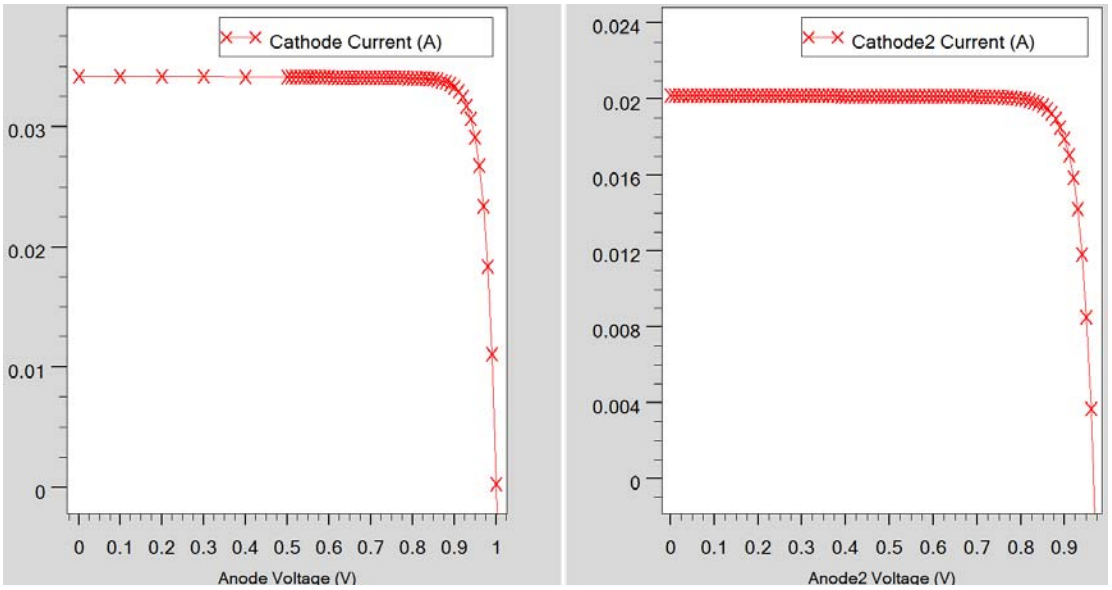

Figure 50. A comparison of the outputs of a GaAs solar cell and the middle layer of the triple junction cell.

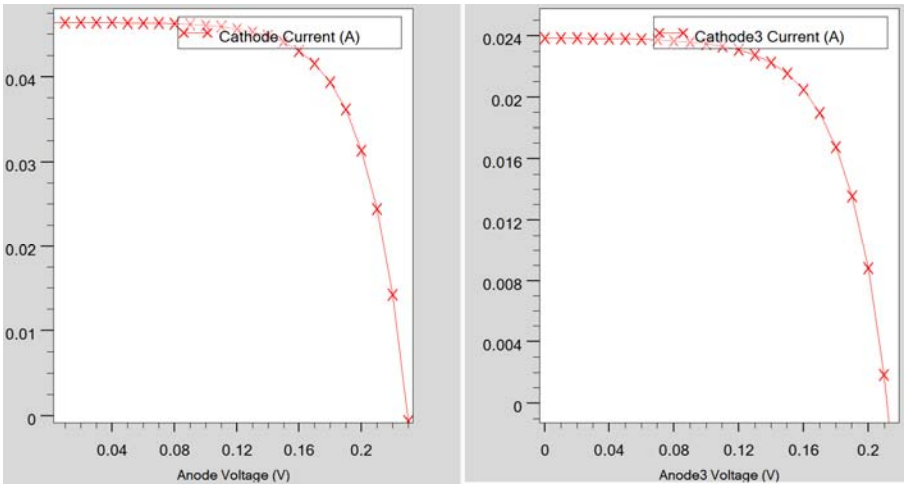

Figure 51. A comparison of the outputs of a Ge solar cell the bottom layer of the triple junction cell.

The next step in modeling the effects of radiation on triple junction solar cells was to implement the defects into the cells individually and extract the resulting I-V curves to ensure the performance had degraded. The effects of radiation on the output performance of the InGaP, GaAs, and Ge cells are illustrated in Figures 52 through 54.

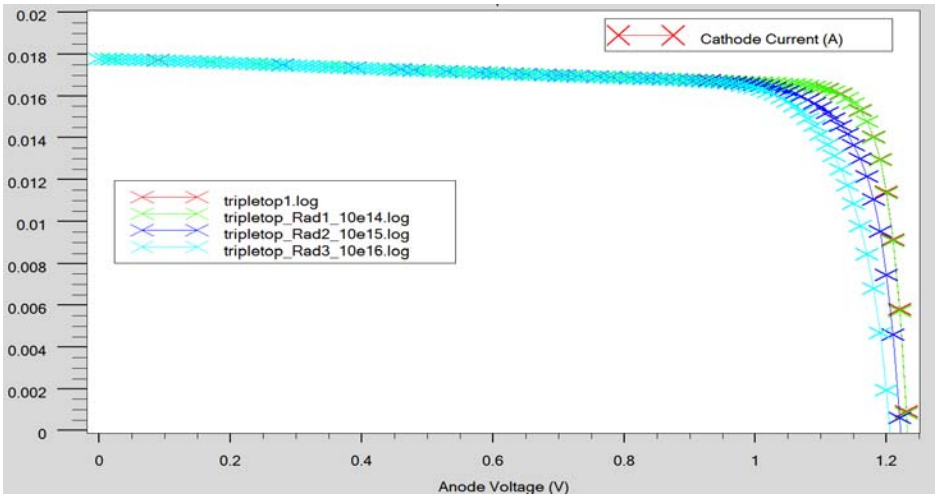

Figure 52. I-V curves from the top layer (InGaP) of the triple junction solar cell with and without radiation damage.

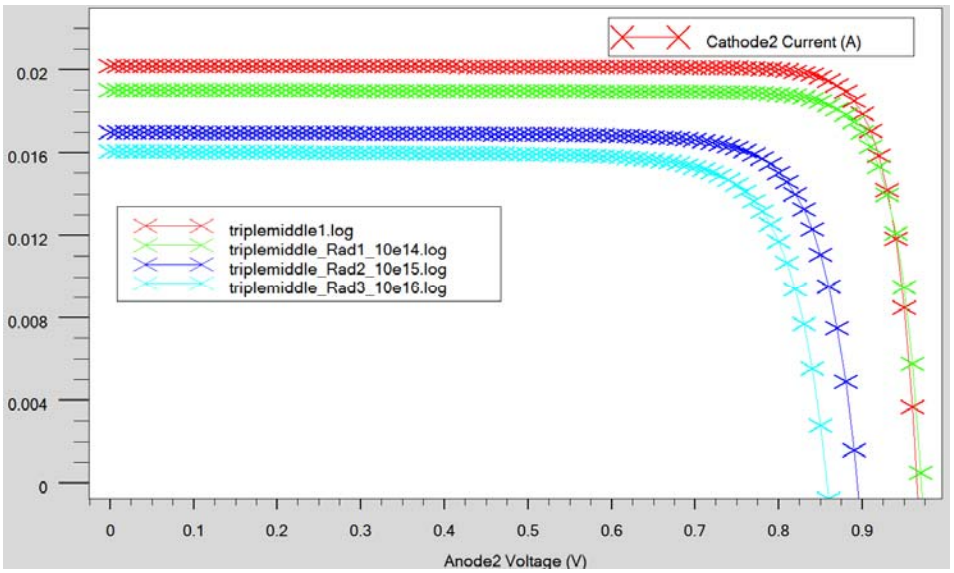

Figure 53. I-V curves from the middle layer (GaAs) of the triple junction solar cell with and without radiation damage.

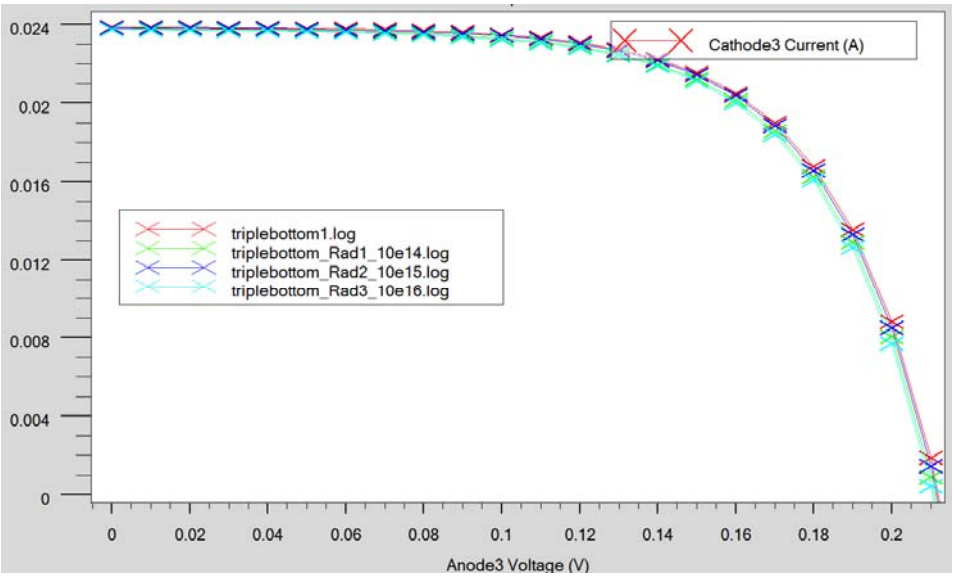

Figure 54. I-V curves from the bottom layer (Ge) of the triple junction solar cell with and without radiation damage.

Finally, the last step was to import the three sets of data into MATLAB in order to combine them into one set of

data that represented the overall I-V curve of the triple junction solar cell. Since triple junction solar cells consist of a series connected stack, the voltages of each layer add together but the lowest overall current produced by each cell is used. The overall I-V curves of the triple junction cell before radiation damage and after the three fluence levels described before were applied are shown in Figure 55. The important characteristics of the triple junction solar cell at the different levels of radiation are organized in Table 4.

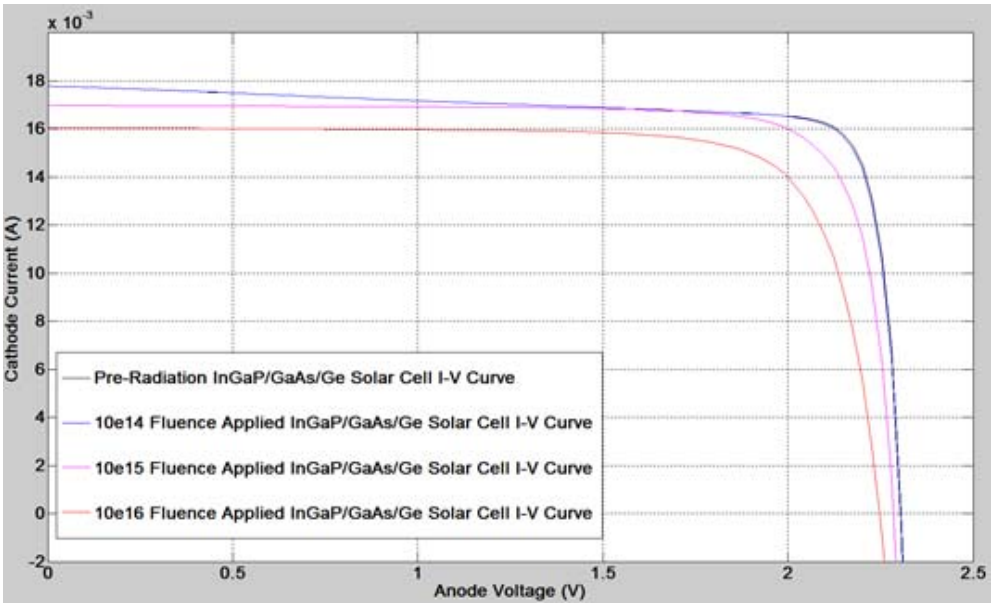

Figure 55. The overall I-V curves from the simulated triple junction solar cell with and without radiation damage.

Table 4. Triple junction solar cell characteristics.

InGaP/GaAs/Ge				
Fluence (e/cm^2)	Pre-Radiation	10^{15}	10^{16}	10^{17}
I_{sc} (A)	0.0178	0.0178	0.017	0.0161
V_{oc} (V)	2.3056	2.0294	2.0173	2.0068
P_{max} (W/cm^2)	0.0342	0.034	0.032	0.0285
FF	0.8337	0.8297	0.817	0.7694
Efficiency (%)	25.13	25.01	23.53	20.95

E. DISCUSSION OF RESULTS

To validate the results of this model of a triple junction solar cell, certain characteristics that were determined from the simulation were compared to a paper published by the Tsukuba Space Center in Japan [44]. A comparison of their solar cell's I-V curve and the one created by the simulation can be seen in Figures 56 and 57. The short-circuit current, open-circuit voltage, and maximum power measurements from the experimental cell over a spectrum of electron magnitudes and fluence levels are shown in Figures 58 through 60. Because the cells were not made with exactly the same parameters, there is a difference between the two I-V curves found in Figures 56 and 57. This difference is small and the assumption can be made that the simulation matches well to the results of the experiment in Japan.

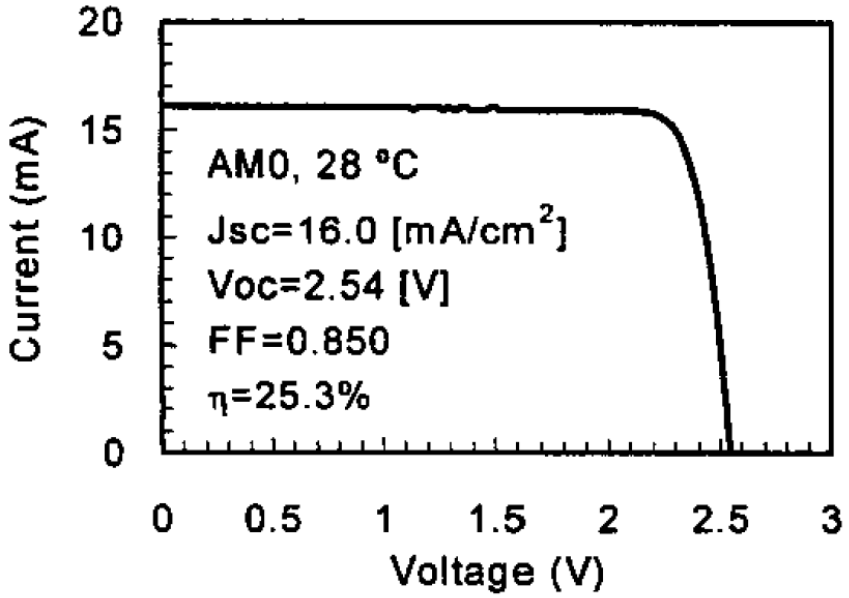

Figure 56. Triple junction solar cell I-V curve. From [44].

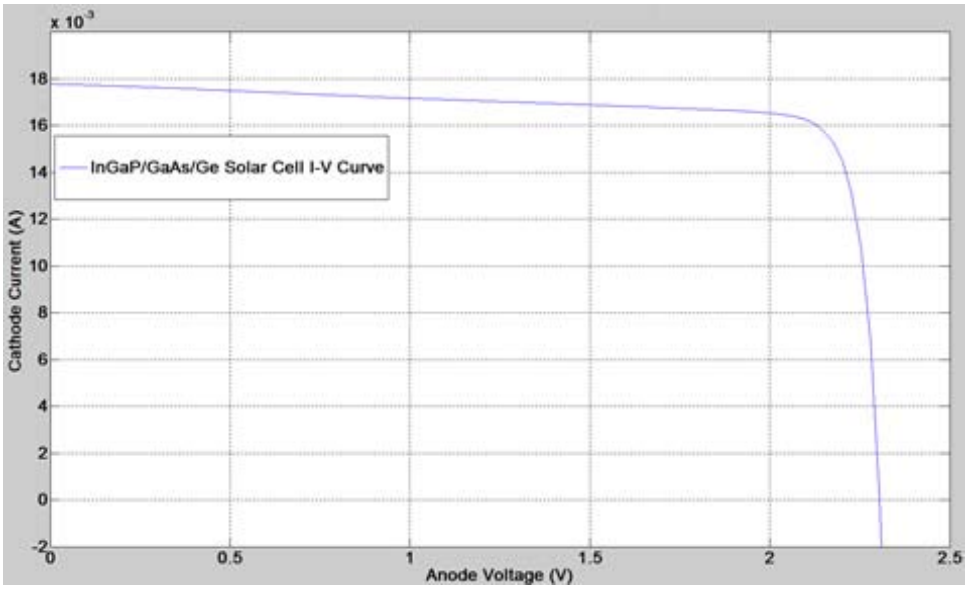

Figure 57. Triple junction solar cell I-V curve from Silvaco ATLAS simulation.

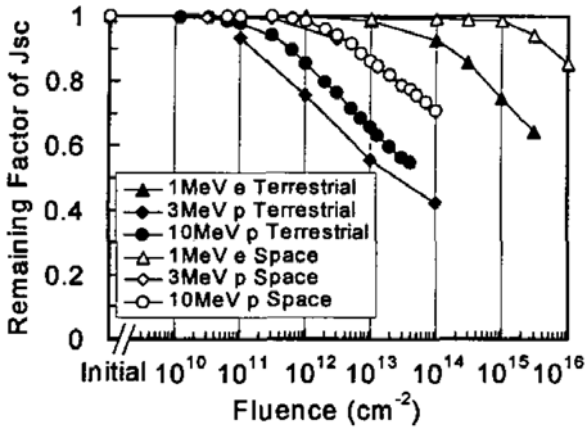

Figure 58. Remaining short circuit current after different levels of radiation. From [44].

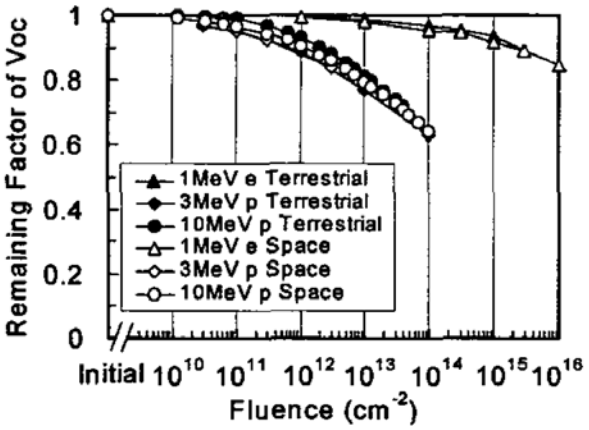

Figure 59. Remaining open circuit voltage after different levels of radiation. From [44].

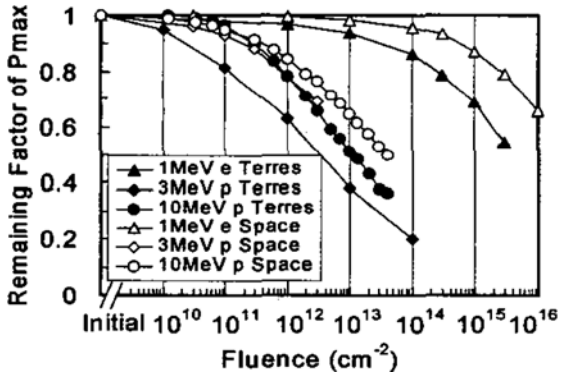

Figure 60. Remaining maximum power after different levels of radiation. From [44]

The data gleaned from Figures 58 through 60 is organized into Table 5 in order to be compared to the characteristics obtained from the ATLAS simulation and data processing in MATLAB. Table 4 is useful in showing the characteristics of the simulated triple junction solar cell, and the data contained within it was used to create Table 6. The effect of each level of radiation on the triple junction solar cell performance characteristics, in percentages, is organized in Table 6.

Table 5. Data from [44] triple junction solar cell.

Triple Junction Cell Performance Characteristics as a Percentage of the Pre-Radiation Cell Characteristics from [44]			
Fluence Level	10^{15}	10^{16}	10^{17}
I_{sc}	100%	97%	89%
V_{oc}	95%	90%	84%
P_{max}	96%	90%	65%

Table 6. Data from the Silvaco ATLAS simulation triple junction solar cell.

Triple Junction Cell Performance Characteristics as a Percentage of the Pre-Radiation Cell from Silvaco ATLAS			
Fluence Level	10^{15}	10^{16}	10^{17}
I_{sc}	100%	95.5%	90.4%
V_{oc}	88%	87.5%	87%
P_{max}	99.4%	93.6%	83%

VIII. CONCLUSIONS AND RECOMMENDATIONS

Measurable trap data was utilized as a means to predict the degradation effects on the output characteristics of a solar cell in this thesis. This methodology is useful to the research and design of solar cells for both civilian and military applications because of the reduced time and costs associated with this process. Published experimental information and measurements were used in this thesis in the attempt to model the effects of radiation on InGaP, Ge, GaAs, and the triple junction cell.

The experimental measurements for this thesis were obtained from two primary publications. The first source provided the trap levels associated with the varying fluence levels that are found in space. The second provided experimental results used to verify the results of the overall simulated triple junction cell.

Combining these resources in conjunction with work from prior theses, we modeled, tested, and verified the four virtual solar cells. The solar cell models were built based on previous work but were altered to gain more favorable characteristics. Each cell was then subjected to light with the AM0 spectrum. These cells all showed accurate values for short-circuit current, open circuit voltage, maximum power, and efficiency. After creating the cells, the experimentally derived trap levels were implemented into each cell. Again, all of the cells produced accurate results over the three fluence levels examined.

It was determined through simulation and experimental results that the GaAs layer of the triple junction solar cell was the only one to exhibit appreciable change in its characteristics when irradiated at the fluence levels discussed earlier. Due to this phenomenon, a comparison of the short circuit current, the open circuit voltage, and the maximum power under three fluence levels from a simulation of this material was compared to those of the experimentally determined properties. The comparison of the results of the simulation and experiment are organized in Table 7. This juxtaposition is illustrated in Figures 60 through 63. After examining these figures, we can conclude that the characteristics from the simulation closely match the experimental values. The differences in the values at the 10^{17} fluence level are due to the simulated cell having a higher efficiency than the experimental cell due to some of the simulated cell's idealized parameters. A more accurate calculation may have been possible if recombination models could be applied to specific trap statements instead of across entire regions of material. As an added measure of validation, the response of the short circuit current, open circuit voltage, and the maximum power of a GaAs solar cell to radiation can be found in Figures 64 through 66. These curves can be found in NASA's *Solar Cell Radiation Handbook* [45] published from the work done at the NASA Jet Propulsion Laboratory in California.

Table 7. Comparison of important characteristics of the simulated and experimental GaAs solar cells.

GaAs						
Parameter	1 Mev $\Phi e = 10^{15}$ e/cm^2			1 Mev $\Phi e = 10^{16}$ e/cm^2		
	Normalized Values			Normalized Values		
	Exp [4]	Sim	Diff %	Exp [4]	Sim	Diff %
I_{SC}	.94	.909	3.2	.81	.848	4.5
V_{OC}	.97	.983	1.3	.90	.914	1.5
P_{max}, mW	.864	.876	1.4	.692	.722	4.2

GaAs			
Parameter	1 Mev $\Phi e = 10^{17}$ e/cm^2		
	Normalized Values		
	Exp [4]	Sim	Diff %
I_{SC}	.68	.819	16.9
V_{OC}	.86	.879	2.2
P_{max}, mW	.575	.659	12.7

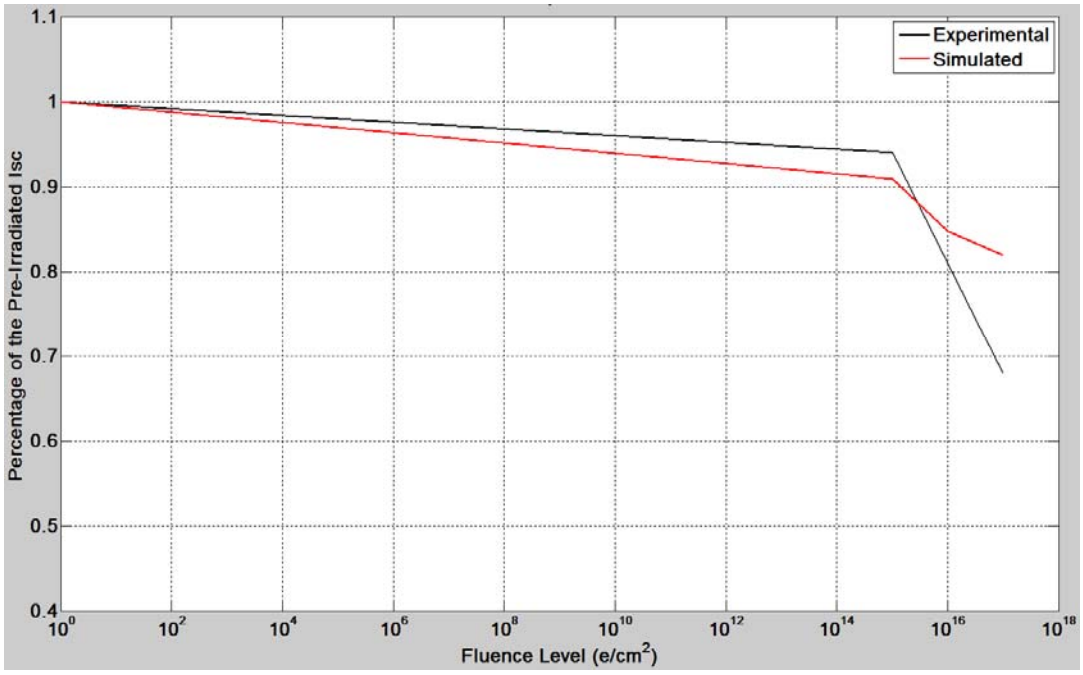

Figure 61. A comparison of the effects of radiation on the short circuit current of the experimental and simulated GaAs solar cells.

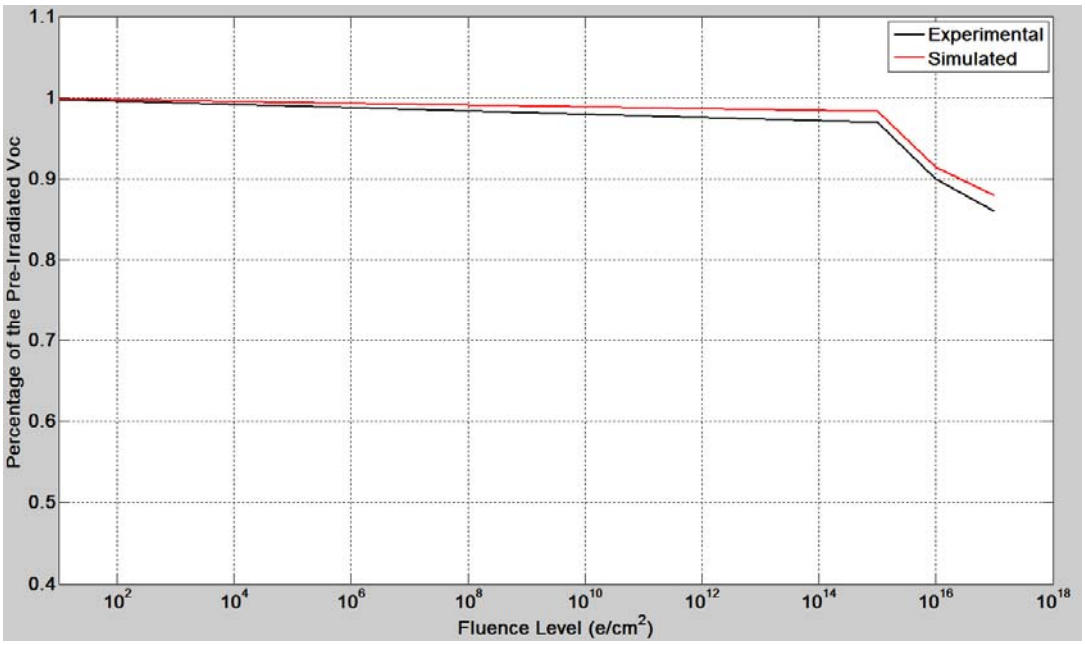

Figure 62. A comparison of the effects of radiation on the open circuit voltage of the experimental and simulated GaAs solar cells.

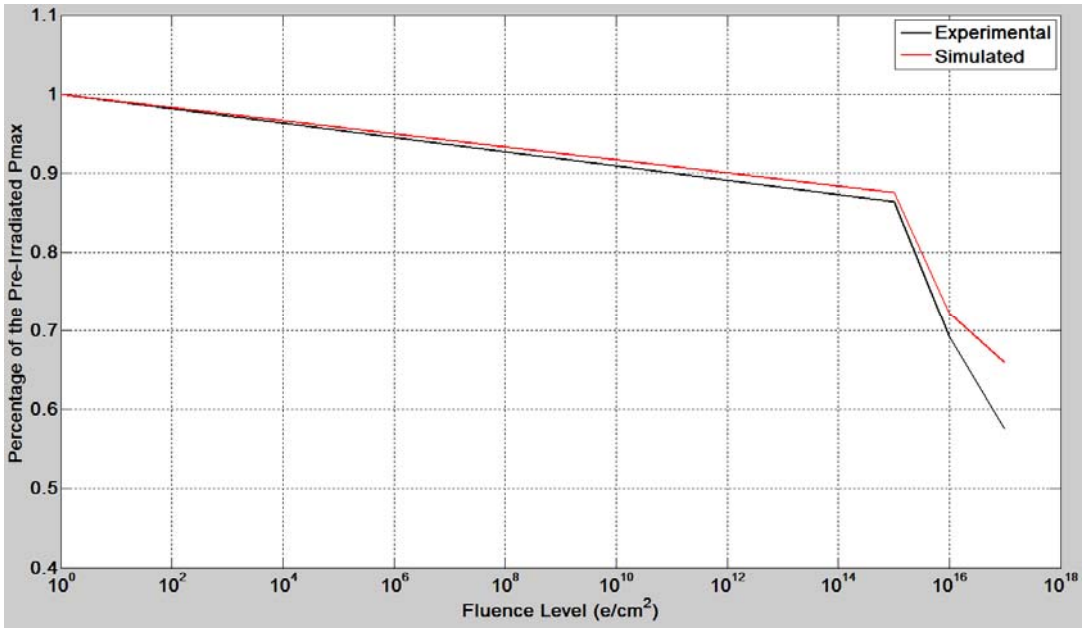

Figure 63. A comparison of the effects of radiation on the maximum power of the experimental and simulated GaAs solar cells.

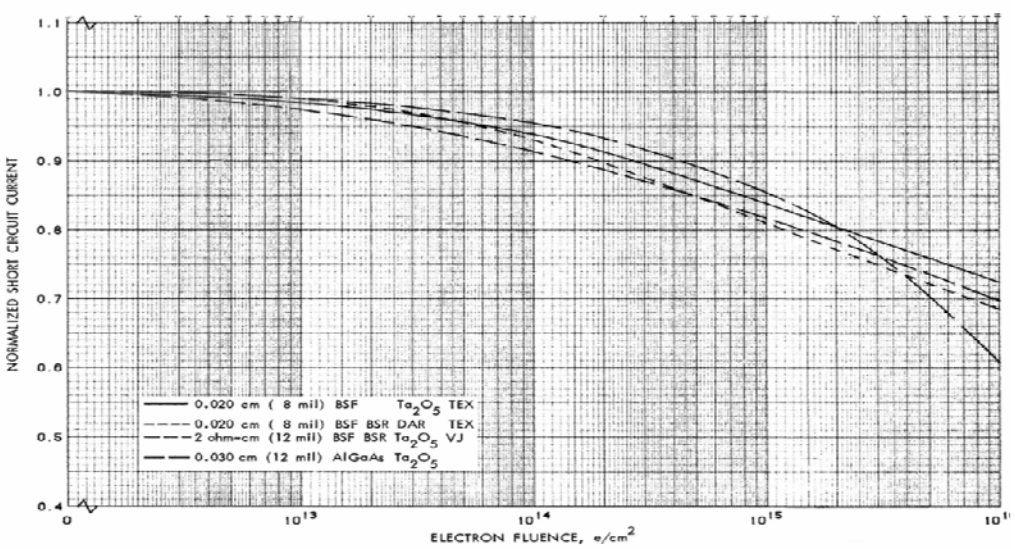

Figure 3.107 Normalized I_{SC} vs 1 MeV Electron Fluence for 10 Ohm-cm n/p Textured, 2 Ohm-cm Vertical Junction, and p/n AlGaAs Cells

Figure 64. Normalized values for short circuit current in a GaAs solar cell. From [45].

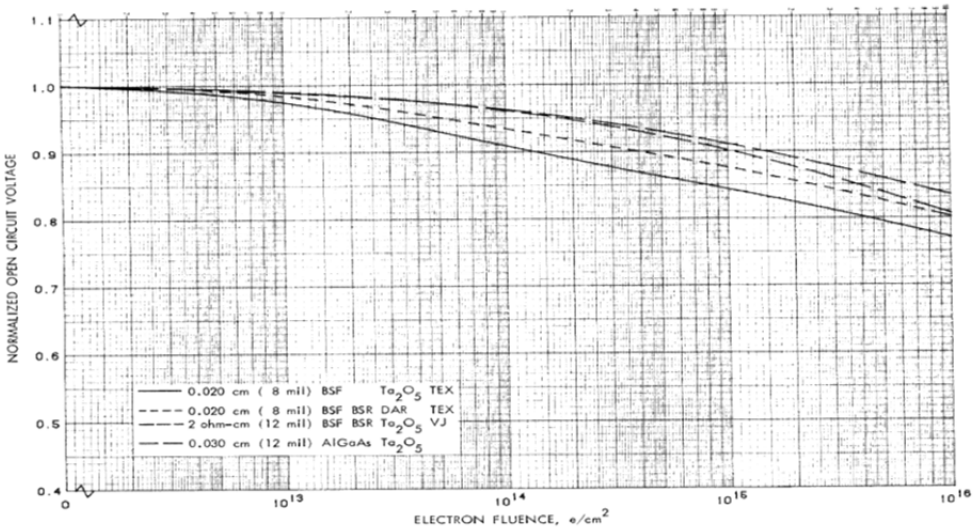

Figure 3.108 Normalized V_{OC} vs 1 MeV Electron Fluence for 10 Ohm-cm n/p Textured, 2 Ohm-cm Vertical Junction, and p/n AlGaAs Cells

Figure 65. Normalized values for open circuit voltage in a GaAs solar cell. From [45].

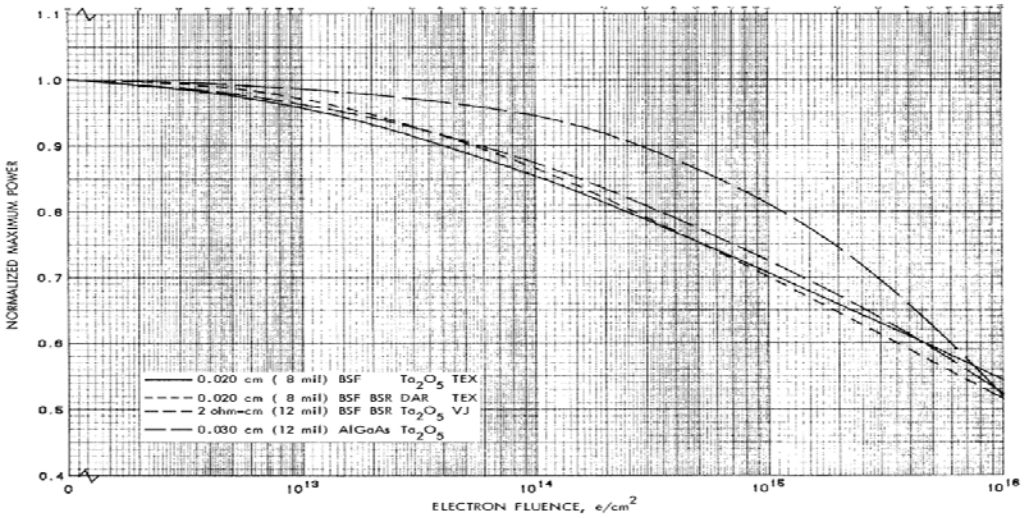

Figure 3.109 Normalized P_{max} vs 1 MeV Electron Fluence for 10 Ohm-cm n/p Textured, 2 Ohm-cm Vertical Junction, and p/n AlGaAs Cells

Figure 66. Normalized values for maximum power in a GaAs solar cell. From [45].

The short circuit current, the open circuit voltage, and the maximum power of experimental and simulated triple junction solar cells are compared in Table 8 and illustrated in Figures 64 through 66. Upon examination of these figures, we can conclude that the simulation matched the experimental results well. Again, the differences in the results of the simulated and experimental triple junction solar cells were due to the different composition of the cells, the idealized parameters of the simulated solar cell giving it a higher efficiency, and the inability to apply recombination models to specific trap statements.

Table 8. Comparison of important characteristics of the simulated and experimental triple junction solar cells.

InGaP/GaAs/Ge						
Parameter	1 Mev Φe = 10^{15} e/cm^2			1 Mev Φe = 10^{16} e/cm^2		
	Normalized Values			Normalized Values		
	Exp [44]	Sim	Diff %	Exp [44]	Sim	Diff %
I_{SC}	1	1	0	.97	.955	1.5
V_{OC}	.95	.88	7.4	.90	.875	2.8
P_{max}, mW	.96	.994	3.4	.90	.936	3.8

InGaP/GaAs/Ge			
Parameter	1 Mev Φe = 10^{17} e/cm^2		
	Normalized Values		
	Exp [44]	Sim	Diff %
I_{SC}	.89	.904	1.5
V_{OC}	.84	.87	3.4
P_{max}, mW	.65	.83	21.7

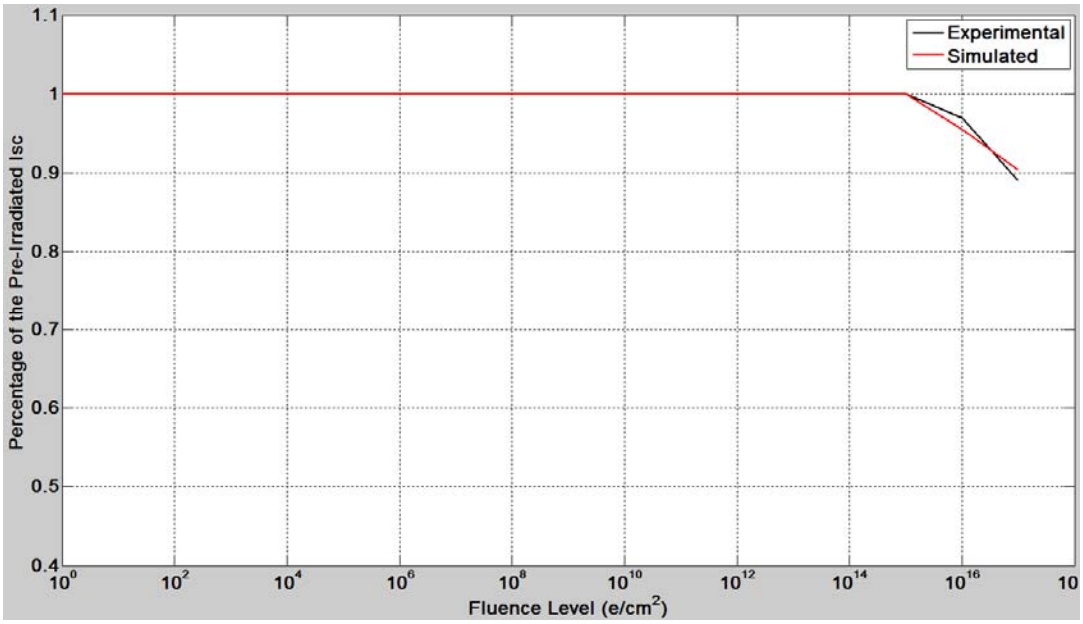

Figure 67. A comparison of the effects of radiation on the short circuit current of the experimental and simulated triple junction solar cells.

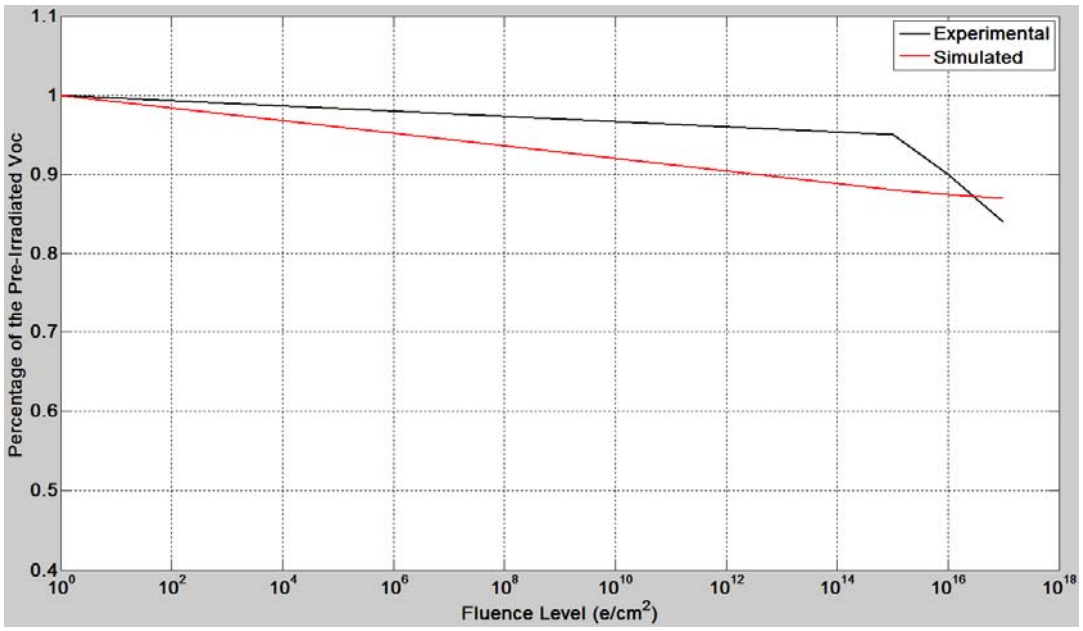

Figure 68. A comparison of the effects of radiation on the open circuit voltage of the experimental and simulated triple junction solar cells.

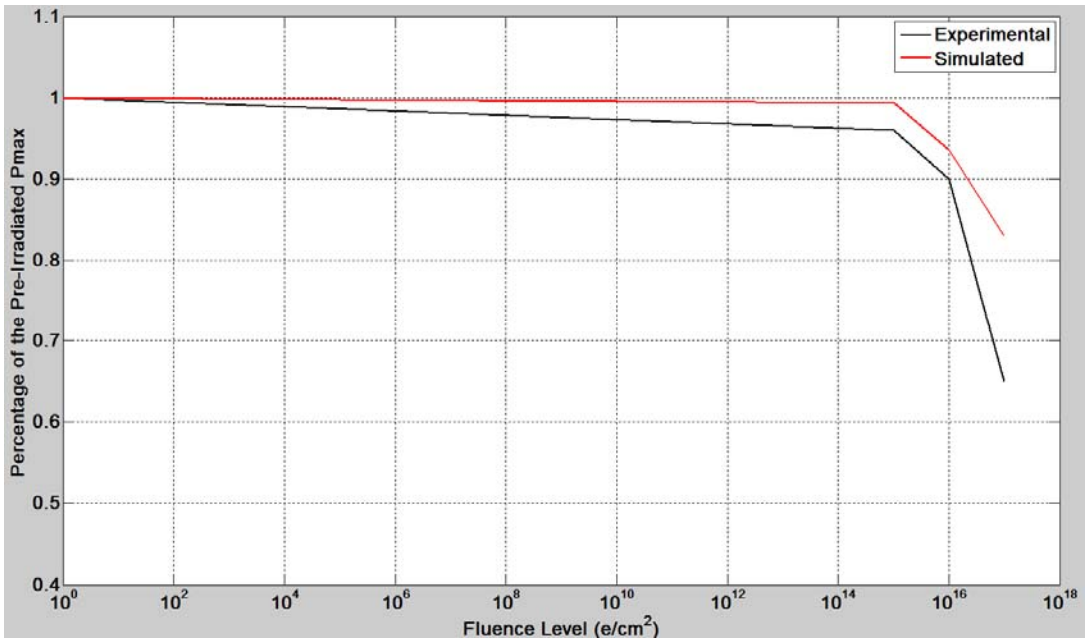

Figure 69. A comparison of the effects of radiation on the maximum power of the experimental and simulated triple junction solar cells.

The only limiting factor for this thesis was the lack of trap data for the InGaP and Ge solar cells. Fortunately, these two materials are considerably more resistant to the effects of radiation, and it was acceptable to model them using the same trap levels found in GaAs. A recommendation for future work is to make a high-efficiency multi-junction solar cell with previously determined trap level data and apply this technique to model the effects of radiation on that cell.

THIS PAGE INTENTIONALLY LEFT BLANK

APPENDIX A. ATLAS SOURCE CODE

A. INGAP SOLAR CELL INPUT DECK

```
go atlas

#Definition of constants
#Mesh
#X-mesh
#Y-Mesh
#Regions
#Electrodes
#Doping
#Material Properties
#Models
#Light Beams
#Solving

#Meshing
mesh width=200000

#X-Mesh: Surface=500 um2 = 1/200000 cm2
x.mesh loc=-250 spac=50
x.mesh loc=0 spac=10
x.mesh loc=250 spac=50

#Y-Mesh
#Vacuum
y.mesh loc=-0.025 spac=.17
#Emitter
y.mesh loc=0 spac=0.01
#Base
y.mesh loc=.63 spac=0.3

#Regions
#Emitter
region num=1 material=InGaP x.min=-250 x.max=250 y.min=-0.17 y.max=0
#Collector
region num=2 material=InGaP x.min=-250 x.max=250 y.min=0 y.max=.63

#Electrodes
electrode name=cathode top
electrode name=anode bottom

#Doping
doping uniform region=1 n.type conc=2e18
doping uniform region=2 p.type conc=1e17

#Material Properties
material TAUN=1e-7 TAUP=1e-7 COPT=1.5e-10 AUGN=8.3e-32 AUGP=1.8e-31

#Vacuum
material material=Vacuum real.index=3.3 imag.index=0

#InGaP
material material=InGaP EG300=1.9 PERMITTIVITY=11.62 AFFINITY=4.16
material material=InGaP MUN=1945 MUP=141
```

```
material material=InGaP NC300=1.3e20 NV300=1.28e19
material material=InGaP index.file=solarex04.nk

output con.band val.band

#Models
models BBT.KL


#Light Beams
beam num=1  am0  wavel.start=0.21  wavel.end=4  wavel.num=50

#Output and Display Structure File
struct outfile=InGaP_Pre_Rad_Structure
#tonyplot InGaP_Pre_Rad_Structure

#Solve I-V Curve
log outfile=InGaP_Pre_Rad.log
solve init
method gummel maxtraps=10 itlimit=25
solve B1=1.0
solve vanode=0 name=anode vstep=0.01 vfinal=1.4
extract name="IV" curve(v."anode", i."cathode")

#Solve Spectrum Response
beam num=1 wavelength=0.3
log outfile=InGaP_Spectrum.log
solve b1=0.001 beam=1  lambda=0.3  wstep=0.02  wfinal=1

#Solve Photogeneration
solve b1=1 lambda=0.6
struct outfile=InGaP_Photogeneration_0.6.str

#Plot
Tonyplot InGaP_Pre_Rad.log
Tonyplot InGaP_Spectrum.log
Tonyplot InGaP_Photogeneration_0.6
```

B. GAAS SOLAR CELL INPUT DECK

```
go atlas

#Definition of constants
#Mesh
#X-mesh
#Y-Mesh
#Regions
#Electrodes
#Doping
#Material Properties
#Models
#Light Beams
#Solving

#Meshing
mesh width=200000
#x-mesh: Surface=500 um2 = 1/200000 cm2

x.mesh loc=-250 spac=50
```

```
x.mesh loc=0 spac=10
x.mesh loc=250 spac=50

#Y-Mesh

#Vacuum
y.mesh loc=-0.1 spac=.01
#Emitter
y.mesh loc=0 spac=0.01
#Base
y.mesh loc=150 spac=0.3

#Regions
#Emitter
region num=1 material=GaAs x.min=-250 x.max=250 y.min=-0.1 y.max=0
#Collector
region num=2 material=GaAs x.min=-250 x.max=250 y.min=0 y.max=150

#Electrodes
electrode name=cathode top
electrode name=anode bottom

#Doping
doping uniform region=1 n.type conc=2e18
doping uniform region=2 p.type conc=1e17

#Material Properties
material TAUN=1e-7 TAUP=1e-7 COPT=1.5e-10 AUGN=8.3e-32 AUGP=1.8e-31

#Vacuum
material material=Vacuum real.index=3.3 imag.index=0

#GaAs
material material=GaAs EG300=1.42 PERMITTIVITY=13.1 AFFINITY=4.07
material material=GaAs MUN=8800 MUP=400
material material=GaAs NC300=4.7e17 NV300=7e18
material material=GaAs sopra=Gaas.nk

output con.band val.band

#Models
models BBT.KL


#Light Beams
beam num=1  am0  wavel.start=0.21  wavel.end=4  wavel.num=50

#Output and Display Structure File
struct outfile=GaAs_Pre_Rad_Structure
tonyplot GaAs_Pre_Rad_Structure

#Solve I-V Curve
log outfile=GaAs_Pre_Rad.log
solve init
method gummel maxtraps=10 itlimit=25
solve B1=1.0
solve vanode=0 name=anode vstep=0.1 vfinal=0.5
solve vanode=0.5 name=anode vstep=0.01 vfinal=1
extract name="IV" curve(v."anode", i."cathode")

#Solve Spectrum Response
beam num=1 wavelength=0.3
```

```
log outfile=GaAs_Spectrum.log
solve b1=0.001 beam=1  lambda=0.3  wstep=0.02  wfinal=1

#Solve Photogeneration
solve b1=1 lambda=0.6
struct outfile=GaAs_Photogeneration_0.6.str

#Plot
Tonyplot GaAs_Pre_Rad.log
Tonyplot GaAs_Spectrum.log
Tonyplot GaAs_Photogeneration_0.6.str
```

C. GE SOLAR CELL INPUT DECK

```
go atlas

#Definition of constants
#Mesh
#X-mesh
#Y-Mesh
#Regions
#Electrodes
#Doping
#Material Properties
#Models
#Light Beams
#Solving

#Meshing
mesh width=200000
#x-mesh: Surface=500 um2 = 1/200000 cm2

x.mesh loc=-250 spac=50
x.mesh loc=0 spac=10
x.mesh loc=250 spac=50

#Y-Mesh

#Vacuum
y.mesh loc=-1 spac=.01
#Window
y.mesh loc=0 spac=.01
#Emitter
y.mesh loc=0.2 spac=0.01
#Base
y.mesh loc=50.2 spac=0.3

#Regions
#InGaP Window
region num=1 material=InGaP x.min=-250 x.max=250 y.min=-1 y.max=0
#Emitter
region num=2 material=Ge x.min=-250 x.max=250 y.min=0 y.max=0.2
#Collector
region num=3 material=Ge x.min=-250 x.max=250 y.min=0.2 y.max=50.2

#Electrodes
electrode name=cathode top
electrode name=anode bottom

#Doping
```

```
doping uniform region=1 n.type conc=8e17
doping uniform region=2 n.type conc=6e18
doping uniform region=3 p.type conc=8.5e17

#Material Properties
material TAUN=1e-7 TAUP=1e-7 COPT=1.5e-10 AUGN=8.3e-32 AUGP=1.8e-31

#Vacuum
material material=Vacuum real.index=3.3 imag.index=0

#InGaP
material material=InGaP index.file=solarex04.nk

#Ge
material material=Ge sopra=Ge.nk

#Recombination Velocities
interface s.s y.min=0.9 y.max=1.1 s.n=1e6 s.p=1e6

output con.band val.band

#Models
models srh conmob fermi ni.fermi bgn optr auger print


#Light Beams
beam num=1  am0  wavel.start=0.21  wavel.end=4  wavel.num=50

#Output and Display Structure File
struct outfile=Ge_Pre_Rad_Structure
tonyplot Ge_Pre_Rad_Structure

#Solve I-V Curve
log outfile=Ge_Pre_Rad.log
solve init
method gummel maxtraps=10 itlimit=25
solve B1=1.0
solve vanode=0 name=anode vstep=0.01 vfinal=0.3
extract name="IV" curve(v."anode", i."cathode")

#Solve Spectrum Response
beam num=1 wavelength=0.3
log outfile=Ge_Spectrum.log
solve b1=0.001 beam=1  lambda=0.3  wstep=0.02  wfinal=1

#Solve Photogeneration
solve b1=1 lambda=0.6
struct outfile=Ge_Photogeneration_0.6.str

#Plot
Tonyplot Ge_Pre_Rad.log
Tonyplot Ge_Spectrum.log
Tonyplot Ge_Photogeneration_0.6.str
```

D. INGAP SOLAR CELL INPUT DECK

```
go atlas

#Definition of constants
#Mesh
#X-mesh
#Y-Mesh
#Regions
#Electrodes
#Doping
#Material Properties
#Models
#Light Beams
#Solving

#Meshing
mesh width=200000

#X-Mesh: Surface=500 um2 = 1/200000 cm2
x.mesh loc=-250 spac=50
x.mesh loc=0 spac=10
x.mesh loc=250 spac=50

#Y-Mesh
#Vacuum
y.mesh loc=-0.025 spac=.17

#Emitter
y.mesh loc=0 spac=0.01

#Base
y.mesh loc=.63 spac=0.3

#Tunnel 1-2
y.mesh loc=.66  spac=0

#Emitter 2 (GaAs)
y.mesh loc=.76    spac=0.01

#Base 2 (GaAs)
y.mesh loc=150.76  spac=0.3

#Tunnel 2-3
y.mesh loc=150.79  spac=0

#InGaP Layer
y.mesh loc=151.79 spac=.01
#Emitter
y.mesh loc=151.99 spac=0.01
#Base
y.mesh loc=201.99 spac=0.3

#Regions
#Emitter
region num=1 material=InGaP x.min=-250 x.max=250 y.min=-0.17 y.max=0

#Collector
region num=2 material=InGaP x.min=-250 x.max=250 y.min=0 y.max=.63
```

```
#Tunnel 1-2
region num=3 material=Vacuum x.min=-250 x.max=250 y.min=.63 y.max=.66

#Emitter 2(GaAs)
region num=4 material=GaAs  x.min=-250  x.max=250  y.min=.66  y.max=.76

#Base 2(GaAs)
region num=5 material=GaAs  x.min=-250  x.max=250  y.min=.76    y.max=150.76

#Tunnel 2-3
region num=6 material=Vacuum x.min=-250 x.max=250 y.min=150.76 y.max=150.79

#InGaP Layer
region num=7 material=InGaP x.min=-250 x.max=250 y.min=150.79 y.max=151.79

#Emitter
region num=8 material=Ge x.min=-250 x.max=250 y.min=151.79 y.max=151.99

#Collector
region num=9 material=Ge x.min=-250 x.max=250 y.min=151.99 y.max=201.99

#Electrodes
electrode name=cathode1 top
electrode name=anode1 x.min=-250 x.max=250 y.min=.63 y.max=.63

electrode name=cathode2 x.min=-250 x.max=250 y.min=.66 y.max=.66
electrode name=anode2 x.min=-250 x.max=250 y.min=150.76 y.max=150.76

electrode name=cathode3 x.min=-250 x.max=250 y.min=150.79 y.max=150.79
electrode name=anode3 bottom

#Doping
doping uniform region=1 n.type conc=2e18
doping uniform region=2 p.type conc=1e17
doping uniform region=4 n.type  conc=2e18
doping uniform region=5 p.type  conc=1e17
doping uniform region=7 n.type conc=8e17
doping uniform region=8 n.type conc=6e18
doping uniform region=9 p.type conc=8.5e17


#Material Properties
material TAUN=1e-7 TAUP=1e-7 COPT=1.5e-10 AUGN=8.3e-32 AUGP=1.8e-31

#Vacuum
material material=Vacuum real.index=3.3 imag.index=0

#InGaP
material material=InGaP EG300=1.9 PERMITTIVITY=11.62 AFFINITY=4.16
material material=InGaP  MUN=1945 MUP=141
material material=InGaP NC300=1.3e20 NV300=1.28e19
material material=InGaP index.file=solarex04.nk

#GaAs
material material=GaAs EG300=1.42   PERMITTIVITY=13.1   AFFINITY=4.07
material material=GaAs   MUN=8800   MUP=400
material material=GaAs   NC300=4.7e17  NV300=7e18
material material=GaAs   sopra=Gaas.nk

#Ge
material material=germanium sopra=Ge.nk
```

```
output con.band val.band

#Models
models BBT.KL

#Output and Display Structure File
struct outfile=Triple_Pre_Rad_Structure
tonyplot Triple_Pre_Rad_Structure

#Light Beams
beam num=1  am0  wavel.start=0.21  wavel.end=4  wavel.num=50

#Solve Top I-V Curve
log outfile=tripletop2.log
solve init
method gummel maxtraps=10 itlimit=25
solve B1=1.0
solve vanode=0 name=anode1 vstep=0.014 vfinal=1.4
extract name="IV" curve(v."anode1", i."cathode1")

tonyplot tripletop2.log

#Solve Middle I-V Curve
log outfile=triplemiddle2.log
solve init
method gummel maxtraps=10 itlimit=25
solve B1=1.0
solve vanode=0 name=anode2 vstep=0.01 vfinal=1
extract name="IV" curve(v."anode2", i."cathode2")

tonyplot triplemiddle2.log


models srh conmob fermi ni.fermi bgn optr auger print
#Solve Bottom I-V Curve
log outfile=triplebottom2.log
solve init
method gummel maxtraps=10 itlimit=25
solve B1=1.0
solve vanode=0 name=anode3 vstep=0.0022 vfinal=.22
extract name="IV" curve(v."anode3", i."cathode3")

tonyplot triplebottom2.log
```

E. RADIATION STATEMENTS

1. 1 MeV Fluence of $10e^{14}$

```
############################################################
# Radiation effects                                        #
# 1 MeV electron Fluence level 10to14 e/cm2                #
############################################################
# Top Cell
trap acceptor e.level=0.71 density=3.0e12 degen=2 sign=4e-013 sigp=4e-015/
region=1
trap donor e.level=0.14 density=1.8e13 degen=2 sigp=5.7e-013 sign=5.7e-015/
region=2
trap donor e.level=0.41 density=8.2e13 degen=2 sigp=2.6e-013 sign=2.6e-015/
region=2
```

```
trap donor e.level=0.71 density=3.0e10 degen=2 sigp=8.3e-013 sign=8.3e-015/
region=2
trap donor e.level=0.90 density=8.8e11 degen=2 sigp=3e-011 sign=3e-013 region=2

#Middle Cell
trap acceptor e.level=0.71 density=3.0e12 degen=2 sign=4e-013 sigp=4e-015/
region=4
trap donor e.level=0.14 density=1.8e13 degen=2 sigp=5.7e-013 sign=5.7e-015/
region=5
trap donor e.level=0.41 density=8.2e13 degen=2 sigp=2.6e-013 sign=2.6e-015/
region=5
trap donor e.level=0.71 density=3.0e10 degen=2 sigp=8.3e-013 sign=8.3e-015/
region=5
trap donor e.level=0.90 density=8.8e11 degen=2 sigp=3e-011 sign=3e-013 region=5

#Bottom Cell
trap acceptor e.level=0.71 density=3.0e12 degen=2 sign=4e-013 sigp=4e-015/
region=8
trap donor e.level=0.14 density=1.8e13 degen=2 sigp=5.7e-013 sign=5.7e-015/
region=9
trap donor e.level=0.41 density=8.2e13 degen=2 sigp=2.6e-013 sign=2.6e-015/
region=9
trap donor e.level=0.71 density=3.0e10 degen=2 sigp=8.3e-013 sign=8.3e-015/
region=9
trap donor e.level=0.90 density=8.8e11 degen=2 sigp=3e-011 sign=3e-013 region=9

#Models
models BBT.KL
models region=1 CONMOB BGN SRH
models region=2 CONMOB SRH
models region=4 CONMOB BGN SRH
models region=5 CONMOB SRH
models region=8 CONMOB BGN SRH
models region=9 CONMOB SRH
models OPTR print
```

2. 1 MeV Fluence of $10e^{15}$

```
############################################################
# Radiation effects                                        #
# 1 MeV electron Fluence level 10to15 e/cm2                #
############################################################
# Top Cell
trap acceptor e.level=0.13 density=2.2e14 degen=2 sign=2.6e-015 sigp=2.6e-017/
region=1
trap acceptor e.level=0.29 density=4.0e14 degen=2 sign=2.6e-013 sigp=2.6e-015/
region=1
trap acceptor e.level=0.35 density=8.0e13 degen=2 sign=6.4e-015 sigp=6.4e-017/
region=1
trap acceptor e.level=0.71 density=6.4e13 degen=2 sign=4e-013 sigp=4e-015/
region=1
trap donor e.level=0.41 density=2.1e13 degen=2 sigp=2.6e-013 sign=2.6e-015/
region=2
trap donor e.level=0.71 density=1.7e13 degen=2 sigp=8.3e-013 sign=8.3e-015/
region=2
trap donor e.level=0.90 density=2.8e13 degen=2 sigp=3e-011 sign=3e-013 region=2

#Middle Cell
trap acceptor e.level=0.13 density=2.2e14 degen=2 sign=2.6e-015 sigp=2.6e-017/
region=4
```

```
trap acceptor e.level=0.29 density=4.0e14 degen=2 sign=2.6e-013 sigp=2.6e-015/
region=4
trap acceptor e.level=0.35 density=8.0e13 degen=2 sign=6.4e-015 sigp=6.4e-017/
region=4
trap acceptor e.level=0.71 density=6.4e13 degen=2 sign=4e-013 sigp=4e-015/
region=4
trap donor e.level=0.41 density=2.1e13 degen=2 sigp=2.6e-013 sign=2.6e-015/
region=5
trap donor e.level=0.71 density=1.7e13 degen=2 sigp=8.3e-013 sign=8.3e-015/
region=5
trap donor e.level=0.90 density=2.8e13 degen=2 sigp=3e-011 sign=3e-013 region=5

#Bottom Cell
trap acceptor e.level=0.13 density=2.2e14 degen=2 sign=2.6e-015 sigp=2.6e-017/
region=8
trap acceptor e.level=0.29 density=4.0e14 degen=2 sign=2.6e-013 sigp=2.6e-015/
region=8
trap acceptor e.level=0.35 density=8.0e13 degen=2 sign=6.4e-015 sigp=6.4e-017/
region=8
trap acceptor e.level=0.71 density=6.4e13 degen=2 sign=4e-013 sigp=4e-015/
region=8
trap donor e.level=0.41 density=2.1e13 degen=2 sigp=2.6e-013 sign=2.6e-015/
region=9
trap donor e.level=0.71 density=1.7e13 degen=2 sigp=8.3e-013 sign=8.3e-015/
region=9
trap donor e.level=0.90 density=2.8e13 degen=2 sigp=3e-011 sign=3e-013 region=9

#Models
models BBT.KL
models region=1 CONMOB BGN SRH
models region=2 CONMOB SRH
models region=4 CONMOB BGN SRH
models region=5 CONMOB SRH
models region=8 CONMOB BGN SRH
models region=9 CONMOB SRH
models OPTR print
```

3. 1 MeV Fluence of $10e^{16}$

```
############################################################
# Radiation effects                                        #
# 1 MeV electron Fluence level 10to16 e/cm2                #
############################################################
# Top Cell
trap acceptor e.level=0.13 density=8.4e14 degen=2 sign=2.6e-015 sigp=2.6e-017/
region=1
trap acceptor e.level=0.29 density=1.6e15 degen=2 sign=2.6e-013 sigp=2.6e-015/
region=1
trap acceptor e.level=0.35 density=1.0e15 degen=2 sign=6.4e-015 sigp=6.4e-017/
region=1
trap acceptor e.level=0.71 density=2.7e14 degen=2 sign=4e-013 sigp=4e-015/
region=1
trap donor e.level=0.41 density=8.8e13 degen=2 sigp=2.6e-013 sign=2.6e-015/
region=2
trap donor e.level=0.71 density=5.0e13 degen=2 sigp=8.3e-013 sign=8.3e-015/
region=2
trap donor e.level=0.90 density=6.5e13 degen=2 sigp=3e-011 sign=3e-013 region=2
```

```
#Middle Cell
trap acceptor e.level=0.13 density=8.4e14 degen=2 sign=2.6e-015 sigp=2.6e-017/
region=4
trap acceptor e.level=0.29 density=1.6e15 degen=2 sign=2.6e-013 sigp=2.6e-015/
region=4
trap acceptor e.level=0.35 density=1.0e15 degen=2 sign=6.4e-015 sigp=6.4e-017/
region=4
trap acceptor e.level=0.71 density=2.7e14 degen=2 sign=4e-013 sigp=4e-015/
region=4
trap donor e.level=0.41 density=8.8e13 degen=2 sigp=2.6e-013 sign=2.6e-015/
region=5
trap donor e.level=0.71 density=5.0e13 degen=2 sigp=8.3e-013 sign=8.3e-015/
region=5
trap donor e.level=0.90 density=6.5e13 degen=2 sigp=3e-011 sign=3e-013 region=5

#Bottom Cell
trap acceptor e.level=0.13 density=8.4e14 degen=2 sign=2.6e-015 sigp=2.6e-017/
region=8
trap acceptor e.level=0.29 density=1.6e15 degen=2 sign=2.6e-013 sigp=2.6e-015/
region=8
trap acceptor e.level=0.35 density=1.0e15 degen=2 sign=6.4e-015 sigp=6.4e-017/
region=8
trap acceptor e.level=0.71 density=2.7e14 degen=2 sign=4e-013 sigp=4e-015/
region=8
trap donor e.level=0.41 density=8.8e13 degen=2 sigp=2.6e-013 sign=2.6e-015/
region=9
trap donor e.level=0.71 density=5.0e13 degen=2 sigp=8.3e-013 sign=8.3e-015/
region=9
trap donor e.level=0.90 density=6.5e13 degen=2 sigp=3e-011 sign=3e-013 region=9
```

THIS PAGE INTENTIONALLY LEFT BLANK

APPENDIX B. MATLAB SCRIPT

A. LOADING DATA AND PLOTTING I-V CURVES

```
%% Prepare the Workspace
clc

%% Plain Cell
% Load in Silvaco Data

%Top of Cell
Tripletop_V=data1(:,12);
Tripletop_I=(data1(:,11));
%plot(Tripletop_V,Tripletop_I);

%Middle of Cell
Triplemiddle_V=data2(:,18);
Triplemiddle_I=(data2(:,17));
%plot(Triplemiddle_V,Triplemiddle_I);

%Bottom of Cell
Triplebottom_V=data3(:,24);
Triplebottom_I=(data3(:,23));
%plot(Triplebottom_V,Triplebottom_I);

%% Combine Data to Create Overall I-V Curve
% Add Voltages Together
Total_V1=Tripletop_V+Triplemiddle_V+Triplebottom_V;
I_Matrix=[Tripletop_I,Triplemiddle_I,Triplebottom_I];

%Use Lowest Current
Total_I1=min(I_Matrix,[],2);

%%Plot Overall I-V Curve
plot(Total_V1,Total_I1,'k')
grid on
set(gca,'fontsize',18,'fontweight','demi')
xlabel('Anode Voltage (V)')
ylabel('Cathode Current (A)')
title('Overall Triple Junction Cell I-V Curve')
legend('InGaP/GaAs/Ge Solar Cell I-V Curve')
hold all

%Calculate Important Characteristics
Voc=Total_V1(89)
Isc=Total_I1(1)
Pmax=max(Total_V1.*Total_I1)
FF=Pmax/(Voc*Isc)
eff=Pmax/.136
```

```
%%Cell Rad 1
% Prepare the Workspace
clc

%% Load in Silvaco Data
%Top of Cell
Tripletop_V10e14=data4(:,12);
Tripletop_I10e14=(data4(:,11));
%plot(Tripletop_V,Tripletop_I);

%Middle of Cell
Triplemiddle_V10e14=data5(:,18);
Triplemiddle_I10e14=(data5(:,17));
%plot(Triplemiddle_V,Triplemiddle_I);

%Bottom of Cell
Triplebottom_V10e14=data6(:,24);
Triplebottom_I10e14=(data6(:,23));
%plot(Triplebottom_V,Triplebottom_I);

%% Combine Data to Create Overall I-V Curve
% Add Voltages Together
Total_V110e14=Tripletop_V10e14+Triplemiddle_V10e14+Triplebottom_V10e14;

%Make Current Matrix
I_Matrix10e14=[Tripletop_I10e14,Triplemiddle_I10e14,Triplebottom_I10e14
];

%Use Lowest Current
Total_I10e14=min(I_Matrix10e14,[],2);

%Plot Overall I-V Curve
plot(Total_V110e14,Total_I10e14,'b')
grid on
xlabel('Anode Voltage (V)')
ylabel('Cathode Current (A)')
title('Triple Junction Cell I-V Curve')
legend('10e14 Fluence Applied InGaP/GaAs/Ge Solar Cell I-V Curve')
hold all

%Calculate Important Characteristics
Voc10e14=Total_V110e14(89)
Isc10e14=Total_I10e14(1)
Pmax10e14=max(Total_V110e14.*Total_I10e14)
FF10e14=Pmax10e14/(Voc10e14*Isc10e14)
eff10e14=Pmax10e14/.136

%%Cell Rad 2
% Prepare the Workspace
clc

%% Load in Silvaco Data
```

```
%Top of Cell
Tripletop_V10e15=data7(:,12);
Tripletop_I10e15=(data7(:,11));
%plot(Tripletop_V,Tripletop_I);

%Middle of Cell
Triplemiddle_V10e15=data8(:,18);
Triplemiddle_I10e15=(data8(:,17));
%plot(Triplemiddle_V,Triplemiddle_I);

%Bottom of Cell
Triplebottom_V10e15=data9(:,24);
Triplebottom_I10e15=(data9(:,23));
%plot(Triplebottom_V,Triplebottom_I);

%% Combine Data to Create Overall I-V Curve
% Add Voltages Together
Total_V110e15=Tripletop_V10e15+Triplemiddle_V10e15+Triplebottom_V10e15;

%Make Current Matrix
I_Matrix10e15=[Tripletop_I10e15,Triplemiddle_I10e15,Triplebottom_I10e15
];

%Use Lowest Current
Total_I10e15=min(I_Matrix10e15,[],2);

%%Plot Overall I-V Curve
plot(Total_V110e15,Total_I10e15,'m')
grid on
xlabel('Anode Voltage (V)')
ylabel('Cathode Current (A)')
title('Triple Junction Cell I-V Curve')
legend('10e15 Fluence Applied InGaP/GaAs/Ge Solar Cell I-V Curve')
hold all

%Calculate Important Characteristics
Voc10e15=Total_V110e15(89)
Isc10e15=Total_I10e15(1)
Pmax10e15=max(Total_V110e15.*Total_I10e15)
FF10e15=Pmax10e15/(Voc10e15*Isc10e15)
eff10e15=Pmax10e15/.136

%%Cell Rad 3
% Prepare the Workspace
clc

%% Load in Silvaco Data
%Top of Cell
Tripletop_V10e16=data10(:,12);
Tripletop_I10e16=(data10(:,11));
%plot(Tripletop_V,Tripletop_I);

%Middle of Cell
Triplemiddle_V10e16=data11(:,18);
```

```
Triplemiddle_I10e16=(data11(:,17));
%plot(Triplemiddle_V,Triplemiddle_I);

%Bottom of Cell
Triplebottom_V10e16=data12(:,24);
Triplebottom_I10e16=(data12(:,23));
%plot(Triplebottom_V,Triplebottom_I);

%% Combine Data to Create Overall I-V Curve
% Add Voltages Together
Total_V110e16=Tripletop_V10e16+Triplemiddle_V10e16+Triplebottom_V10e16;

%Make Current Matrix
I_Matrix10e16=[Tripletop_I10e16,Triplemiddle_I10e16,Triplebottom_I10e16
];

%Use Lowest Current
Total_I10e16=min(I_Matrix10e16,[],2);

%%Plot Overall I-V Curve
plot(Total_V110e16,Total_I10e16,'r')
grid on
xlabel('Anode Voltage (V)')
ylabel('Cathode Current (A)')
title('Triple Junction Cell I-V Curve')
legend('10e16 Fluence Applied InGaP/GaAs/Ge Solar Cell I-V Curve')
hold all

%Calculate Important Characteristics
Voc10e16=Total_V110e16(89)
Isc10e16=Total_I10e16(1)
Pmax10e16=max(Total_V110e16.*Total_I10e16)
FF10e16=Pmax10e16/(Voc10e16*Isc10e16)
eff10e16=Pmax10e16/.136
```

B. COMPARING ISC, VOC, AND PMAX OF THE EXPERIMENTAL AND SIMULATED TRIPLE JUNCTION SOLAR CELLS UNDER THREE FLUENCE LEVELS

```
%% Prepare the Workspace
clc

%Fluence Levels
Fluence=[1,10e14,10e15,10e16];

%Data from Experiment
EXPIsc=[1,1,.97,.89];
EXPVoc=[1,.95,.90,.84];
EXPPmax=[1,.96,.90,.65];
```

```
%Data from Simulation
SIMIsc=[1,1,.955,.904];
SIMVoc=[1,.88,.875,.87];
SIMPmax=[1,.994,.936,.83];

%%Plot the 3 Characteristics

%Isc
figure(1);
plot(Fluence,EXPIsc,'k','linewidth',2)
hold on
plot(Fluence,SIMIsc,'r','linewidth',2)
grid on
set(gca,'fontsize',18,'fontweight','demi')
xlabel('Fluence Level (e/cm^2)','fontsize',18);
ylabel('Percentage of the Pre-Irradiated Isc','fontsize',18)
legend('Experimental', 'Simulated')
title('Effects of Radiation on the Isc of the Experimental and
Simulated Triple Junction Solar Cell','fontsize',18)

%Voc
figure(2);
plot(Fluence,EXPVoc,'k','linewidth',2)
hold on
plot(Fluence,SIMVoc,'r','linewidth',2)
grid on
set(gca,'fontsize',18,'fontweight','demi')
xlabel('Fluence Level (e/cm^2)','fontsize',18);
ylabel('Percentage of the Pre-Irradiated Voc','fontsize',18)
legend('Experimental', 'Simulated')
title('Effects of Radiation on the Voc of the Experimental and
Simulated Triple Junction Solar Cell','fontsize',18)

%Pmax
figure(3);
plot(Fluence,EXPPmax,'k','linewidth',2)
hold on
plot(Fluence,SIMPmax,'r','linewidth',2)
grid on
set(gca,'fontsize',18,'fontweight','demi')
xlabel('Fluence Level (e/cm^2)','fontsize',18);
ylabel('Percentage of the Pre-Irradiated Pmax','fontsize',18)
legend('Experimental', 'Simulated')
title('Effects of Radiation on the Pmax of the Experimental and
Simulated Triple Junction Solar Cell','fontsize',18)
```

C. COMPARING ISC, VOC, AND PMAX OF THE EXPERIMENTAL AND SIMULATED GAAS SOLAR CELLS UNDER THREE FLUENCE LEVELS

```
%% Prepare the Workspace
clc

%Fluence Levels
Fluence=[1,10e14,10e15,10e16];

%Data from Experiment
GaAsEXPIsc=[1,.94,.81,.68];
GaAsEXPVoc=[1,.97,.90,.86];
GaAsEXPPmax=[1,.864,.692,.575];

%Data from Simulation

GaAsSIMIsc=[1,.909,.848,.819];
GaAsSIMVoc=[1,.983,.914,.879];
GaAsSIMPmax=[1,.876,.722,.659];

%%Plot the 3 Characteristics

%Isc
figure(1);
semilogx(Fluence,GaAsEXPIsc,'k','linewidth',2')
hold on
semilogx(Fluence,GaAsSIMIsc,'r','linewidth',2)
grid on
set(gca,'fontsize',18,'fontweight','demi')
xlabel('Fluence Level (e/cm^2)','fontsize',18);
ylabel('Percentage of the Pre-Irradiated Isc','fontsize',18)
legend('Experimental', 'Simulated')
title('Effects of Radiation on the Isc of the Experimental and
Simulated GaAs Solar Cell','fontsize',18)

%Voc
figure(2);
semilogx(Fluence,GaAsEXPVoc,'k','linewidth',2)
hold on
semilogx(Fluence,GaAsSIMVoc,'r','linewidth',2)
grid on
set(gca,'fontsize',18,'fontweight','demi')
xlabel('Fluence Level (e/cm^2)','fontsize',18);
ylabel('Percentage of the Pre-Irradiated Voc','fontsize',18)
legend('Experimental', 'Simulated')
title('Effects of Radiation on the Voc of the Experimental and
Simulated GaAs Solar Cell','fontsize',18)

%Pmax
figure(3);
semilogx(Fluence,GaAsEXPPmax,'k','linewidth',2)
hold on
```

```
semilogx(Fluence,GaAsSIMPmax,'r','linewidth',2)
grid on
set(gca,'fontsize',18,'fontweight','demi')
xlabel('Fluence Level (e/cm^2)','fontsize',18);
ylabel('Percentage of the Pre-Irradiated Pmax','fontsize',18)
legend('Experimental', 'Simulated')
title('Effects of Radiation on the Pmax of the Experimental and
Simulated GaAs Solar Cell','fontsize',18)
```

THIS PAGE INTENTIONALLY LEFT BLANK

LIST OF REFERENCES

[1] M. O'Brien, Space radiation environment. [Online] Available: http://radhome.gsfc.nasa.gov/radhome/environ.htm, Dec. 1, 1998 [Mar. 20, 2012].

[2] P. Michalopoulous, "A novel approach for the development and optimization of state-of-the-art photovoltaic devices using Silvaco," M.S. thesis, Naval Postgraduate School, Monterey, California, 2002.

[3] M. Tsutagawa. "Triple junction InGaP/GaAs/Ge solar cell optimization using Silvaco ATLAS", M.S. thesis, Naval Postgraduate School, Monterey, California, 2008.

[4] A. Crespin. "A novel approach to modeling the effects of radiation in gallium-arsenide solar cells using Silvaco's ATLAS software", M.S. thesis, Naval Postgraduate School, Monterey, California, 2004.

[5] M. Dayah. "Dynamic Periodic Table" [Online]. Available:PTable.com, Feb. 12, 2012 [Mar. 21, 2012].

[6] "Silicon Atom" [Online]. Available: http://www.learnabout-electronics.org/images/silicon_atom.jpg, [Mar. 21, 2012].

[7] A. Carpi. "Atomic Theory II" [Online]. Available: http://www.visionlearning.com/library/module_viewer.php?mid=51, 2003 [Mar. 21, 2012].

[8] B. Streetman, *Solid State Electronic Devices Fourth Edition*, Englewood Cliffs, NJ: Prentice Hall, pp. 33-35, 1995.

[9] Encyclopaedia Brittanica, "Electron Orbitals" [Online]. Available:http://www.britannica.com/EBchecked/media/92141/Atomic-orbitals-Electrons-fill-in-shell-and-subshell-levels-in, [Mar. 21, 2012]

[10] R. Baker. *CMOS: Circuit Design, Layout, and Simulation*, Hoboken, NJ: Wiley-IEEE Press, pp. 745-750, 2008.

[11] R. Jones. "Energy Gap" [Online]. Available: http://people.seas.harvard.edu/~jones/es154/lectures/lecture_2/energy_gap/band_gap_2.gif, Jan. 12, 2002 [March 21, 2012].

[12] D. Leadley. "Electronic Band Structure" [Online]. Available: http://www2.warwick.ac.uk/fac/sci/physics/postgraduate/current/regs/mpags/ex5/bandstructure/energy_band_gaps_in_materials.jpg Jul. 15 2010 [March 21, 2012].

[13] D. Neaman. *An Introduction to Semiconductor Devices*, New York, NY: McGraw Hill, pp. 3-25, 599-605, 2006.

[14] "Crystal Structures" [Online]. Available: http://spectrum. ieee.org /image/1838375, [Mar. 21, 2012].

[15] "Basic Crystal Structures" [Online]. Available: http://www.a-levelphysicstutor.com /images/matter/crystal-cells02.jpg, [Mar. 21, 2012].

[16] B. Zeghbroech. "Diamond Crystal Structure" [Online]. Available: http://ecee.colorado.edu/~bart/book/book/chapter2/ch2_2.htm#2_2_3, 2007 [Mar. 21, 2012].

[17] "Substitutional and Interstitial Impurities" [Online]. Available: http://chemed.chem.purdue.edu/genchem/topicreview/bp/materials/graphics/19.gif, [Mar. 21, 2012].

[18] "Fermi-Dirac Distribution Function" [Online]. Available: http://1.bp.blogspot.com/_Jt8jI5P6sEU/TKjjtSo92NI/AAAAAAAAEVo/ZczqxI1tYQU/s400/Fermi-Dirac+Distribution+Function.bmp, [Mar. 21, 2012].

[19] "Diffusion of Current" [Online]. Available: http://1.bp.blogspot.com/_7UH1P0Umjhk/SWwu6w0_8dI/AAAAAAAABkw/fc2RpdjorXE/s320/Diffusion+of+Current.jpg, [Mar. 21, 2012].

[20] B. Zeghbroeck. “Carrier Transport” [Online]. Available: http://ecee.colorado.edu/~bart/book/transpor.htm, 1998 [Mar.21, 2012].

[21] B. Zeghbroeck. “Semiconductors Fundamentals” [Online]. Available: http://ecee.colorado.edu/~bart/book/book/chapter2/ch2_8.htm#2_8_5, 2011 [Mar. 21, 2012].

[22] “Czochralski Growth” [Online]. Available: http://www.eere.energy.gov/basics/renewable_energy/images/illust_czoch.gif,[Mar. 21, 2012].

[23] “MBE Structure” [Online]. Available: http://www.veeco.com/images/markets/subpages/mbe_structure.jpg, [Mar. 21, 2012].

[24] “Diffusion” [Online]. Available: http://saroshshahbuddin.files.wordpress.com/2010/08/diffusion.png,[Mar. 21, 2012].

[25] B. Zeghbroech. “P-N Junctions” [Online]. Available: http://ecee.colorado.edu/~bart/book/book/chapter4/ch4_2.htm, 2011 [Mar. 21, 2012].

[26] “Reverse-Biased P-N Junction” [Online]. Available: http://hyperphysics.phy-astr.gsu.edu/hbase/solids/imgsol/diod4.gif, [Mar. 22, 2012]

[27] “Reverse-Biased Band Diagram” [Online]. Available: http://img11.imageshack.us/img11/139/pnjunctionreversebias.jpg, [Mar. 22, 2012].

[28] “Forward-Biased P-N Junction” [Online]. Available: hyperphysics.phy-astr.gsu.edu, [Mar. 22, 2012].

[29] E. Schubert. “Light Emitting Diodes” [Online] Available: http://www.ecse.rpi.edu/~schubert/Light-Emitting-Diodes-dot-org/chap04/F04-01%20PN%20junction%20energies.jpg, Oct. 5, 2004 [Mar. 22, 2012].

[30] “Diode I-V Characteristics” [Online]. Available: http://www.eng.uwi.tt/depts/elec/staff/rdefour/ee33d/images/fig2_2.gif, [Mar. 22, 2012].

[31] "Tunneling" [Online]. Available: http://ecourses.vtu.ac.in/nptel/ courses/Webcourse-contents/IIT-Delhi/Semiconductor%20Devices/pn/PN_3_img/fig%208.gif, [Mar. 22, 2012].

[32] "Avalanche Effect" [Online]. Available: http://www.globalsino. com /micro/1/images/1micro9820d.gif, [Mar 22. 2012].

[33] " The Photovoltaic Process" [Online]. Available:http://www.thep-center.org/uploadfile/Thin%20Film%20Eng/2.png,[Mar. 23, 2012].

[34] "I-V Curve for a PV Cell" [Online]. Available: http://www.solarjourneyusa.com/Pictures/IV-curveMPPT.png, [Mar. 23, 2012].

[35] "AM0 Spectrum" [Online]. Available: http://origin-ars.sciencedirect.com/content/image/1-s2.0-S0927024804003952-gr2.gif, [Mar. 23, 2012].

[36] S. Michael, Class Lecture, Topic: "The Design and Optimization of Advanced Multi-Junction Solar Cells." Naval Postgraduate School, November 10, 2011.

[37] "Triple Junction Cell" [Online]. Available: http://jolisfukyu.tokai-sc.jaea.go.jp/fukyu/mirai-en/2009/img/honbun/4-8.jpg, [Mar. 23, 2012].

[38] T. Weatherford, Class Lecture, Topic: "Radiation Effects in Microelectronics." Naval Postgraduate School, March 5, 2012.

[39] "Earth Orbits" [Online]. Available: http://satelit.web.id/images/Orbits.gif, [Mar 24, 2012].

[40] National Aeronautics and Space Administration, *Solar Cell Radiation Handbook*, Jet Propulsion Laboratory, Pasadena, CA, 1982, updated 2008.

[41] "Basic Radiation Physics." [Online]. Available: http://www.e-radiography.net/radsafety/rad_physics4.jpg,[Mar. 23, 2012].

[42] *ATLAS User's Manual*, vols. 1-2, software version 5.6.0.R, Silvaco International, Santa Clara, CA, 2012.

[43] B. Garcia, "Indium gallium nitride multijunction solar cell simulation using Silvaco ATLAS." M.S. thesis, Naval Postgraduate School, Monterey, California, 2007.

[44] M. Imaizumi, T. Takamoto, T. Ohshima, M. Yamaguchi, H. Itoh, S. Matsuda, "Radiaton effects on high-efficiency InGaP/GaAs/Ge triple-junction solar cells developed for terrestrial use," *Photovoltaic Specialists Conference, 2002. Conference Record of the Twenty-Ninth IEEE* , vol., no., pp. 990-993, 19-24 May 2002.

[45] National Aeronautics and Space Administration, *Solar Cell Radiation Handbook*, Jet Propulsion Laboratory, Pasadena, CA, pp. 148-150, 1989.

THIS PAGE INTENTIONALLY LEFT BLANK

INITIAL DISTRIBUTION LIST

1. Defense Technical Information Center
   Ft. Belvoir, Virginia

2. Dudley Knox Library
   Naval Postgraduate School
   Monterey, California

3. Dr. Clark Robertson, Chairman
   Department of Electrical and Computer Engineering
   Naval Postgraduate School
   Monterey, California

4. Dr. Sherif Michael
   Department of Electrical and Computer Engineering
   Naval Postgraduate School
   Monterey, California

5. Dr. Douglas Fouts
   Department of Electrical and Computer Engineering
   Naval Postgraduate School
   Monterey, California

6. ENS Daniel Schiavo
   North Plainfield, New Jersey

7. Mr. and Mrs. Daniel Schiavo
   North Plainfield, New Jersey

8. Ms. Caitlin Liff
   Davidsonville, Maryland